TUS 7-19

DOE/ER-0046/9

Damage Analysis and Fundamental Studies

Quarterly Progress Report
Jan-Mar 1982

May 1982

U.S. Department of Energy
Assistant Secretary for Energy Technology
Office of Fusion Energy
Washington, DC 20545

NOTICE

This report was prepared as an account of work sponsored by the United States Government. Neither the United States nor the U.S. Department of Energy (DOE), nor any of its employes, nor any of its contractors, subcontractors or their employes, makes any warranty, expressed or implied, or assumes any legal liability or responsibility for any third party's use or the results of such use of any information, apparatus, product or process disclosed in this report, or represents that its use by such third party would not infringe privately owned rights.

Printed in the United States of America
Available from
National Technical Information Service
U.S. Department of Commerce
5285 Port Royal Road
Springfield, VA 22161

NTIS price codes
Printed copy: A10
Microfiche copy: A01

DOE-Richland, WA

DOE/ER-0046/9
UC-20,20c

Damage Analysis and Fundamental Studies

Quarterly Progress Report
Jan-Mar 1982

May 1982

U.S. Department of Energy
Assistant Secretary for Energy Technology
Office of Fusion Energy
Washington, DC 20545

FOREWORD

This report is the seventeenth in a series of Quarterly Technical Progress Reports on Damage Analysis and Fundamental Studies (DAFS), which is one element of the Fusion Reactor Materials Program, conducted in support of the Magnetic Fusion Energy Program of the U. S. Department of Energy (DOE). The first eight reports in this series were numbered DOE/ET-0065/1 through 8. Other elements of the Materials Program are:

- Alloy Development for Irradiation Performance (ADIP)
- Plasma-Materials Interaction (PMI)
- Special Purpose Materials (SPM).

The OAFS program element is a national effort composed of contributions from a number of National Laboratories and other government laboratories, universities, and industrial laboratories. It was organized by the Materials and Radiation Effects Branch, Office of Fusion Energy, DOE, and a Task Group on Damage Analysis and Fundamental Studies, which operates under the auspices of that Branch. The purpose of this series of reports is to provide a working technical record of that effort for the use of the program participants, the fusion energy program in general, and the DOE.

This report is organized along topical lines in parallel to a Program Plan of the same title so that activities and accomplishments may be followed readily, relative to that Program Plan. Thus, the work of a given laboratory may appear throughout the report. The Table of Contents is annotated for the convenience of the reader.

This report has been compiled and edited under the guidance of the Chairman of the Task Group on Damage Analysis and Fundamental Studies, D. G. Doran, Hanford Engineering Development Laboratory (HEDL). His efforts, those of the supporting staff of HEDL, and the many persons who made technical contributions are gratefully acknowledged. M. M. Cohen, Materials and Radiation Effects Branch, is the DOE counterpart to the Task Group Chairman and has responsibility for the DAFS Program within DOE.

D. L. Vieth, Chief
Materials and Radiation Effects Branch
Office of Fusion Energy

CONTENTS

CONTENTS (Cont'd)

CONTENTS (Cont'd)

FIGURES

Page

CHAPTER 2

FIGURES (Cont'd)

FIGURES (Cont'd)

FIGURES (Cont'd)

FIGURES (Cont'd)

TABLES

TABLES (Cont'd)

TABLES (Cont'd)

Page

CHAPTER 4

CHAPTER 1

IRRADIATION TEST FACILITIES

RTNS-II IRRADIATIONS AND OPERATIONS

C. M. Logan and D. W. Heikkinen (Lawrence Livermore National Laboratory)

1.0 Objective

The objectives of this work are operation of OFE's RTNS-II (a 14-MeV neutron source facility), machine development, and support of the experimental program that utilizes this facility. Experimenter services include dosimetry handling, scheduling, coordination, and reporting. RTNS-II is dedicated to materials research for the fusion power program. Its primary use is to aid in the development of models of high-energy neutron effects. Such models are needed in interpreting and projecting to the fusion environment engineering data obtained in other neutron spectra.

2.0 Summary

During this quarter, a letter of understanding between the U.S. (DOE) and Japan (Monbusho) was signed. This implements joint utilization and support of the RTNS-II facility. Irradiations were done on a total of fourteen different experiments. Approximately five weeks of unscheduled outage occurred due to problems with the 50-cm target seal.

3.0 Program

Title: RTNS-II Operations (WZJ-16)
Principal Investigator: C. M. Logan
Affiliation: Lawrence Livermore National Laboratory

4.0 Relevant DAFS Program Plan Task/Subtask

TASK II.A.2,3,4.
TASK II.B.3,4
TASK II.C.1,2,6,11,18.

5.1 Irradiations-C.M. Logan, D.W. Heikkinen and M.W. Guinan (LLNL)

During this quarter, irradiations were done for the following people:

Principal Contact	Sample
T. Iida (Osaka)	Fiber Optic Cables, Insulators, Diffraction Grating, Transistors, Amorphous Metals
J. Fowler (LANL)	Macor, Saphire
H. Vonach (Vienna)	Nb
C. Snead (BNL)	Superconductor
R. Borg (LLNL)	Geological Materials
M. Singh (LLNL)	Laser Glass
R. Van Konynenburg (LLNL)	MFTF Magnet Insulaters
R. Jalbert	Tritium Detector Development
R. Hartmann (Northrop)	IC Chips
D. Kaletta (Karlsruhe)	Nb, V, Ni
H. Matsui (Nagoya)	TiC, Li_2O
B. Schumacher (LLNL)	Nb dosimetry, Thin Proton Recoil Counter
D. Heikkinen (LLNL)	Nb dosimetry
G. Woolhouse (Aracor)	Silicon

5.2 RTNS-II Status-C. M. Logan and D. W. Heikkinen

During the first five weeks of this quarter, the 50-cm target seal continued to cause problems. These problems were caused by use of a stainless steel stator. The stainless steel stator has been replaced by a brass stator similar to the one used with the 23-cm targets. This appears to have solved the problem.

Irradiations have begun for Japanese scientists as part of the joint utilization plan for RTNS-II. A steering committee has been established to oversee the experimntal program at RTNS-II. In addition, points of

contact have been appointed for both the Japanese and United States sides. These are shown in Table 1.

TABLE 1

STEERING COMMITTEE AND POINTS OF CONTACT

	U.S.	Japan
Point of Contact	D. Doran	K. Sumita
	HEDL	Osaka
Steering Committee	R. Borchers	I. Kawano
	LLNL	Monbusho
	M. Cohen	K. Kawamura
	DOE	Tokyo Institute of Techno1ogy

6.0 Future Work

The first meeting of the Steering Committee will be held in Tokyo during April 1982. Irradiations will be continued or are scheduled for T. Iida (Osaka), H. Matsui (Nagoya), M. Guinan (LLNL), J. Fowler (LANL), D. Kaletta (Karlsruhe), R. Hartmann (Northrop), and C. Snead (BNL).

7.0 Publications

None

CHAPTER 2

DOSIMETRY AND DAMAGE PARAMETERS

ROOM-RETURN NEUTRON FLUX MEASUREMENTS AT RTNS-II

L. R. Greenwood (Argonne National Laboratory)

1.0 Objective

To characterize the neutron flux and energy spectrum in the RTNS-II target room.

2.0 Summary

Neutron activation measurements have been used to determine the neutron flux and energy spectrum in the RTNS-II target room both near the target and at distances of 5, 15, 30, 120, and 380 cm (the backwall). The room-return neutron flux and spectrum appears to be constant throughout the room, but increasing from 1% of the total flux at 18 cm to 3% at 30 cm and 31% at 120 cm.

3.0 Program

Title: Dosimetry and Damage Analysis

Principal Investigator: L. R. Greenwood

Affiliation: Argonne National Laboratory

4.0 Relevant DAFS Program Plan Task/Subtasks

Task II.A.2 High-Energy Neutron Dosimetry

Task II.A.2.2 Flux-Spectral Definition in RTNS-II

5.0 Accomplishments and Status

A joint experiment[1,2] was conducted with Rockwell International and Lawrence Livermore Laboratory (LLL) to characterize the neutron flux and energy spectrum at the Rotating Target Neutron Source (RTNS-II). Various dosimetry samples were irradiated on arcs at distances of 5, 15, 30, 120, and 380 cm from the source, the last position corresponding to the back door of the target room. At distances of 30 cm or greater the neutron activation data clearly shows the influence of room-return neutrons. Clint Logan[3] performed neutronics calculations to estimate this room-return effect. Our measurements, including radiometric measurements at Argonne and LLL, was then used to adjust the calculated flux-spectra.

The radiometric foil measurements are summarized in Table 1. Only the 0° values are shown at distances of 30 cm or greater. A large number of measurements were also made at other angles and at closer distances. The presence of room-return neutrons is easily evident in the activation rates listed in Table 1. Note that whereas the high threshold $(n, 2n)$ reactions decrease roughly as the distance squared, the lower threshold (n, p) and (n, α) reactions show a much smaller decrease while the thermal (n, γ) reactions are nearly constant.

The data in Table 1 was used with the STAYSL code to adjust the spectrum calculated by Logan. The results are illustrated in Figures l and 2. Figure l shows the final neutron energy spectrum determined at 120 cm from the target at 0" to the beam. The spectra at 30 cm and 380 cm are nearly identical

TABLE 1

ACTIVATION RATES FOR RTNS-II

Values are time-averaged over a 252-hour period. Distances from the source are at 0° to the beam.

Reaction	$\sigma\phi$ (x 10^{-12} atom/atom-S)		
	30 cm	120 cm	380 cm
$^{45}Sc(n,\gamma)^{46}Sc$	59.9	53.8	55.5
$^{59}Co(n,\gamma)^{60}Co$	96.9	81.3	83.1
$^{107}Ag(n,\gamma)^{110m}Ag$	--	12.0	12.0
$^{197}Au(n,\gamma)^{198}Au$	385.	276.	270.
$^{48}Ti(n,p)^{48}Sc$	25.5	--	--
$^{54}Fe(n,p)^{54}Mn$	116.	7.40	1.00
$^{59}Co(n,p)^{59}Fe$	18.0	1.17	0.129
$^{58}Ni(n,p)^{58}Co$	116.	7.93	1.16
$^{60}N(n,p)^{60}Co$	51.5	3.23	0.320
$^{27}Al(n,\alpha)^{24}Na$	41.4	--	--
$^{54}Fe(n,\alpha)^{51}Cr$	34.8	2.16	0.217
$^{45}Sc(n,2n)^{44m}Sc$	48.9	3.01	0.281
$^{59}Co(n,2n)^{58}Co$	313.	19.2	1.82
$^{58}Ni(n,2n)^{57}Ni$	15.1	0.945	0.087
$^{89}Y(n,2n)^{88}Y$	379.	23.8	2.21
$^{93}Nb(n,2n)^{92m}Nb$	178.	10.7	1.06
$^{107}Ag(n,2n)^{106}Ag$	--	13.1	1.31
$^{169}Tm(n,2n)^{168}Tm$	743.	46.3	4.75
$^{197}Au(n,2n)^{196}Au$	851.	53.1	5.17

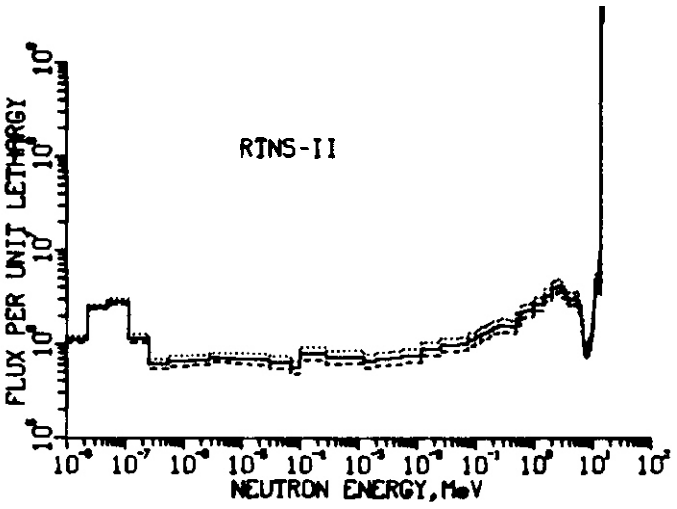

Pig. 1. Measured Neutron Spectrum at the RTNS-II d–t Neutron Source at LLL at a Distance of 30 cm on the 0° Beam Axis. The 14.9-MeV Spike is from the Source and All Lower Energy Neutrons are Due to Scattering from the Walls. The Room-Return Energy Spectrum is Constant Throughout the Target *Room.*

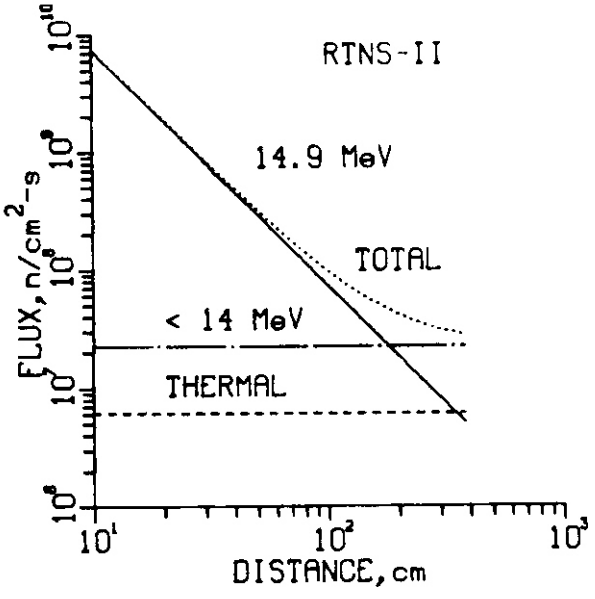

Pig. 2. Neutron Flux Maps for the RTNS-II d–t Source at LLL. The 14.9-MeV Spike Decreases as the Distance Squared Whereas the Room Return Flux is Isotropic. The Roan Return Flux is Insignificant (<1%) at Distances Less Than 18 cm.

except for the peak at 14.9 MeV. We thus conclude that the room-return flux and spectrum is constant and isotropic throughout the target room. The adjusted spectra agree quite well with the calculations by Logan.

Figure 2 illustrates the flux distribution in the RTNS-II target room. The absolute values are for the small targets. The 14.9-MeV peak (0°) decreases as the distance squared. All lower energy fluxes appear to be constant. This can be expressed mathematically as follows:

$$@(\text{Total}) = \Phi_o \left(\frac{1}{R_2} + c\right) \tag{1}$$

where Φ_o is the 14.9-MeV source strength, R is the distance in centimeters, and C is the constant ratio of the room return flux to the source strength. We find that $C = 3.06 \times 10^{-5}$ cm^{-2}. The ratio of the room return flux to the total flux and 14.9 MeV flux is then given by:

$$\frac{\Phi(\text{Return})}{\Phi(\text{Total})} = \frac{R^2C}{1 + R^2C} \tag{2}$$

$$\frac{\Phi(\text{Return})}{\Phi(14.9\ \text{MeV})} = R^2C \tag{3}$$

Table 2 lists some values calculated using equations (2) and (3). Obviously, caution must be used at distances close to the target (< 5 cm) since finite size effects become important. Also, it should be noted that experimental assemblies will peturb the flux-spectrum due to scattering and attenuation of the neutrons. The equations also do not hold exactly for angles other than 0° to the beam since the source is not quite isotropic. However, the neutron energy and source strength can easily be adjusted for other angles.[4] At

back angels (> 90°) effects must also be included for the rotating target itself.

Table 2

ROOM-RETURN NEUTRON FLUX AT RTNS-II

R, cm	Return/Total	Return/14.9 MeV
5	7.7×10^{-4}	7.7×10^{-4}
10	3.1×10^{-3}	3.1×10^{-3}
15	6.8×10^{-3}	6.9×10^{-3}
30	0.027	0.028
60	0.099	0.110
120	0.31	0.44
200	0.55	1.22
380 (wall)	0.82	4.42

The room-return fluxes (Table 2) and energy spectrum (Figure 1) are especially interesting since they are quite similar to the first wall of a fusion reactor. The total steady state flux at 100 cm is about 10^8 n/cm^2-s producing a fluence of 10^{13} n/cm^2 in about 24 hours. With larger targets and extended schedules at RTNS-II it may be possible to achieve a fluence of 10^{14} n/cm^2 per week at 100 cm from the source where the return flux is about one-fourth of the total. This fluence is comparable to that proposed for some experiments at near-tern fusion reactors (TFTR and JET). By placing moderators near the source or experiment, the return neutron flux could easily be increased and tailored for fusion materials studies.

6.0 References

1. L. R. Greenwood, D. Kneff, and M. Guinan, "Flux-Spectral Definition in RTNS-11", Chapter 2, DOE/ER-0046/3, p. 20–23 (1980).

2. B. M. Oliver, D. W. Kneff, M. M. Nakata, and H. Farrar IV, "Helium Generation Cross Sections for 14.8-MeV Neutrons", Chapter 2, DOE/ER-0046/7, p. 28–33 (1981).

3. C. Logan, Lawrence Livermore Laboratory, private communication (1981).

4. H. Liskien and A. Paulsen, Neutron Production Cross Sections and Energies for the Reactions $T(p,n)^3He$, $D(d,n)^3He$, and $T(d,n)^4He$, Nucl. Data Tables, A11, 569 (1973).

7.0 Future Work

Work is continuing to calculate neutron energy spectra at RTNS-II and to determine the best values for measured activation cross sections. A similar joint experiment with RIES and LLL is now being planned for the larger targets now being used at RTNS-II.

8.0 Publications

1. L. R. Greenwood, Neutron Flux and Spectral Measurements to Characterize Irradiation Facilities for Fusion Materials Studies, Proceedings of the Fourth ASTM-EURATOM Symposium on Reactor Dosimetry, March 22–26, 1982, National Bureau of Standards, Gaithersburg, MD.

RTNS-II FLUENCE MAPPING AND HELIUM GENERATION CROSS SECTIONS

O. W. Kneff, B. M. Oliver, M. M. Nakata, and H. Farrar IV (Rockwell International, Energy Systems Group)

1.0 Objective

The objectives of this work are to measure helium generation rates of materials for Magnetic Fusion Reactor applications in the ~14.8-MeV T(d,n) neutron environment, to characterize the T(d,n) neutron field of the Rotating Target Neutron Source-I1 (RTNS-II), and to develop helium accumulation neutron dosimeters for this test environment.

2.0 Summary

Neutron fluence contours have been calculated for the high-flux region of the RTNS-II sample irradiation volume, and the cross section of elemental lead has been determined for 14.8-MeV neutrons.

3.0 Program

Title: Helium Generation in Fusion Reactor Materials
Principal Investigators: D. W. Kneff and H. Farrar IV
Affiliation: Rockwell International, Energy Systems Group

4.0 Relevant OAFS Program Plan Task/Subtask

Subtask II.A.2.2 Flux-Spectral Definition in RTNS-II
Subtask II.A.4.2 T(d,n) Helium Gas Production Data

5.0 Accomplishments and Status

5.1 RTNS-II Neutron Fluence Map

Neutron fluence contours have been calculated for the high-flux sample irradiation region of the RTNS-II neutron field. They were obtained from the fluence map generated as part of a joint Rockwell International-Argonne National Laboratory (ANL)-Lawrence Livermore National Laboratory (LLNL) RTNS-II source characterization experiment. The experimental irradiation geometry was described in detail in a previous report,[**]) and the fluence mapping results (not previously reported) have been used in the determination of the helium generation cross sections for several pure elements and separated isotopes incorporated in the irradiation.[2] The fluence map and the generated contours are presented below.

The fluence map was derived from the radiometric and helium accumulation dosimetry materials irradiated in a miniature (20-mm-diameter by 8-mm-thick) capsule, mounted 0.76 mm from the front face of the rotating target assembly.[1] The activation foils and pure element wire dosimeters were segmented after the irradiation and analyzed, respectively, for activity levels (at ANL and LLNL) and generated helium. The fluence mapping was performed by first constructing an average map from the radiometric dosimetry data, assuming a circular deuteron beam shape. The magnitude of a slight capsule offset from the deuteron beam axis was first determined using a series of least-squares fits across the segmented foil data. This offset (1.1 mm) was then incorporated in a multiple regression analysis to evaluate the constants in an empirical model of the fluence profile.

This empirical model was then compared with the helium concentration gradients measured in the more finely segmented pure element dosimetry wires. In previous RTNS-I characterization experiments, the helium data revealed significant asymmetries in the neutron fluence profiles.[3,4] In the present case, the helium measurements demonstrated that the fluence profile for the RTNS-II

irradiation was generally symmetric, which is attributed in part to the larger neutron source spot (larger deuteron beam diameter) in close proximity to the capsule. No adjustments were made to the radiometric fluence map for this irradiation.

The empirical fluence model derived for this irradiation (9.3×10^5 nC, 122.6 h beam time) is given by the following expression:

$$\Phi(R,\Delta Z) = \left(\frac{A}{A + \Delta Z}\right)^{1.5}\left[C_0 + C_2\left(\frac{B}{B + \Delta Z}\right)^2 R^2 + C_3\left(\frac{B}{B + \Delta Z}\right)^3 R^3\right].$$

Here R is the radial distance from the neutron source axis (in mm), AZ is the axial distance from the front face of the irradiation capsule (mm), and Φ is the total fluence (in units of 10^{17} n/cm^2) at any given position (R,ΔZ) within the capsule. The evaluated constants for this expression are:

C_0 = 10.523
C_2 = -0.105
C_3 = 0.003
A = 3.816
B = 12

The capsule distance AZ is related to the axial distance from the outside face of the rotating target assembly (Z) by

$$Z(mm) = \Delta Z(mm) + 0.76 \text{ mm}.$$

Note that this map has not been adjusted for neutron attenuation by the capsule and its contents, and is thus not a "free space" map. The average neutron transmission through the entire capsule is roughly estimated to be about 88%.

The relative uncertainties in the fluence map (due, for example, to small asymnetries in the fluence profile) are ±5%, representing the region for which $0 \leq Z \leq 8.4$ mm and $0 \leq R \leq 8$ mm. These limits correspond to the volume of the capsule containing the analyzed dosimetry materials. Some additional dosimetry materials were located at R -9 mm, but have not yet been correlated with the map. The absolute fluence map uncertainty is ±7%, which includes the above relative uncertainties, activation counting uncertainties, and a ±4% uncertainty in the $^{93}Nb(n,2n)^{92m}Nb$ cross section used to normalize the map.(5)

Fluence contours (lines of constant fluence) derived from this empirical map are shown in Figure 1. This figure also indicates the geometry of the capsule relative to the beam axis. The large (> factor of 5) fluence gradients present over the small capsule thickness demonstrate the importance of passive dosimetry in this type of fast neutron irradiation experiment.

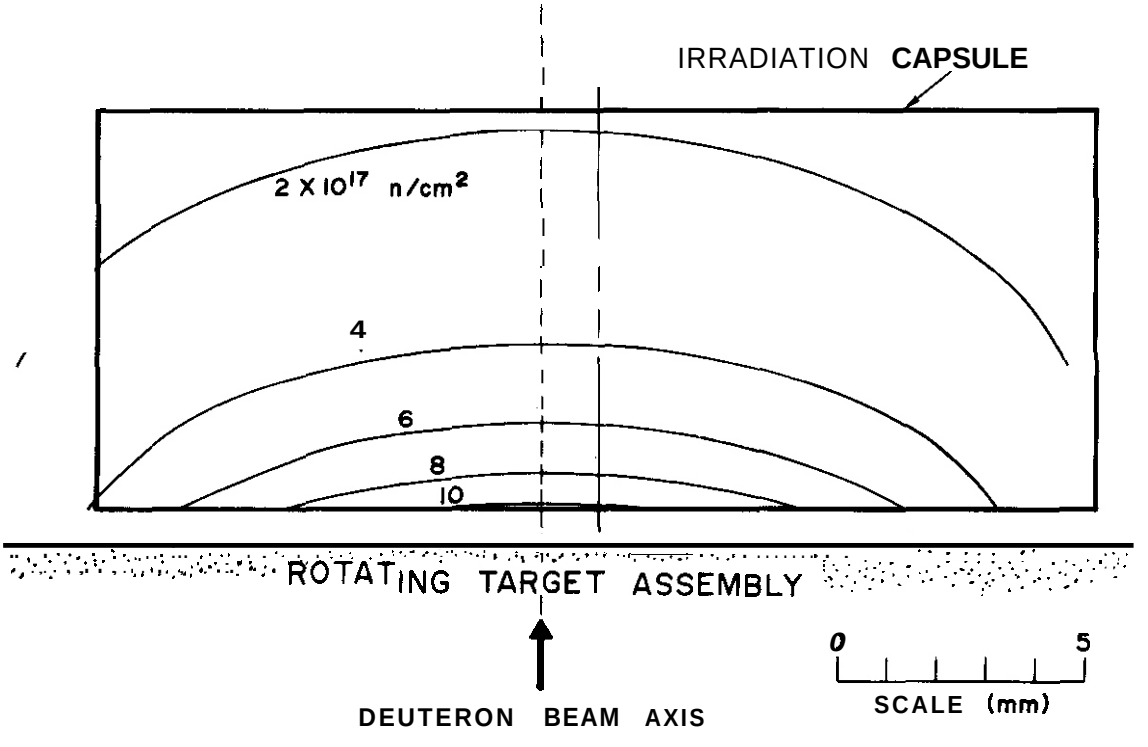

FIGURE 1. Contours of Constant Fluence for the High-Flux Region of the RTNS-II Neutron Field.

5.2 Helium Generation Cross Section for Lead

Total helium generation cross section measurements have been completed for pure element lead, irradiated in the ~14.8-MeV T(d,n) neutron spectrum of RTNS-II. These measurements were part of a program supported by the Office of Basic Energy Sciences of .the U.S. Department of Energy, to determine helium generation cross sections of a wide variety of elements and isotopes of interest to the fusion community. The cross section of lead was determined by combining the helium measurement for each of six samples with the neutron fluence at each sample's irradiation position (see Section 5.1), and averaging the six values. The final cross section value is 0.62 ± 0.05 mb.

Lead is of interest in fusion reactor designs as a component of candidate blanket materials. Its low helium generation cross section also makes lead compounds (including PbO, PbF_2, PbS) ideal for irradiating and measuring helium generation in the hard-to-handle elements oxygen, fluorine, and sulfur. Helium analysis of these materials, which were also irradiated at RTNS-II, is now in progress.

6.0 References

1. D. W. Kneff, B. M. Oliver. M. M. Nakata, and H. Farrar IV, "Characterization of the RTNS-II Neutron Field," in Damage Analysis and Fundamental Studies, Quarterly Progress Report July-September 1980, DOE/ER-0046/3, U.S. Department of Energy, 25 (1980).

2. D. W. Kneff, B. M. Oliver, M. M. Nakata, and H. Farrar IV, "Experimental Helium Generation Cross Sections for Fast Neutrons," Second Topical Meeting on Fusion Reactor Materials, Seattle, Washington, August 1981, J. Nucl. Mater. (to be published).

3. D. W. Kneff, H. Farrar IV, F. M. Mann, and R. E. Schenter, "Experimental and Theoretical Determination of Helium Production in Copper and Aluminum by 14.8-MeV Neutrons," Nucl. Technol., 49, 498 (1980).

4. D. W. Kneff, B. M. Oliver, M. M. Nakata, and H. Farrar IV, "Helium Generation Cross Sections for Fast Neutrons," in Proc. Symp. on Neutron Cross-sections from 10 to 50 MeV, M. R. Bhat and S. Pearlstein (Eds.), BNL-NCS-51245, Brookhaven National Laboratory, N.Y. (1980), p. 289.

5. O. R. Nethaway, "The $^{93}Nb(n,2n)^{92m}Nb$ Cross Section," J. Inorg. Nucl. Chem., 40, 1285 (1978).

7.0 Future Work

The helium analyses of RTNS-irradiated materials will continue. RTNS-II analyses are near completion for Li, ^{6}Li, ^{7}Li, C, O, F, and the candidate fusion alloys 316 stainless steel, HT9, and 9Cr1Mo.

8.0 Publications

None.

HELIUM ACCUMULATION NEUTRON DOSIMETRY FOR THE OMEGA WEST REACTOR

D. W. Kneff, B. M. Oliver, H. Farrar IV (Rockwell International, Energy Systems Group), and L. R. Greenwood (Argonne National Laboratory)

1.0 Objective

The objective of this work is to apply helium accumulation plus radiometric neutron dosimetry to the measurement of neutron fluences and energy spectra in mixed-spectrum fission reactors utilized for fusion materials testing.

2.0 Summary

Neutron energy spectrum unfolding using combined helium accumulation and radiometric measurements has been demonstrated for the neutron environment of the Omega West Reactor.

3.0 Program

Title: Helium Generation in Fusion Reactor Materials/Dosimetry and Damage Analysis

Principal Investigators: D. W. Kneff, H. Farrar IV, and L. R. Greenwood

Affiliation: Rockwell International and Argonne National Laboratory

4.0 Relevant DAFS Program Plan Task/Subtask

Subtask II.A.1.1 Flux-Spectral Definition in a Tailored Fission Reactor

5.0 Accomplishments and Status

Helium accumulation and radiometric neutron dosimetry measurements made for the Omega West Reactor (OWR) at Los Alamos have been used to demonstrate combined spectral unfolding in a mixed-spectrum reactor neutron environment. The measurements were made as part of the OWR spectral characterization

experiment performed in October 1980. The irradiation and the radiometric dosimetry results have been described in a previous report.(1)

The helium accumulation dosimetry was provided primarily by Al-0.7% ^{6}Li and Al-0.5% B alloy wires plus pure element copper wire. Samples of all three materials were irradiated within gadolinium cover foils, and additional samples of the alloy wires plus aluminum were irradiated without covers. Self-shielding effects were calculated to be -0.2% for the covered materials and ~1-2% for the uncovered materials. A total of 20 helium analyses were performed for these materials. The helium concentrations produced by the 7.6-hour, 8.0-MW irradiation are summarized in Table 1.

TABLE 1

SUMMARY OF HELIUM GENERATION RESULTS FROM THE OMEGA WEST REACTOR SPECTRAL CHARACTERIZATION IRRADIATION

Material	Cover	Average ^{4}He Atom Fraction	With Respect to
Al-0.7% ^{6}Li	Al	1.32×10^{-3}	^{6}Li
	Gd	1.34×10^{-4}	^{6}Li
Al-0.5% B	Al	5.42×10^{-3}	^{10}B
	Gd	5.62×10^{-4}	^{10}B
Al	Al	7.72×10^{-10}	Al
Cu	Gd	3.66×10^{-10}	Cu

Spectral unfolding calculations were performed using the unfolding code STAY'SL.(2) These calculations were performed both with and without the helium accumulation data. The spectral unfolding results obtained with the inclusion of ^{6}Li, ^{10}B, and Cu helium production reaction rates are shown in Figure 1, and the reactions used in the unfolding are summarized in Table 2. ENDF/B-V (n,α) cross sections(3) were used for the helium generation reactions The unfolding results indicate that the $^{6}Li(n,\alpha)$ and $Cu(n,\alpha)$ cross sections

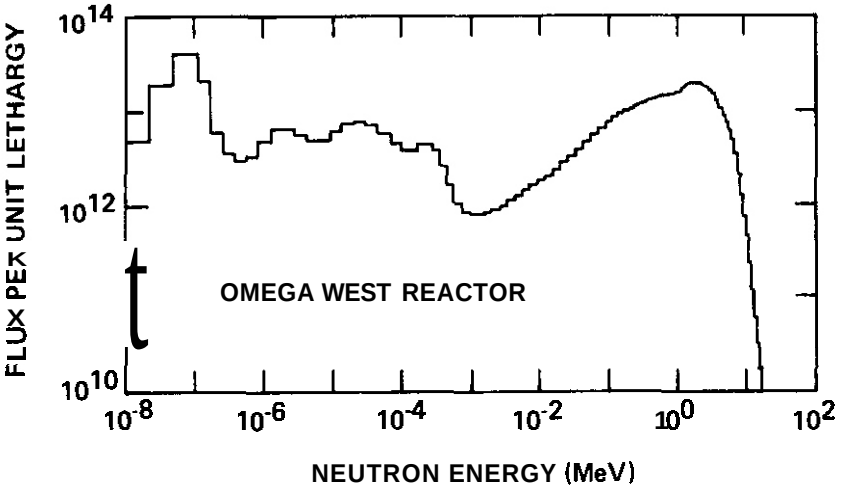

FIGURE 1. Unfolded Flux Spectrum for the Omega West Reactor at 8 MW, Core Center.

are consistent with the ENDF/B-V radiometric cross sections. The $^{10}B(n,\alpha)$ results are also in excellent agreement, but this analysis does not provide an independent cross section test, because the ^{10}B concentration of the Al-B alloy was originally determined relative to the ^{6}Li content of the Al-Li alloy, in a separate thermal neutron irradiation.

This OWR experiment utilized a large number of radiometric reactions, and spectral unfolding without the helium data generated a nearly identical spectrum. The helium accumulation measurements were included here primarily to demonstrate the combined unfolding and the consistency of the spectrum-integrated cross sections. Long-term reactor experiments now in progress in the High Flux Isotopes Reactor (HFIR) and the Oak Ridge Research Reactor (ORR), on the other hand, have limited radiometric dosimetry, due to long irradiation times and burn-up by the high fluxes. Helium accumulation is expected to contribute significantly to the spectral unfolding for these irradiations.

6.0 References

1. L. R. Greenwood, "Characterization of the Omega West Reactor (LASL)," Damage Analysis and Fundamental Studies, Quarterly Progress Report October-December 1980, DOE/ER-0046/4, Vol. 1, U.S. Department of Energy, 16 (1981).

TABLE 2

DOSIMETRY REACTIONS USED FOR OWR SPECTRAL UNFOLDING

Reaction		Energy Range* (MeV)	Average Deviation†
$^{6}Li(n,X)helium$		1×10^{-9} - 4×10^{-7}	-0.1%
$^{10}B(n,X)helium$		1×10^{-9} - 4×10^{-7}	+0.0%
$^{45}Sc(n,\gamma)^{46}Sc$		1×10^{-9} - 4×10^{-7}	-5.7%
$^{59}Co(n,\gamma)^{60}Co$		1×10^{-9} - 1×10^{-4}	+1.8%
$^{58}Fe(n,\gamma)^{59}Fe$		1×10^{-9} - 2×10^{-4}	+4.1%
$^{176}Lu(n,\gamma)^{177}Lu$		1×10^{-8} - 1×10^{-7}	+4.3%
$^{197}Au(n,\gamma)^{198}Au$		1×10^{-8} - 4×10^{-6}	-1.1%
$^{235}U(n,f)$		1×10^{-8} - 2×10^{-6}	+0.5%
$^{238}U(n,\gamma)^{239}U$		2×10^{-8} - 2×10^{-4}	-4.0%
$^{176}Lu(n,\gamma)^{177}Lu$	**	8×10^{-8} - 9×10^{-6}	+7.2%
$^{45}Sc(n,\gamma)^{46}Sc$	**	8×10^{-8} - 2×10^{-5}	-2.4%
$^{10}B(n,X)helium$	**	8×10^{-8} - 2×10^{-5}	+0.5%
$^{6}Li(n,X)helium$	**	8×10^{-8} - 3×10^{-5}	-2.4%
$^{59}Co(n,\gamma)^{60}Co$	**	8×10^{-8} - 1×10^{-4}	-0.6%
$^{58}Fe(n,\gamma)^{59}Fe$	**	8×10^{-8} - 3×10^{-4}	+3.8%
$^{235}U(n,f)$	**	8×10^{-8} - 3×10^{-4}	+1.3%
$^{63}Cu(n,\gamma)^{64}Cu$	**	8×10^{-8} - 7×10^{-3}	-8.3%
$^{237}Np(n,\gamma)^{238}Np$	**	1×10^{-7} - 1×10^{-4}	+15.2%
$^{197}Au(n,\gamma)^{198}Au$	**	8×10^{-7} - 6×10^{-6}	+1.1%
$^{238}U(n,\gamma)^{239}U$	**	4×10^{-6} - 2×10^{-4}	-0.2%
$^{237}Np(n,f)$		0.36 - 5.0	+1.6%
$^{238}U(n,f)$		1.4 - 6.0	-0.1%
$^{54}Fe(n,p)^{54}Mn$		2.0 - 6.7	+1.3%
$^{58}Ni(n,p)^{58}Co$		2.0 - 6.7	-4.2%
$^{46}Ti(n,p)46Sc$		3.7 - 9.0	-1.6%
$^{60}Ni(n,p)^{60}Co$		4.5 - 10	-9.1%
$^{63}Cu(n,\alpha)^{60}Co$		4.5 - 10	+2.6%
$Cu(n,X)helium$		5.0 - 11	+4.0%
$^{54}Fe(n,\alpha)51Cr$		5.0 - 11	+6.4%
$^{48}Ti(n,p)^{48}Sc$		5.5 - 12	+6.1%
$^{27}Al(n,\alpha)24Na$		6.0 - 12	-1.3%
$^{93}Nb(n,2n)^{92m}Nb$		9.0 - 14	+3.3%
$^{55}Mn(n,2n)54Mn$		11 - 17	+1.8%
$^{90}Zr(n,2n)^{89}Zr$		12 - 18	-4.1%

*90% response range

†Percentage deviation of measured from calculated reaction integral

**Gadolinium cover foil

2. F. G. Perey, Least Squares Dosimetry Unfolding: The Program STAY'SL, ORNL/TM-6062, Oak Ridge National Laboratory (1977); as modified by L. R. Greenwood, Argonne National Laboratory (1979).

3. National Nuclear Data Center, Brookhaven National Laboratory.

7.0 Future Work

Mixed-spectrum reactor dosimetry development and use will continue, with near-term analysis emphasis on current ORR and HFIR experiments.

8.0 Publications

A paper entitled "A Review of Helium Accumulation Neutron Dosimetry for Fusion Neutron Test Environments," by D. W. Kneff, H. Farrar IV, and L. R. Greenwood, was presented at the Fourth ASTM-EURATOM Symposium on Reactor Dosimetry, Gaithersburg, Maryland, on March 24, 1982, and has been submitted for publication in the symposium proceedings.

COMBINED HELIUM ACCUMULATION AND RADIOMETRIC DOSIMETRY FOR Be(d,n) NEUTRON SPECTRA

L. R. Greenwood (Argonne National Laboratory), D. W. Kneff, and H. Farrar IV (Rockwell International, Energy Systems Group)

1.0 Objective

The objectives of this work are to characterize the Be(d,n) neutron environment and to develop helium accumulation and radiometric neutron dosimeters for routine neutron fluence and energy spectrum measurements in Be(d,n) and Li(d,n) neutron fields.

2.0 Summary

Neutron energy spectrum unfolding using combined helium accumulation and radiometric measurements has been demonstrated for the Be(d,n) neutron environment.

3.0 Program

Title: Dosimetry and Damage Analysis/Helium Generation in Fusion Reactor Materials

Principal Investigators: L. R. Greenwood, D. W. Kneff, and H. Farrar IV

Affiliation: Argonne National Laboratory and Rockwell International

4.0 Relevant DAFS Program Plan Task/Subtask

Subtask II.A.2.1 Flux-Spectral Definition in the Be(d,n) Field

5.0 Accomplishments and Status

Combined helium accumulation-radiometric neutron dosimetry spectral unfolding has now been performed for the Be(d,n) neutron environment produced by 30-MeV

deuterons. The objective of the work was to demonstrate the use of the measured dosimetry data from both techniques in spectral unfolding calculations. Such combined spectral unfolding is being developed for the characterization of, and routine dosimetry in, the neutron irradiation field of the Fusion Materials Irradiation Test Facility (FMIT). The calculations were performed using dosimetry data derived from a Be(d,n) characterization experiment that has been described in detail previously.[1]

Spectral unfolding was performed at 0° (relative to the deuteron beam axis) at a distance of 17 mm from the center of the beryllium target. This location corresponds to the front face of a stack of radiometric dosimetry foils. The helium analysis results from seven Al, Fe, and Cu pure element dosimetry rings located near this foil stack were geometrically extrapolated to the plane of the foils. The spectral unfolding code STAY'SL was used for the analysis,[2] and the dosimetry reactions used are listed in Table 1. Radiometric cross sections for neutron energies $\leq$ 20 MeV were based on ENDF/B-V,[3] and cross sections > 20 MeV were taken from Ref. 4. ENDF/B-V (n,α) cross sections were used for Cu and Al helium production below the (n,nα) thresholds (~12 MeV), and the (n,total helium) statistical model calculations of F. M. Mann were used at higher energies.[5] The Fe(n,total helium) cross section was taken from Arthur and Young.[6] The resulting unfolded neutron energy spectrum is shown in Figure 1.

The results demonstrate the feasibility of using combined helium accumulation/radiometric spectrum unfolding for broad fast-neutron energy distributions. In the present case, the helium accumulation materials used in the unfolding were based in part on the availability of energy-dependent total helium production cross section information. The unfolding demonstrates their similar energy sensitivities (Table 1). Future work will investigate materials with different expected energy responses, such as gold for higher energies, and emphasis will be placed on materials that can be analyzed for both activation yields and helium generation (e.g., Co, Ni, Au).

TABLE 1

DOSIMETRY REACTIONS USED FOR Be(d,n) NEUTRON SPECTRUM UNFOLDING

Reaction	Energy Range* (MeV)	Average Deviation†
$^{59}Co(n,\gamma)^{60}Co$	10^{-4} - 13.5	-1.9%
$^{197}Au(n,\gamma)^{198}Au$	10^{-3} - 4.0	-0.1%
$^{58}Ni(n,p)^{58}Co$	3.0 - 17.5	+6.6%
$^{54,56}Fe(n,X)^{54}Mn$	3.5 - 25	-6.8%
$^{59}Co(n,p)^{59}Fe$	6.5 - 19	-2.6%
$^{60}Ni(n,p)^{60}Co$	7.0 - 19.5	+9.1%
$^{27}Al(n,\alpha)^{24}Na$	8.5 - 18.5	-0.9%
$^{54}Fe(n,\alpha)^{51}Cr$	8.5 - 22	-2.7%
Fe(n,X)helium	8.5 - 25	+16.0%
Al(n,X)helium	9.0 - 25	+0.6%
Cu(n,X)helium	9.0 - 26	-1.9%
$^{197}Au(n,2n)^{196}Au$	10 - 20	+0.5%
$^{93}Nb(n,2n)^{92m}Nb$	10.5 - 20	-12.0%
$^{59}Co(n,2n)^{58}Co$	12 - 23	-3.8%
$^{90}Zr(n,2n)^{89}Zr$	13 - 25	-1.1%
$^{58}Ni(n,2n)^{57}Ni$	13.5 - 24	+15.4%
$^{197}Au(n,3n)^{195}Au$	17 - 27	-10.2%
$^{59}Co(n,3n)^{57}Co$	21 - 30	+3.8%
$^{197}Au(n,4n)^{194}Au$	25 - 32	+1.5%

*90% response range

†Percentage deviation of measured from calculated reaction integral

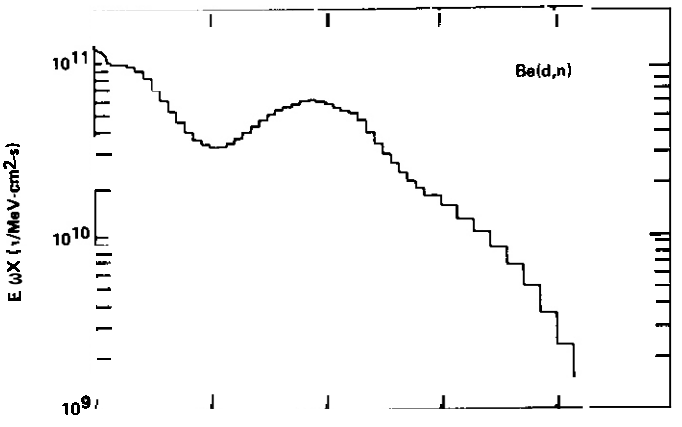

FIGURE 1.

6.0 References

1. D. W. Kneff, H. Farrar IV, L. R. Greenwood, and M. W. Guinan, "Characterization of the Be(d,n) Neutron Field by Passive Dosimetry Techniques," in Proc. Symp. on Neutron Cross-Sections from 10 to 50 MeV, M. R. Bhat and S. Pearlstein (Eds), BNL-NCS-51245, Brookhaven National Laboratory, N.Y. (1980), p. 113.

2. F. G. Perey, Least Squares Dosimetry Unfolding: The Program STAY'SL, ORNL/TM-6062, Oak Ridge National Laboratory (1977); as modified by L. R. Greenwood, Argonne National Laboratory (1979).

3. National Nuclear Data Center, Brookhaven National Laboratory.

4. L. R. Greenwood, Extrapolated Neutron Activation Cross Sections for Dosimetry to 44 MeV, ANL/FPP/TM-115, Argonne National Laboratory (1978).

5. D. W. Kneff, H. Farrar IV, F. M. Mann, and R. E. Schenter, "Experimental and Theoretical Determination of Helium Production in Copper and Aluminum by 14.8-MeV Neutrons," Nucl. Technol., 49, 498 (1980).

6. E. D. Arthur and P. G. Young, Evaluated Neutron-Induced Cross Sections for ^{54,56}Fe to 40 MeV, LA-8626-MS, Los Alamos National Laboratory (1980).

7.0 Future Work

Since this Be(d,n) irradiation experiment included a sufficiently large number of radiometric dosimetry reactions to extensively characterize the neutron field, the emphasis on further helium work will be on integrally testing (n,total helium) cross section evaluations by comparison with the helium measurements. Comparisons made at several neutron source angles are expected to provide some energy-dependent information, since the neutron energy spectrum changes rapidly with source angle.

8.0 Publications

A paper entitled "A Review of Helium Accumulation Neutron Dosimetry for Fusion Neutron Test Environments," by O. W. Kneff, H. Farrar IV, and L. R. Greenwood, was presented at the Fourth ASTM-EURATOM Symposium on Reactor Dosimetry, Gaithersburg, Maryland, on March 24, 1982, and has been submitted for publication in the symposium proceedings.

NEUTRON DOSIMETRY MEASUREMENTS FOR THE HFIR-CTR32 IRRADIATION

L. R. Greenwood and R. K. Smither (Argonne National Laboratory)

1.0 Objective

To establish the best practicable dosimetry for fission reactors and to provide dosimetry and damage analysis for OFE experiments.

2.0 Summary

Results are presented for the HFIR-CTR32 irradiation. The maximum fluence was 4.80 x 10^{22} n/cm^2 (1.24 x 10^{22} n/cm^2 above 0.1 MeV). The status of all other fission reactor dosimetry is summarized in Table I.

3.0 Program

Title: Dosimetry and Damage Analysis

Principal Investigator: L. R. Greenwood

Affiliation: Argonne National Laboratory

4.0 Relevant DAFS Program Plan Task/Subtasks

Task II.A.l Fission Reactor Dosimetry

5.0 Dosimetry Results for the HFIR-CTR32 Irradiation

The CTR32 irradiation in the PTP of the High Flux Isotopes Reactor (HFIR) at Oak Ridge National Laboratory was conducted from August 17, 1980 to December 12, 1980 for a total exposure of 124 days (10,863 MWD). dosimeters were inserted at 12 vertical heights in the experiment. Six of the dosimetry

Table I

Status of Reactor Experiments

Facility/Experiment		Status/Comments
ORR	- MFE1	Completed 12/79
	- MFE2	Completed 06/81
	- MFE4A	Completed 12/81
	- MFE4B, C	Irradiation in Progress
	- TBC07	Completed 07/80
	- TRIO - Test	Irradiations in Progress
AFIR	- CTR32	Completed 04/82
	- CTR30, 31, 34, 35	Irradiations in Progress
	- T1, T2, T3	Irradiations in Progress
	- RB1, RB2, RB3	Irradiations in Progress
	- CTR39, 40, 41	Planning in Progress
Omega West	- Spectral Analysis	Completed 10/80
	- HEDL 1	Completed 05/81
EBR II	- X287	Completed 09/81
IPNS	- LASL 1 (Hurley)	Irradiation 02/82

capsules contained radiometric monitors (Ni, Cu, 0.1% Co-Al, 80% Mn-Cu, Nb, Ti, and Fe). The other six capsules contained helium accumulation monitors supplied by Rockwell International (Fe, Ni, Cu, Nb, Ti). All of the samples were gamma counted at ANL. The helium monitors as well as some of the radiometric samples were then sent to Rockwell for helium analysis.

The radiometric dosimetry results are given in Table II. Burnup corrections were applied to all of the reactions, although most corrections were <10 percent. The $^{59}Co(n,\gamma)$ and $^{58}Fe(n,\gamma)$ reactions require significant corrections, 20-30% for cobalt and 10-20% for iron. In the iron case, the largest correction is due to double capture in ^{57}Fe. A self-consistency test insures that these burnup corrections are quite accurate (~2%). This is also confirmed by the excellent agreement between the various thermal neutron reactions. The corrections to ^{54}Mn from the $^{54}Fe(n,p)$ and $^{55}Mn(n,2n)$ reactions are uncertain since the ^{54}Mn thermal cross section is not known (<10 barns). If we assume an average cross section of 5 barns, then the ^{54}Mn corrections have an uncertainty of ±4%. All other corrected activities are accurate to ±2%.

The STAYSL computer code was used to determine flux and spectral values. The activation rates in Table I were used to adjust a HFIR spectrum calculated by Kam and Swanks.[1] Excellent agreement was found between this spectrum and our dosimetry results (Table II). The final adjusted spectrum is shown in Figure 1. Fluence values are listed in Table III. Vertical fluence gradients were also determined from the data in Table I and these gradients are shown in Figure 2.

Table II

Activation Rates for HFIR-CTR32

Height, cm	$\sigma\phi$(atom/atom-s) (100 MW)					
	$^{59}Co(n,\gamma)$ ($\times 10^{-8}$)	$^{58}Fe(n,\gamma)$ ($\times 10^{-9}$)	$^{54}Fe(n,p)$ ($\times 10^{-11}$)	$^{46}Ti(n,p)$ ($\times 10^{-12}$)	$^{55}Mn(n,2n)$ ($\times 10^{-13}$)	$^{63}Cu(n,\alpha)$ ($\times 10^{-13}$)
20.8	4.18	1.27	4.13	--	1.23	3.11
16.7	--	1.37	5.22	--	--	--
12.5	5.56	1.70	6.44	9.43	1.94	4.42
4.2	7.21	2.17	6.99	10.46	2.13	4.84
0.0	--	--	--	10.34	--	--
-4.2	7.28	2.19	6.86	10.23	2.10	4.83
-8.3	--	1.87	6.77	--	--	--
-12.5	5.76	1.75	6.08	8.89	1.83	5.11
-16.7	--	--	--	7.28	--	--
-20.8	4.22	1.21	3.86	5.66	1.23	2.88

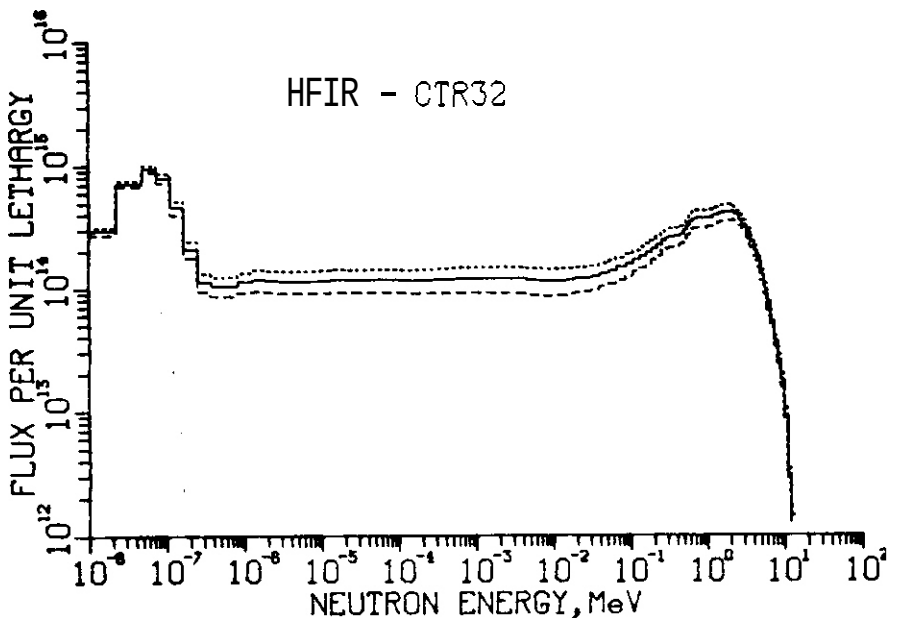

Figure 1. Measured neutron spectrum for the HFIR-CTR32 experiment at midplane of the PTP. The dotted and dashed lines show the standard deviations *to* group fluxes; however, correlations are very strong

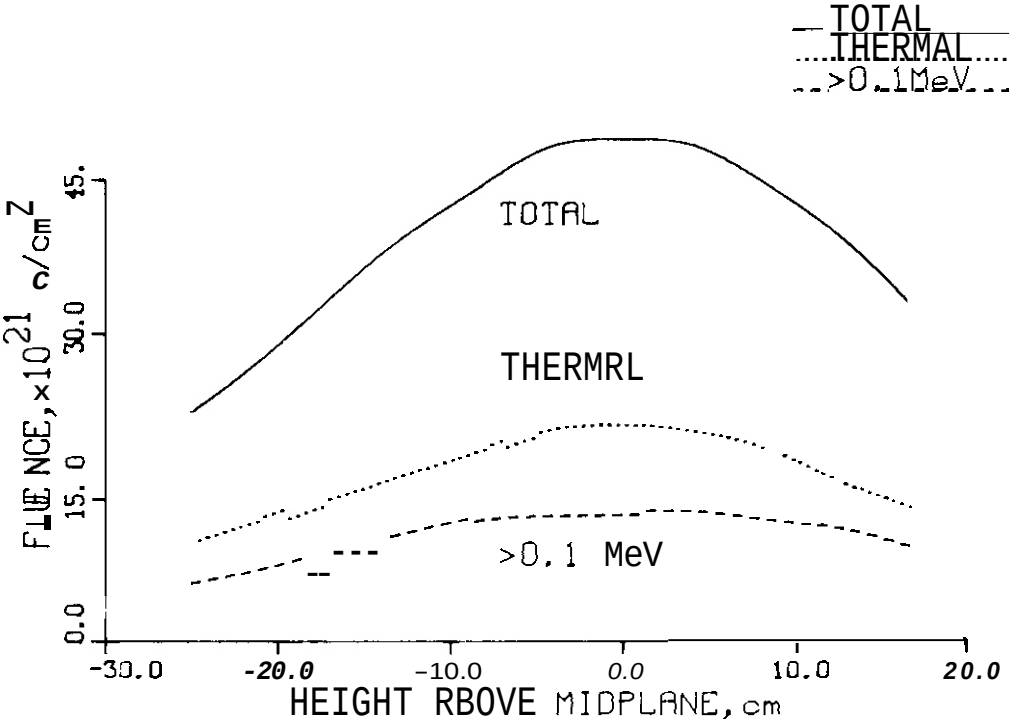

Figure 2. Fluence gradients measured during the HFIR-CTR32 irradiation

Table III

Neutron Fluences for HFIR-CTR32

Height, cm	Fluence, x 10^{21} n/cm^2		
	Total (±5%)	Thermal (±5%)	>0.1 MeV (±8%)
-25.0	22.2	9.5	5.7
-20.8	27.5	11.8	7.1
-16.7	33.6	14.0	8.9
-12.5	39.4	16.2	10.6
-8.3	44.1	17.8	12.1
-4.2	48.0	20.5	12.5
0.0	48.7	21.0	12.6
4.2	48.0	20.3	12.6
8.3	44.4	18.7	11.8
12.5	39.4	15.6	10.9
16.7	32.7	12.9	9.1
20.8	28.1	11.8	7.4

Displacement damage rates were computed using the adjusted spectra and our revised displacement damage cross sections which were recently put into the NMFE Computer at Lawrence Livermore Laboratory. The spectral-averaged displacement and helium generation rates are listed in Table IV. The experimental experimental helium values will be measured by Rockwell International

The nickel two-step, thermal production of helium was computed assuming the formulation for HFIR of T. Gabriel (ORNL/TM-6361, 1979). The correctness of this procedure is currently being reexamined and the calculations may change slightly. However, experimental values will also be provided by Rockwell.

The thermal neutron capture reaction in nickel also leads to a substantial increase in displacement damage, a point which has been neglected in previous calculations. The Q-value for the $^{59}Ni(n,\alpha)^{56}Fe$ reaction is 5.097 MeV. Hence, thermal neutrons produce a 340 keV ^{56}Fe recoil and a 4757 keV alpha. Using the Lindhard energy partition model and a cut-off of 40 eV, one find that each thermal capture produces 1763 displacements (1701 from ^{56}Fe and 62 from the alpha). If we compute the helium production in nickel, then we can easily determine this extra number of displacements, as follows:

$$\text{DPA}\ (n,\alpha) = \frac{\text{He (appm in Ni)}}{567} \qquad (1)$$

This equation holds for all thermal irradiations and can be used to correct all previous experiments (e.g., in ORR). In the present case at midplane, the usual calculations for Ni gives 9.71 DPA and 41 appm He. Double thermal neutron capture produces 2897 appm He and an additional 5.11 DPA. Hence, neglecting this effect would cause us to underpredict the nickel DPA value by

Table IV

Damage Parameters for HFIR-CTR32
He in appm, DPA = displacements per atom, (n,γ) included
Values accurate to ±10%

Height, cm:	20.8		12.5		4.2	
Element	DPA	He	DPA	He	DPA	He
Al	9.59	4.67	14.26	6.73	16.21	7.45
Ti	6.03	3.09	9.16	4.67	10.39	5.16
V	6.78	0.15	10.12	0.22	11.49	0.25
Cr	6.01	1.07	8.99	1.57	10.18	1.73
Mn[a]	6.62	0.89	9.81	1.29	11.21	1.43
Fe	5.32	1.82	7.97	2.64	9.01	2.92
Co[a]	6.73	0.93	9.82	1.35	11.43	1.49
Nib	7.80	1196.	11.85	1922.	14.82	2938.
cu	5.18	1.65	7.73	2.39	8.77	2.64
Nb	5.13	0.35	7.65	0.51	8.66	0.56
316 SS[c]	5.70	121.	8.55	194.	9.82	296.

[a](n,γ) effect is 8.4% for Mn and 27.6% for cobalt: however, corrections for neutron self-shielding effects may be required!

[b]Nickel includes thermal neutron capture helium and DPA effect (see text)

[c]316 SS: Cr(16), Mn(2), Fe(70), Ni(10), Mo(2)

53%! In 316 SS the effect increases the net DPA value by 6-8%. In longer irradiations, this effect will be even more important, especially if one is trying to tailor He/DPA ratios to fusion values!

It should also be noted that the DPA rates in Table IV include (n,γ) effects, but not beta-decay. This omission will be corrected in our files and new values will be calculated. In any case, great caution must be used with the (n,γ) contributions due to neutron self-shielding effects, especially for Mn and Co.

6.0 References

1. F. B. K. Kam and J. H. Swanks, Neutron Flux Spectrum in the HFIR Target Region, ORNL-TM-3322 (1971).

7.0 Future Work

At least 13 additional experiments are now planned or in progress in HFIR (see Table I). Helium data will also be integrated with our radiometric data to improve our knowledge of the HFIR flux-spectrum and to integrally test our helium cross sections.

8.0 Publications

1. L. R. Greenwood, Neutron Flux and Spectral Measurements to Characterize Irradiation Facilities for Fusion Materials Studies, Proceedings of the Fourth ASTM-EURATOM Symposium on Reactor Dosimetry, March 22-26, 1982, National Bureau of Standards, Gaithersburg, MD

THE IMPACT OF THE $^{59}Ni(n,\alpha)^{56}Fe$ REACTION ON DAMAGE CALCULATIONS FOR HFIR

F. A. Garner and F. M. Mann (Hanford Engineering Development Laboratory)

1.0 Objective

The object of this effort is to determine the appropriate method of comparison of HFIR and EBR-II displacement exposures, and the extrapolation to fusion conditions of experimental results derived from these reactors.

2.0 Summary

Greenwood and Smither have recently shown that the contribution of the $^{59}Ni(n,\alpha)^{56}Fe$ reaction to displacement damage has been overlooked. When included in calculations of HFIR-induced displacement levels, there are substantial consequences. The displacement level is increased measurably and the helium/dpa ratio correspondingly reduced. However, the additional contribution to the damage rate is nonuniform both in time and space.

3.0 Program

Title: Irradiation Effects Analysis (AKJ)
Principal Investigator: D. G. Doran
Affiliation: Hanford Engineering Oevelopment Laboratory

4.0 Relevant OAFS Program Plan Task/Subtask

II.C.I Effect of Material Parameters on Microstructure
II.C.2 Effect of Helium on Microstructure
II.C.4 Effect of Solid Transmutants on Microstructure

5.0 Accomplishments and Status

5.1 Introduction

In a recent report Greenwood and Smither have noted that the currently employed method of calculating the displacement damage for irradiated steels neglect an important source of displacement damage.[1] The production of helium in nickel in thermal reactors involves the $^{59}Ni(n,\alpha)^{56}Fe$ reaction with an energy release of 5.097 MeV, shared between the ^{56}Fe (4.757 MeV) and alpha particle (340 keV). Greenwood calculates that this leads to 1701 displacements from ^{56}Fe and 62 displacements from the alpha particle per reaction.

The displacements caused by this reaction can be calculated from the following formula.[1]

$$DPA\ (n,\alpha) = \frac{(He\ (appm)\ from\ the\ Ni^{59}\ reaction) \times \left(\frac{Mole\ Fraction}{Nickel}\right)}{567}$$

Since comparisons have recently been made of the damage generated in the DO-heat of AISI 316 stainless steel by irradiation in the HFIR and EBR-II reactors,[2-3] it was decided to assess the impact of this reaction for both pure nickel and the DO-heat (13% nickel).

5.2 Calculational Assumptions

The impact of the $^{59}Ni(n,\alpha)$ reaction on metals irradiated in EBR-II is rather small since the low level of slow neutrons in EBR-II does not lead to substantial formation of ^{59}Ni from ^{58}Ni.

The calculation for HFIR concentrates on the PTP position with an assumed displacement cross section (exclusive of the $Ni^{59}(n,\alpha)$ reaction) of 200 barns per total neutron.[4] The helium level as a function of dose is taken from Reference 5 and represents the most up-to-date determination of cross sections and helium levels. Figure 1 is reproduced from Reference 5 and shows the helium concentration as a function of the original ^{58}Ni concentration and fluence.

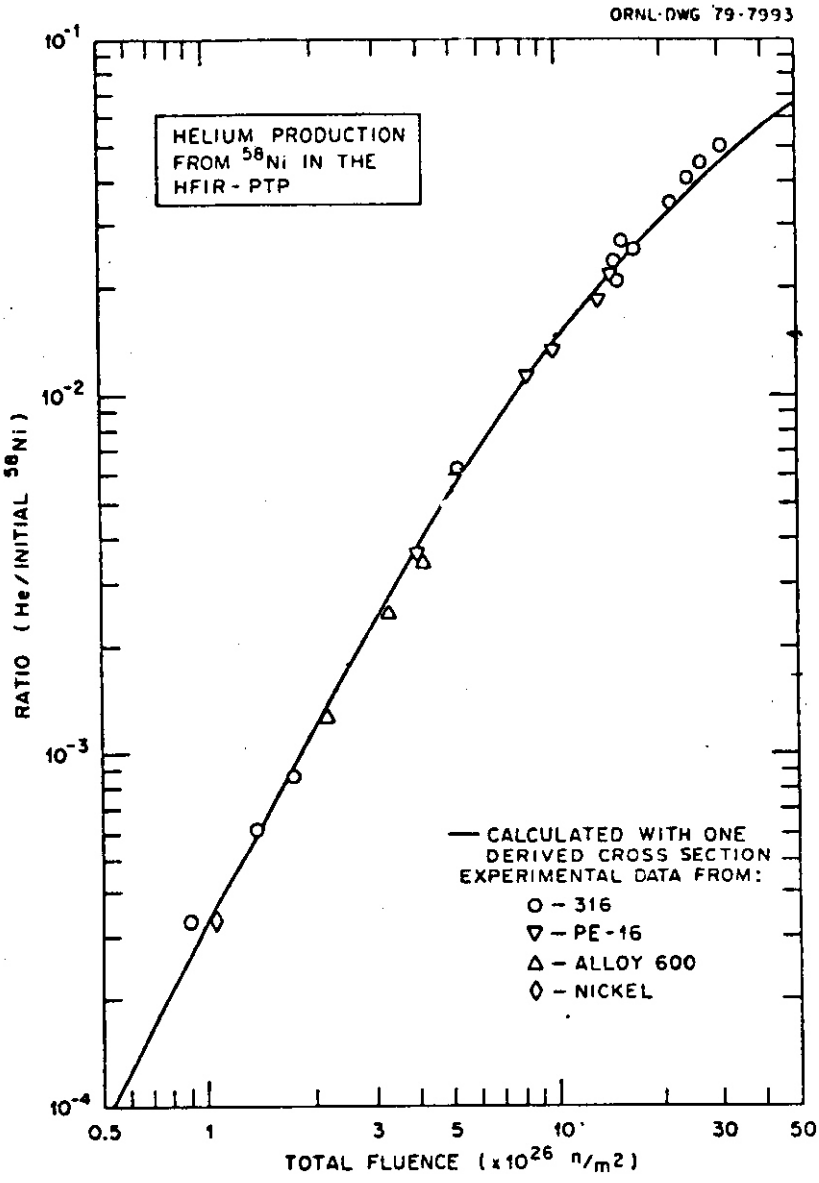

FIGURE 1. Helium Production From ^{58}Ni by Two Thermal Neutron Captures, as Reported by Wiffen and Coworkers.(5) The helium is given as a fraction of the initial concentration of ^{58}Ni. This curve is valid only for the PTP position of HFIR.

5.3 Results of Calculations

Table 1 is a compilation of the displacement calculations for nickel and the DO-heat of steel. Note in Figure 2 that the calculated displacement level essentially doubles in pure nickel when the $^{59}Ni(n,\alpha)^{56}Fe$ reaction is included. For DO-heat AISI 316 the maximum increase in displacement level is just over 12%.

Figure 3 emphasizes the fact that the percentage contribution of the $^{59}Ni(n,\alpha)^{56}Fe$ reaction changes strongly with time, peaking at 93% around a dose of 20 dpa, when calculated with the currently employed displacement model. As shown in Figure 4, 20 dpa is the dose at which the Ni^{59} concentration peaks.[6] This means that this additional contribution to the displacement rate varies strongly with time.

5.4 Discussion

There are a number of ramifications of this analysis that are pertinent to the comparison of HFIR and EBR-II data as well as the development of fission-fusion correlations.

(1) In the comparison of HFIR and EBR-II swelling data for AISI 316, the HFIR data should have their quoted doses increased ~12% in the 30-50 dpa range. Since the swelling of this steel is dominated by a long incubation-transient regime, the impact of the additional fluence on the predicted swelling will be greater than 12%, however.

(2) The comparison of data from the two reactors assumes that the irradiation proceeds at essentially constant neutron flux and displacement rate. While the former is relatively constant, the latter now is known to vary strongly with time in HFIR. Since many of the components of the microstructural/microchemical evolution are sensitive to displacement rate, there is bound to be some as-yet unidentified consequences in the swelling, creep rate, etc.

TABLE 1

ADDITIONAL DISPLACEMENTS (DPA*) FORMED DURING IRRADIATION IN HFIR-PTP BY THE $^{59}Ni(n,\alpha)^{56}Fe$ REACTION

Total Fluence x 10^{22} n/cm^2	Pure Nickel			AISI 316	
	DPA	DPA*	Percent Increase	DPA*	Percent Increase
1.0	2.00	0.40	20	0.05	2.5%
1.5	3.00	0.85	28	0.11	3.7%
2.0	4.00	1.42	36	0.18	4.5%
3.0	6.00	2.87	48	0.37	6.2%
4.0	8.00	4.60	58	0.60	7.5%
5.0	10.00	6.51	65	0.85	8.5%
6.0	12.00	8.54	71	1.11	9.2%
8.0	16.00	12.77	80	1.66	10.4%
10.0	20.00	17.07	85	2.22	11.1%
15.0	30.00	27.47	92	3.57	11.9%
20.0	40.00	37.13	93	4.83	12.1%
30.0	60.00	54.06	90	7.03	11.7%
40.0	80.00	68.34	85	8.88	11.1%
50.0	100.00	80.24	80	10.43	10.4%
60.0	120.00	89.76	75	11.67	9.7%
80.0	160.00	105.40	66	13.70	8.6%

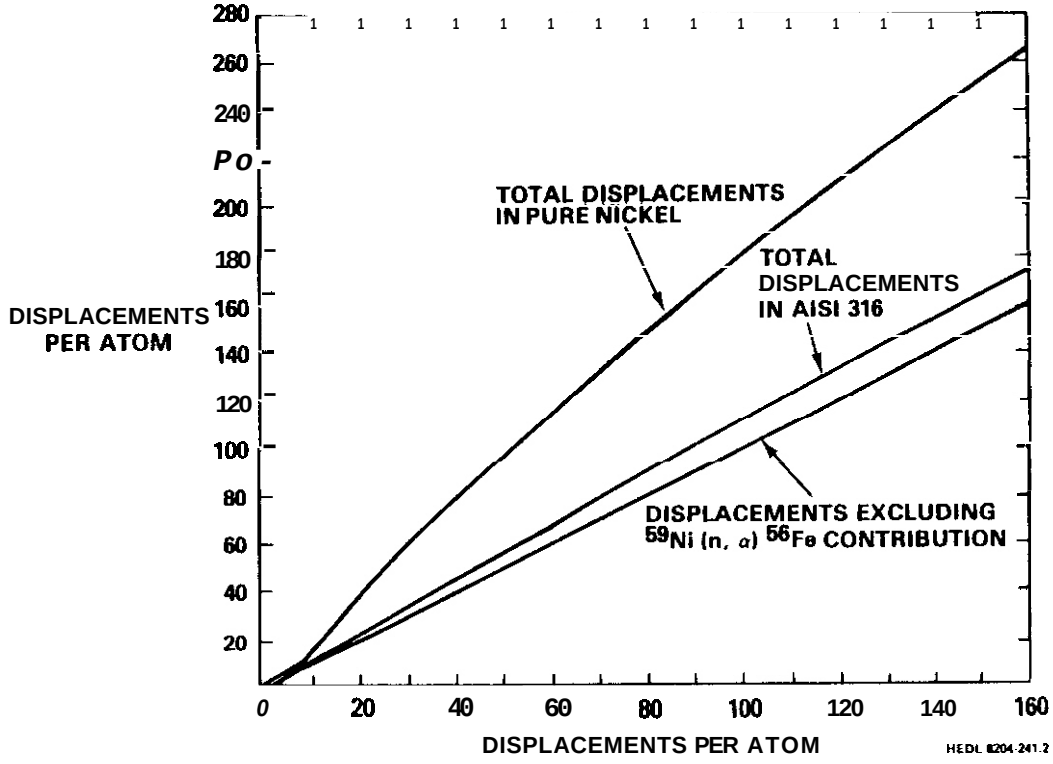

FIGURE 2. Comparison of the Displacement Levels Calculated for Pure Nickel and AISI 316, Calculated Both With and Without Inclusion of the $^{59}Ni(n,\alpha)^{56}Fe$ Contribution.

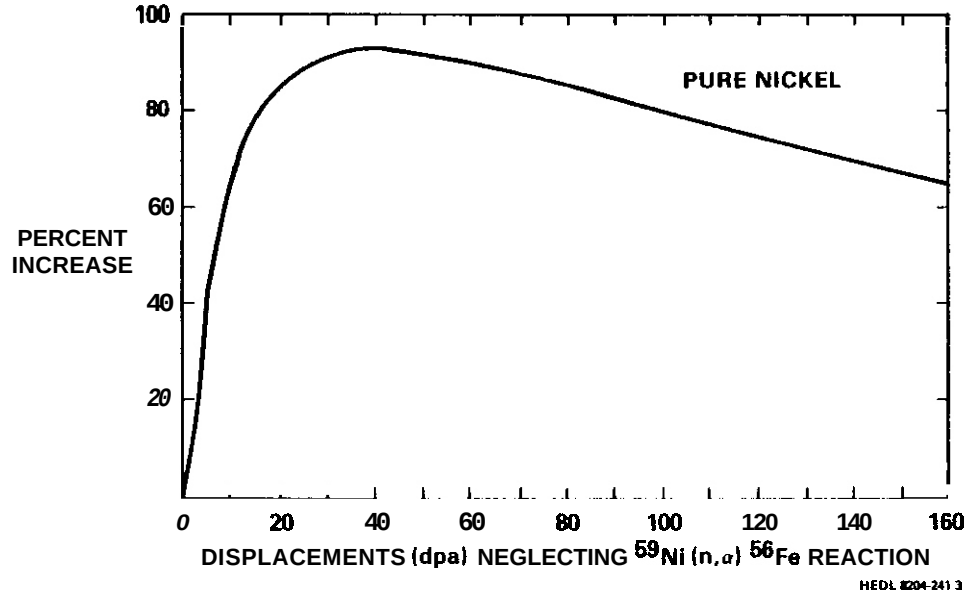

FIGURE 3. Percentage Increase in Calculated Displacement Level for Pure Nickel as a Function of Fluence in HFIR-PTP. To obtain percentage increase for AISI 316 multiply by 0.13, the fraction of nickel. AISI 316 therefore peaks at an increase of 12.1%.

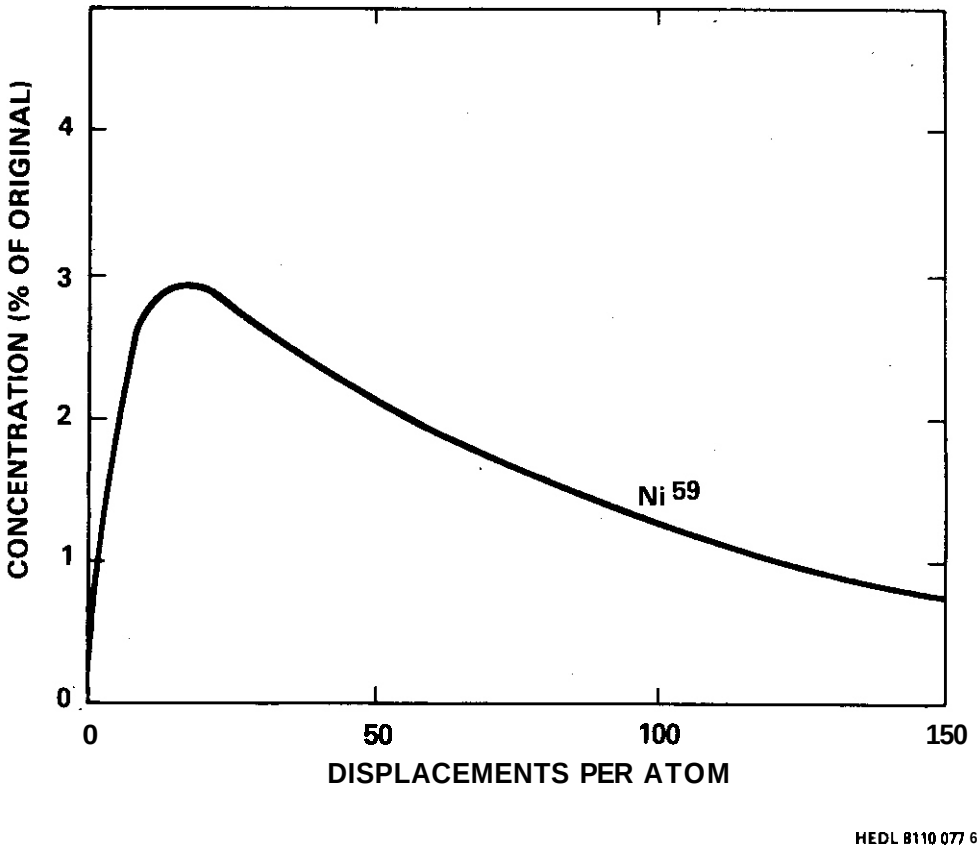

FIGURE 4. Time-Dependent Concentration *of* ^{59}Ni That Arises During HFIR-PTP Irradiation of Pure Nickel. (6) The time-dependent volume-averaged rate of additional displacements will be proportional to the ^{59}Ni concentration.

(3) Not only is the displacement level in HFIR nonuniform in time but it is also nonuniform spatially. Nickel segregates to very high levels in the precipitates of AISI 316 (75% in γ' and 55% in G-phase). This means that nickel-rich precipitates and their immediate surroundings will be subjected tohigherdose levels than that experienced by the matrix containing lower nickel levels.

(4) Since the recoiling ^{56}Fe atom has a mean range of ~800 Å and most precipitate radii are smaller, the iron atom in general will come to rest outside the precipitate. The higher level (compared to the matrix) of PKA's generated within the precipitate will cause the precipitate to accumulate a net excess of vacancies. During HFIR irradiation this excess may account

partially for the fact that precipitates are ideal sites for void nucleation. There will, of course, be an net excess of interstitials just outside the precipitates. An analysis of this phenomenon is now in progress. This process may lead to a change in precipitate stability in various fission reactors.

(5) The conclusions drawn above are specific to the PTP position in HFIR. In more thermalized positions such as A2, HT-5, the impact of this phenomenon is expected to be even greater.

(6) Another conclusion of this analysis is that the helium/dpa ratio in HFIR is lowered by the contribution of the $^{59}Ni(n,\alpha)^{56}Fe$ reaction. This means that the use of HFIR, particularly for pure nickel or high nickel levels, more closely approaches the helium/dpa level typical of fusion spectra.

(7) The range of the alpha particle is so large (compared to the mean distance between precipitates) that the segregation of nickel does not lead to any substantial segregation of the deposited helium. This conclusion is derived from previous analysis of the "helium-halo" effect.(7-8)

(8) For the ADIP long range alloys LRO-15 (20% nickel) and LRO-16 (31% nickel) the impact of the ^{59}Ni displacement contribution will be larger than that of AISI 316.

5.5 Conclusions

Greenwood and Smither have recently noted that the contribution of the $^{59}Ni(n,\alpha)^{56}Fe$ reaction to displacement damage has been overlooked. When included in calculations of HFIR-induced displacement levels, there are substantial consequences. The displacement level is increased measurably and the helium/dpa ratio correspondingly reduced. The additional contribution to the damage rate is nonuniform both in time and space however.

6.0 References

1. L. R. Greenwood and R. K. Smither, "Neutron Dosimetry Measurements for the HFIR-CTR3 Irradiation," this report.

2. H. R. Brager and F. A. Garner, "Comparison of the Swelling and the Microstructural/Microchemical Evolution of AISI 316 Irradiated in EBR-II and HFIR," Proc. Second Topical Meeting on Fusion Reactor Materials, Seattle, WA, August 9-12, 1981 (in press).

3. H. R. Brager and F. A. Garner, "Influence of Neutron Spectra on the Radiation-Induced Evolution in AISI 316," accepted for publication in J. Nucl. Mater.

4. J. F. Bates, F. A. Garner and F. M. Mann, "The Effect of Solid Transmutation Products on Swelling in 316 Stainless Steel," Proc. Second Topical Meeting on Fusion Reactor Materials, Seattle, WA, August 9-12, 1981 (in press).

5. F. W. Wiffen, E. J. Allen, H. Farrar, IV, E. E. Bloom, T. A. Gabriel, H. T. Kerr and F. G. Perey, "The Production Rate of Helium During Irradiation of Nickel in Thermal Neutron Spectrum Fission Reactors," submitted to J. Nucl. Mater.

6. F. A. Garner, F. M. Mann and H. R. Brager, "Measurement and Calculation of Solid Transmutants Formed in AISI 316," DAFS Quarterly Progress Report, DOE/ER-0046/7, November 1981, p. 198.

7. D. S. Gelles and F. A. Garner. "An Experimental Method to Determine the Role of Helium in Neutron-Induced Microstructural Evolution," J. Nucl. Mater., 85 and 86 (1979) 689.

8. F. A. Garner, "Determination of Helium Influence on Microstructural Development: Two Experimental Methods," DAFS Quarterly Progress Report, DOE/ER-0046/1, p. 225.

7.0 Future Work

This analysis will continue to assess the imact of this phenomenon on the development of fission-fusion correlations.

SOLID AND GAS TRANSMUTATION PRODUCTION CODE DEVELOPMENT (AKJ)

F. M. Mann (Hanford Engineering Development Laboratory)

1.0 Objective

The objective of this work is to develop and maintain a computer code system to calculate the amounts of solid and gas transmutants at various facilities used by OFE experimentalists.

2.0 Summary

The computer code REAC and its associated libraries have been expanded and used to determine transmutations in INTOR, UWMAK-1, FMIT, HFIR and FMIT.

3.0 Program

Title: Irradiation Effects Analysis (AKJ)
Principal Investigator: D. G. Doran
Affiliation: Hanford Engineering Development Laboratory

4.0 Relevant DAFS Program Plan Task/Subtask

Subtask II.A.4.5 Gas Generation Rates
Subtask II.C.4.1 Effects of Solid Transmutation Products on Microstructure

5.0 Accomplishments and Status

5.1 Introduction

When materials are placed in neutron environments, not only are atoms displaced from their sites, but transmutants are also produced. A code system called REAC has been developed to calculate transmutations for the various facilities that

OFE uses. This code system [1] has now been extended to be more useful and to include more facilities, more materials, and more cross sections.

5.2 Library Expansion

Cross sections for the stable isotopes of Ti, Mo, and W were obtained from the Livermore ACTL library [2] and from the HEDL modified THRESH2 code. These were processed and put into the multigroup cross section library. Also put into this library were damage energy cross sections processed by NJOY. [3]

Fluxes from INTOR were obtained from J. Jung of Argonne and the first wall spectrum was put into the flux library. Also included in the library is the fraction of the flux above 100 keV for each of the facilities.

PCA (prime candidate alloy) austenitic and HT-9 ferritic steels were added to the material library. Displacement energies were added for all the metals now in the library.

5.3 Code Extension

To aid the user, the exposure is now given in four units, total fluence (n/cm^2), fluence above 100 keV (n/cm^2), total damage energy produced (keV), and for metals the number of displacements per atom (dpa).

5.4 Typical Results

Transmutations as a function of dpa were calculated for PCA and HT-9 for the first wall of INTOR and UWMAK-1 and for FMIT, FFTF, and the PTP position of HFIR. Tables 1 and 2 show the transmutation at 50 dpa.

In general, the transmutation of INTOR, UWMAK-1, and FMIT are very similar. The exceptions are W and Re whose changes result from the relatively soft spectrum of INTOR causing $W(n,\gamma)\ W'\ (\beta^-)$ reactions. FFTF does not cause much transmutation, while HFIR produces significantly different transmutations

TABLE 1

TRANSMUTATIONS OF PCA AT 50 DPA

	Relative Change (%)				
Element[a]	HFIR-PTP	FFTF	INTOR	UWMAK-1	EMIT
Fe	1.4	0.45	-0.23	-0.21	-0.16
Ni	-0.51	-0.25	-1.3	-1.5	-1.5
Cr	-2.5	0.00	-0.13	-0.07	-0.18
Mn	-48.	-0.68	13.	13.	8.6
Mo	-1.8	-0.63	-0.64	-0.44	-0.25
Si	-0.03	0.00	-0.33	-0.36	-0.36
Ti	-0.11	0.02	+3.8	-3.9	+4.1
C	-0.01	0.00	-0.33	-0.37	-0.41

	New Elements (≥10 ppm in at least 1 facility)				
Element[b]	HFIR-PTP	FFTF	INTOR	UWMAK-1	EMIT
H	727	460	4300	4750	4800
He	4200	240	730	811	830
Mg	*	*	12	14	11
Al			21	22	24
V	3800	33	666	600	635
Co	431	174	460	613	1200
Cu	209[t]	*[3]	6	*	*
Nb			12	12	14
Tc	154	54	49	29	*[9]
Ru	60	20	9	5	

*Less than 1 ppm

[t] Probably slightly underpredicted because of lack of ^{63}Ni cross sections

[a] Listed in order of original number density

[b] Listed in order of mass number

TABLE 2

TRANSMUTATIONS OF HT-9 AT 50 DPA

Element[a]	Relative Change (%)				
	HFIR-PTP	FFTF	INTOR	UWMAK-1	EMIT
Fe	0.1	-0.01	-0.5	-0.5	-0.3
Cr	-1.5	0.02	-0.1	0.06	-0.03
C	-0.01	0.00	-0.3	-0.4	-0.4
Si	-0.3	0.00	-0.3	-0.3	-0.3
Mo	-1.a	-0.6	-0.7	-0.4	-0.3
Mn	-25.	0.5	70.	59.	39.
Ni	-0.3	-0.2	-1.4	-1.5	-1.5
V	55.	0.5	17.	+15.	16.
W	-31.	-1.1	-17.	-1.5	-0.4
P	-1.0	-0.005	-0.8	-0.9	-0.a

Element[b]	New Elements (ppm)				
	HFIR-PTP	FFTF	INTOR	UWMAK-1	EMIT
H	240.0	128	3100	3300	3300
He	150	11	590	630	690
Be	*	*	9	11	10
Mg	*	*	10	11	9
Al	*	*	17	18	19
Ti	*	*	118	121	128
co	211	9	21	20	38
Tc	76	24	25	14	5
Ru	29	9	5	2	*
Ta	2	*	8	10	4
Re	470	16	247	12	1

*Less than 1 ppm

[a]Listed in order of number density

[b]Listed in order of mass

than a fusion first wall for selected isotopes (e.g., Mn and V). Note that because of the low Ni content of HT-9, the helium production in HFIR for HT-9 caused by the $^{58}Ni(n,\alpha)^{59}Ni(n,\alpha)^{56}Fe$ is relatively small.

6.0 References

1. F. M. Mann, "Solid and Gas Transmutation Code Development," DAFS Quarterly Progress Report, DOE/ER-0046/6, April-June 1981.

2. M. A. Gardner and R. T. Howerton, ACTL: Evaluated Neutron Activation Cross Section Library - Evaluation Techniques and Reaction Index, UCRL-50400, Volume 18, Lawrence Livermore Laboratory, 1978.

3. F. M. Mann, "Calculation of Damage Parameters," DAFS Quarterly Progress Report, DOE/ER-0046/6, April-June 1981.

7.0 Future Work

Cross sections for selected long-lived isotopes for A-56 and for Cu will be added as well as fluxes for Starfire and TASKA (a mirror machine).

PRIMARY RECOIL ENERGY SPECTRA FOR THE (n,γ) REACTION

R. K. Smither and L. R. Greenwood (Argonne National Laboratory)

1.0 Objective

To develop methods to calculate the energy spectrum of primary recoils resulting from gamma ray emission following neutron capture.

2.0 Summary

A detailed analysis was made of the recoil energy spectrum from multiple γ-ray cascades following thermal neutron capture in iron. Explicit expressions are given for the primary recoil energy distributions expected from the emission of single gamma rays and double and triple cascades. The results are compared to our previous approximations where all gammas are assumed to be emitted independently. The new more complete analysis gives the same result for the average recoil energy per neutron capture as the simpler approximation that assumes that each gamma ray corresponds to an individual recoil event; however, the spectral shapes of the two approximations are quite different in some cases.

3.0 Program

Title: Dosimetry and Damage Analysis

Principal Investigator: L. R. Greenwood

Affiliation: Argonne National Laboratory

4.0 Relevant DAFS Program Plan Task/Subtasks

Task **II.B.l** Calculation of Defect Production **Cross** Sections.

5.0 Accomplishments and Status

Mathematical expressions are derived to generate the primary recoil spectrum for single, double, and triple gamma cascades assuming that **no** appreciable recoil momentum **is** imparted to the capturing nucleus by the captured neutron (thermal capture). The method of analysis **is** applied to two Fe nuclei, $^{56}Fe(n,\gamma)^{57}Fe$ and $^{57}Fe(n,\gamma)^{58}Fe$, and compared with the simpler **calculation** where each gamma ray produces a separate recoil event. A general expression **for** the average recoil energy per neutron capture event is derived that can be applied to gamma cascades with any number of sequential gamma rays.

5.1 Primary Recoil Energy Spectrum from the (n,γ) Reaction

When a gamma ray ***is*** emitted from a nucleus following thermal neutron capture the kinetic energy of the recoiling nucleus (neglecting E_n) **is** given by Eq. (1)

$$E_r = \frac{E_\gamma^2}{2mc^2} \tag{1}$$

where E_γ **is** the gamma ray energy and m is the mass of the nucleus. If two gamma rays are emitted before the nucleus **has** a chance to slow down then their momentum add vectorically. The recoil energy in this case is given by Eq. (2)

$$E_r = E_{\gamma 1}^2 + E_{\gamma 2}^2 + 2E_{\gamma 1}E_{\gamma 2}\cos\theta \tag{2}$$

where θ is the angle between the two y-rays. If the y-ray angular distribution is isotopic the resultant distribution of recoil energies is quite simple. The maximum recoil energy is given by Eq. (3)

$$E_r(max) = (E_{\gamma 1} + E_{\gamma 2})^2/2mc^2 \quad (3)$$

and the minimum recoil energy is given by Eq. (4)

$$E_r(min) = (E_{\gamma 1} - E_{\gamma 2})^2/2mc^2 \quad (4)$$

What is of special interest is that the number of recoils per unit energy between these limits is a constant (see Fig. 1b). The average value for E_r is given by Eq. (5)

$$\bar{E}_r(n) = (E_{\gamma 1}^2 + E_{\gamma 2}^2)/2mc^2 \quad (5)$$

This is just the sum of the recoil energies that would be produced if the gamma rays were considered as individual events. If the neutron capture event is followed by a 2-gamma ray cascade then the average recoil energy generated per neutron capture is given by (5). This is also the average recoil energy per recoil event if the lifetime of the intermediate state is shorter than the stopping time (time for recoiling atom to lose 63% of its recoil energy). If the lifetime is long compared to the stopping time then the two recoils are two separate events and the average recoil energy per event is one-half the value of the average recoil energy per neutron capture, given by Eq. *(5)*.

It is important to maintain the distinction between the average recoil energy per neutron capture, $\bar{E}_r(n)$, and the average recoil energy per recoil event, $\bar{E}_r(r.e.)$, because the latter can be much smaller than the former for (n,γ) events with a high multiplicity of gamma rays.

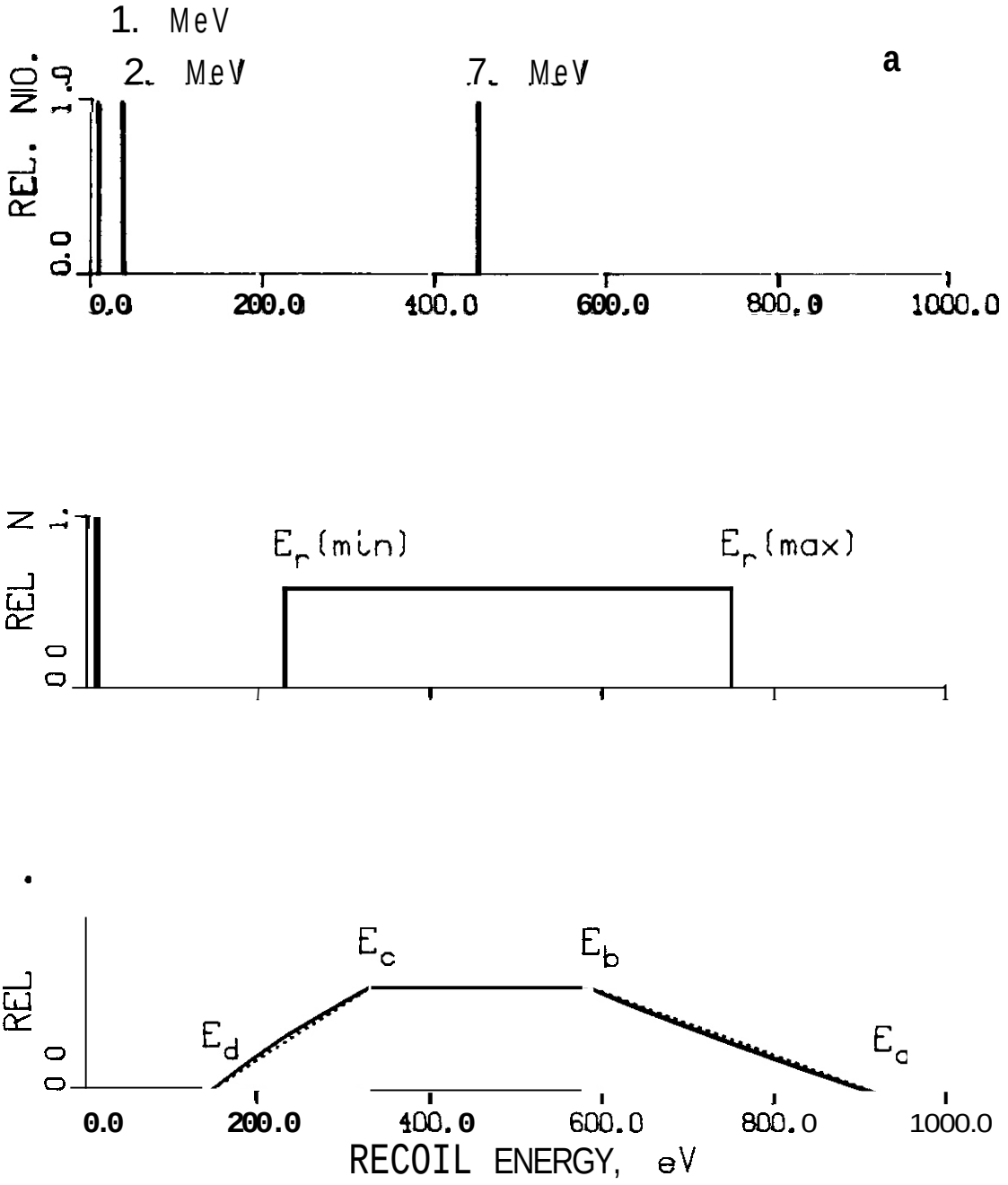

Fig. 1. (a) Recoil energy spectrum for three gamma rays (7 MeV, 2 MeV, and 1 MeV) considered as separate events in the $^{57}Fe(n,\gamma)^{58}Fe$ reaction. (b) The recoil energy spectrum for a two step cascade (E_γ = 7 MeV and 2 MeV) which has a rectangular shape followed by a one step cascade (E_γ = 1 MeV) which generated the spike at 9.3 ev. (c) The recoil energy spectrum of a three step cascade (E_γ = 7 MeV, 2 MeV, and 1 MeV) which results in a near trapezoidal shape distribution. $E_r(ev) = 9.255\ E_\gamma^2\ (MeV)^2$. The dashed lines indicate the trapezoidal approximation to the triple cascade case (c).

If the gamma cascade consists of three gamma rays and the lifetimes of the intermediate states are short then there is only one recoil event per neutron capture and the distribution of recoil energies has an almost trapezoidal shape as is seen in Fig. 1c. The upper limit of the recoil spectrum, E_a, can be very much more energetic then the recoil energy of any of the gamma rays when they are considered as individual events. The break points in the recoil energy distribution (Fig. 1c) E_a, E_b, E_c, and E_d are given by Eqs. (6)-(9), respectively:

$$E_a = (E_{\gamma 1} + E_{\gamma 2} + E_{\gamma 3})^2/2mc^2 \tag{6}$$

$$E_b = (E_{\gamma 1} + E_{\gamma 2} - E_{\gamma 3})^2/2mc^2 \tag{7}$$

$$E_c = (E_{\gamma 1} - E_{\gamma 2} + E_{\gamma 3})^2/2mc^2 \tag{8}$$

$$E_d = (E_{\gamma 1} - E_{\gamma 2} - E_{\gamma 3})^2/2mc^2 \tag{9}$$

where $E_{\gamma 1} \geq E_{\gamma 2} \geq E_{\gamma 3}$ and $E_{\gamma 1} \geq (E_{\gamma 2} + E_{\gamma 3})$. The actual shape of the curve (solid curve in Fig. 1c) is given by equation (10) between E_a and E_b

$$I(\text{rel.}) = \frac{(E_{\gamma 1} + E_{\gamma 2} + E_{\gamma 3}) - (E_r mc^2)^{1/2}}{8\, E_{\gamma 1} E_{\gamma 2} E_{\gamma 3}} \tag{10}$$

and by equation (11) between E_c and E_d.

$$I(\text{rel.}) = \frac{(E_r mc^2)^{1/2} - (E_{\gamma 1} - E_{\gamma 2} - E_{\gamma 3})}{8\, E_{\gamma 1} E_{\gamma 2} E_{\gamma 3}} \tag{11}$$

The value of I(rel.) is constant between E_b and E_c with a value given by Eq. (12)

$$I(\text{rel.}) = \frac{1}{4\, E_{\gamma 1} E_{\gamma 2}} \tag{12}$$

A somewhat more complicated shape develops when $E_{\gamma 1} \leq (E_{\gamma 2} + E_{\gamma 3})$ but a similar analysis is possible. In the triple cascade case, the average recoil energy per neutron capture is given by Eq. (13)

$$\bar{E}_r(n) = (E_{\gamma 1}^2 + E_{\gamma 2}^2 + E_{\gamma 3}^2)/2mc^2 \qquad (13)$$

The general form for $\bar{E}_r(n)$ for the case of "x" sequential gamma rays is given by Eq. (14)

$$\bar{E}_r(n) = (E_{\gamma 1}^2 + E_{\gamma 2}^2 + E_{\gamma 3}^2 + \ldots + E_{\gamma x}^2)/2mc^2 \qquad (14)$$

This is the same average energy that one would get if the lifetimes of the intermediate states were long and each gamma ray resulted in an independent recoil event. Thus the value of $\bar{E}_r(n)$ is not sensitive to the lifetimes of the intermediate states and is only a function of the energy distribution of the emitted gamma rays.

The energy distribution for $E_r(n)$ can be approximated by a trapezoid as discussed above with break points given by Eqs. (6), (7), (8), and (9), (see Fig. 1c). In most cases this is a quite good approximation and the value of $\bar{E}_r(n)$ calculated from this distribution agrees with this approximation to within a few percent for triple gamma cascades. The value of $\bar{E}_r(n)$ for the trapezoid approximation is given by Eq. (15)

$$\bar{E}_r(n)\ \text{trapezoid} = \frac{[(E_a - E_b)(E_a + 2E_b) + 3(E_b^2 - E_c^2) + (E_c - E_d)(2E_c - E_d)]}{3[(E_a + E_b) - (E_c + E_d)]} \qquad (15)$$

This agrees with Eq. (13) to within a few percent in most cases. Table I gives a comparison of the values of $\bar{E}_r(n)$ as calculated from Eq. (13) and Eq. (15) for the $^{57}Fe(n,\gamma)^{58}Fe$ case. The trapezoidal approximation is important because it is a much easier calculation to make for the spectral shape of the primary

Table I

Comparison of the Average Recoil Energy Per Neutron Capture Calculated With the Trapezoidal Approximation, Eq. (15) With the Exact Calculation Using Eq. (13) for a Number of Triple Cascades in the $^{57}Fe(n,\gamma)^{58}Fe$ Reaction.

$E_{\gamma 1}$ (mev)	$E_{\gamma 2}$ (mev)	EY3 (mev)	Trapezoid Approximation (ev)	$\Sigma(E_\gamma^2/2mc^2)$ (ev)	Ratio Trap./Σ()
10.0	0.0	0.0	925.5	925.5	1.000
9.8	0.1	0.1	889.2	889.0	1.000
9.0	0.5	0.5	755.9	754.3	1.002
8.0	1.0	1.0	617.0	610.8	1.010
7.0	2.0	1.0	506.0	499.8	1.012
6.0	2.0	2.0	431.3	402.2	1.061
6.0	3.0	1.0	431.9	425.7	1.015
5.0	2.5	2.5	385.7	347.1	1.111
5.0	3.0	2.0	376.4	351.7	1.070
4.0	3.0	3.0	339.7	314.7	1.079
4.0	4.0	2.0	337.9	333.2	1.014
3.33	3.33	3.33	311.6	308.4	1.010

recoil spectrum, and will be used below in the detailed calculations of the Fe cases.

The recoil spectrum of $^{57}Fe(n,\gamma)^{58}Fe$ reaction was calculated in detail taking into account all the known information about the level scheme, gamma decay pattern observed following neutron capture and the lifetimes of the low lying states.[1] Recoil energy spectra were calculated separately for the single gamma recoil events, the double gamma recoil events and the triple gamma recoil events, see Fig. 2a, 2b, and 3c, respectively. The sum of these three spectra is shown in Fig. 3a. It is quite different than the recoil energy spectrum that is calculated assuming that each gamma ray leads to a separate recoil event. This pure single spectrum is shown in Fig. 3b. The average $\bar{E}_r(n)$ was calculated for the recoil energy spectrum shown in Fig. 3a and compared to the value obtained from the observed (n,γ) spectrum using Eq. (14) as a check on the trapezoidal approximation. The two values 461ev and 456ev for the curve in Fig. 3a and Eq. (14), respectively, agree within 1%. A 40ev energy cutoff is used in both calculations.

Although the value of $\bar{E}_r(n)$ is the same for the two cases the spectral distribution of recoil energies is quite different (see Fig. 3a and 3b). This means that to the extent that displacement damage is a function of recoil energy the two spectra could lead to different amounts of displacement damage. In Fe the fraction of the recoil energy that ends up as displacement damage energy varies from 0.884 at E_r = 40ev to 0.817 at 930ev (Lindhard Model). This is not a large difference but it will have some effect. As an example

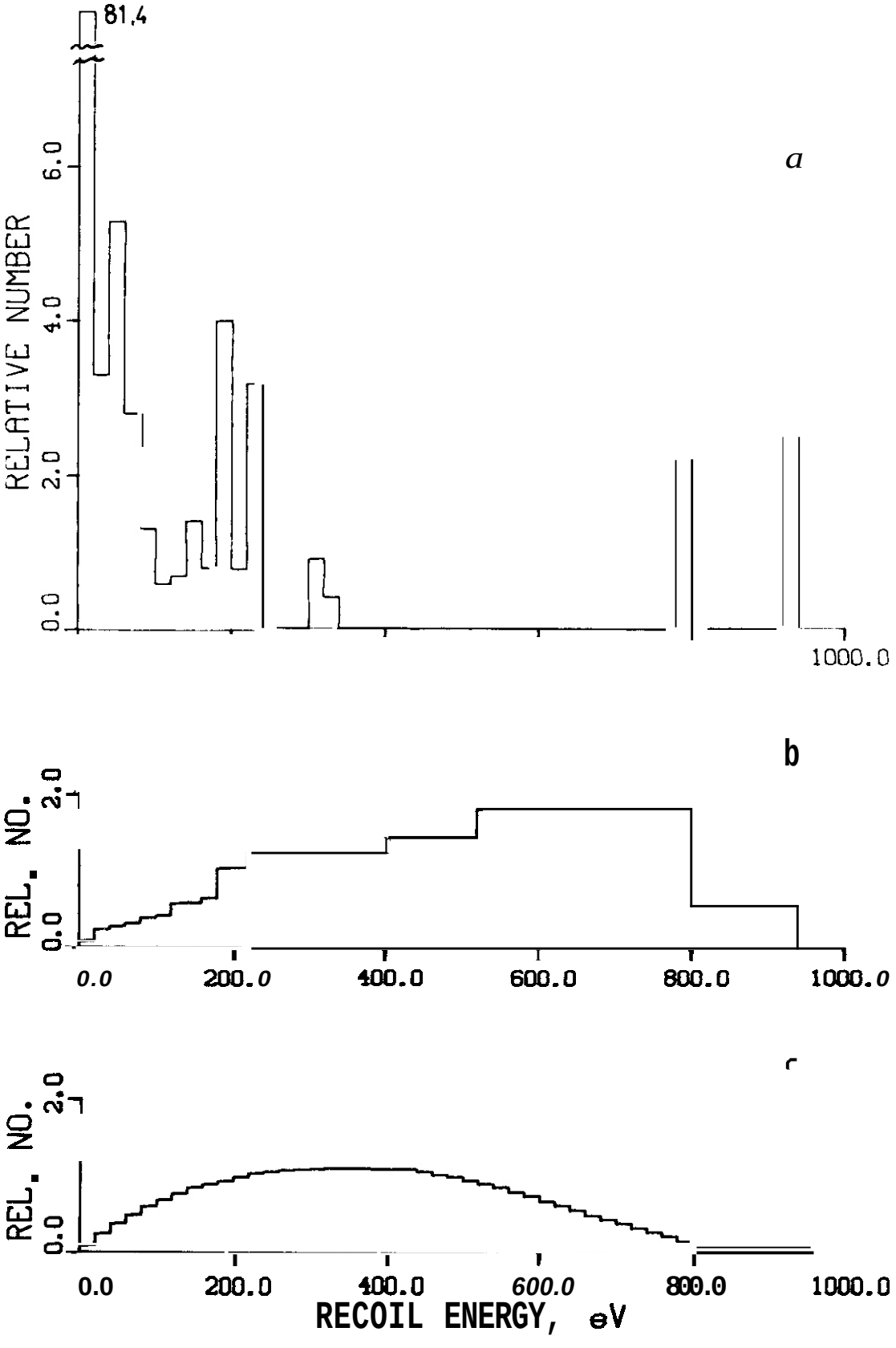

Fig. 2. Recoil energy spectra for $^{57}Fe(n,\gamma)^{58}Fe$ for cascade case where (a) is the spectrum for single gamma events, (b) two step cascades, and (c) three step cascades.

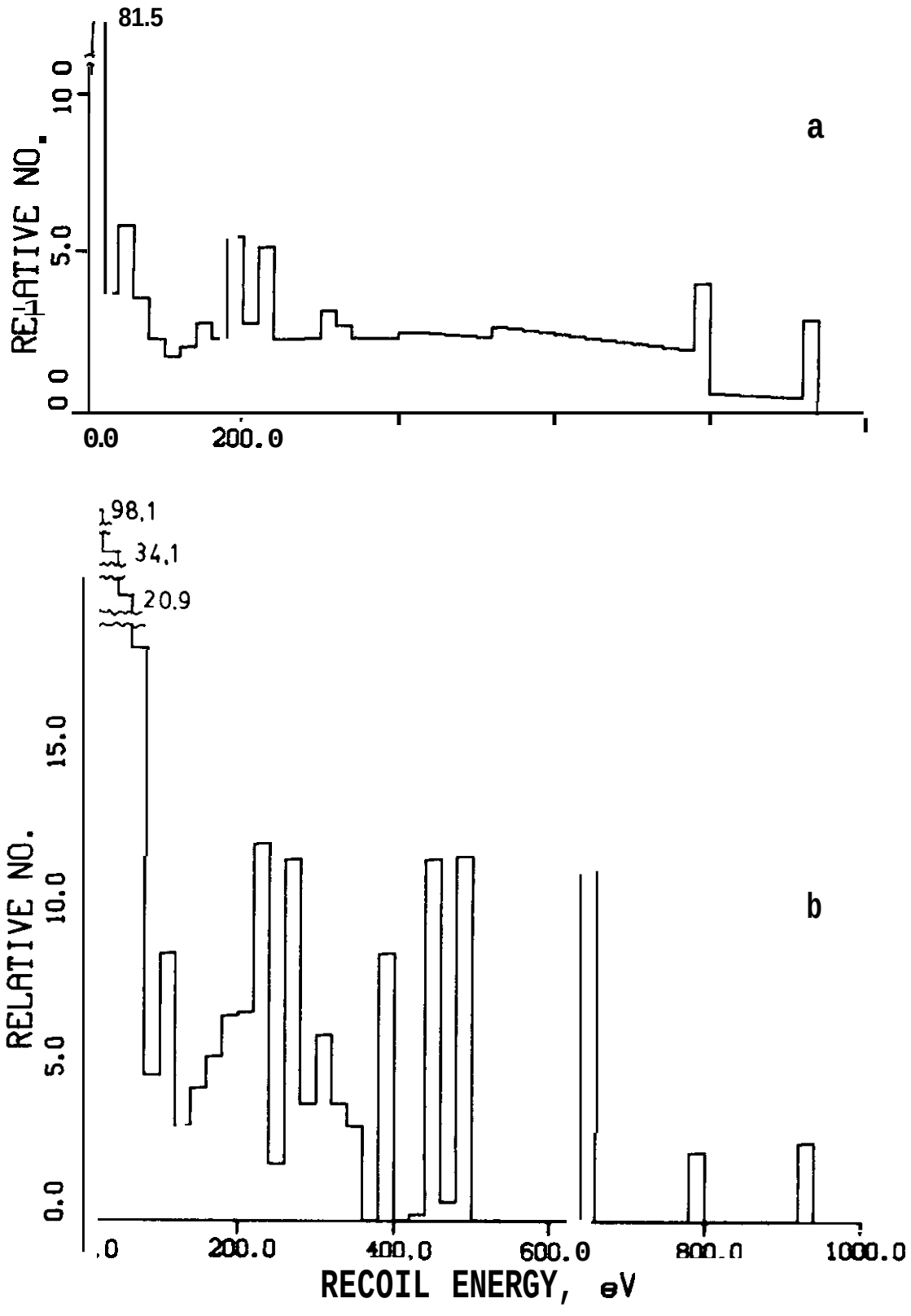

Fig. 3. Recoil energy spectra for the $^{57}Fe(n,\gamma)^{58}Fe$ reaction where (a) is the sum of calculated cascade spectra for the single events and the two step cascade and the three step cascades, shown in figure 2a, 2b, and 2c, respectively, and spectrum (b) is the recoil spectrum when all gamma rays are treated as individual recoil events.

of this effect one can calculate the average recoil energy per recoil event, $\bar{E}_r$(r.e.). This leads to $\bar{E}_r$(r.e.) = 416ev (with 40ev cutoff) for the multiple gama cascade case and $\bar{E}_r$(r.e.) = 272ev for the pure singles case (also with a 40ev cutoff on the recoil energy). The Lindhard function is 0.837 and 0.846 for the multiple cascade and singles cascade, respectively. In this case the difference is only about 1%. For lighter nuclei the difference will be larger. In Be the same recoil energies give a 2.4% effect.

The 40 ev cutoff on recoil energies is used to keep the large number of low energy recoils that are not strong enough to displace an atom from distorting these numbers. These spectra are typical of cases where the level scheme is complex, with high level densities and many decay paths.

A similar analysis made for the $^{56}Fe(n,\gamma)^{57}Fe$ reaction where the final level scheme ^{57}Fe has a level density that is much lower and where a few strong gamma ray transitions dominate the decay pattern. In this case the recoil energy spectrum does not change very much when the multiple gamma cascades are taken into account (see Fig. 4). There is some filling in between the strong recoil peaks but not much else happens. The $\bar{E}_r$, using trapezoidal approximation, is again quite similar for the two cases. The $\bar{E}_r$(n) is 412ev for the complex decay case and 409ev for the singles case using Eq. (11). The $\bar{E}_r$(r.e.), the recoil energy per recoil event, is again different in the two cases but not by a large factor. The $\bar{E}_r$(r.e.) for the complex case is 449ev as compared to 415ev for the all singles case. In both cases we have used a 40ev cutoff in recoil energy.

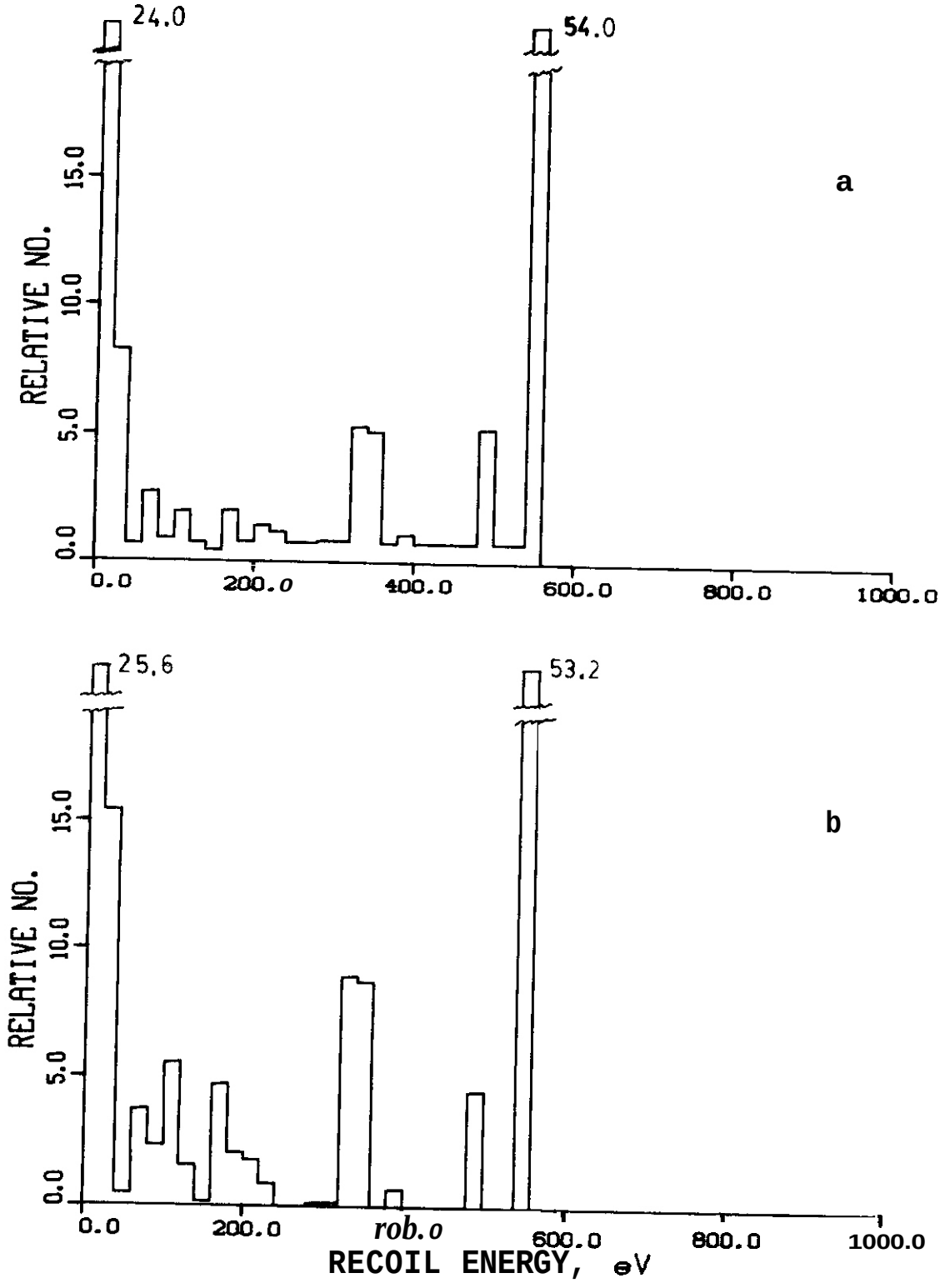

Fig. 4. Recoil energy spectra for the $^{56}Fe(n,\gamma)^{57}Fe$ reaction. (a) Calculated with cascades. (b) Calculated assuming that each gamma ray leads to a separate recoil event.

The above analysis has assumed that the gamma rays were emitted isotropically. The effect of an angular correlation between sequential γ-rays was examined and found to have only a small effect. This is because the γ-γ angular correlations contain only even Legendre polynomials. This means that they are symmetric with respect to $\theta = 90°$ and for every case where there is alignment of the two momentum vectors there is a corresponding case where the momentum vectors are in the opposite direction so the average value $\bar{E}_r$ remains unchanged. There is some effect on the recoil energy spectrum for an individual cascade but even this tends to wash out when the recoil energy spectra from many cascades are added together.

In summary, the approximation presently used in our damage calculations where the $\bar{E}_r(n)$ per neutron capture is calculated from the weighted average of the recoil energies assuming each gamma ray produces its own recoil event is the correct one to use even when the lifetimes of the intermediate states are short, and the multiple gamma cascades give only one recoil event per primary gamma ray. However, the calculation of the spectral shape of the recoil spectrum can be in considerable error unless the more complex analysis is used. The spectral shape of a two step cascade is a rectangle while a good approximation to the spectral shape of recoils from a triple cascade is a trapezoid, with break points given by Eqs. (6)-(9).

6.0 References

1. H. Schmidt, W. Michaelis, and U. Fanger, Nuc. Phys. A136 122 (1969).
2. U. Fanger, W. Michaelis, H. Schmidt, and H. Ottmar, Nuc. Phys. A128 641 (1969).

7.0 Future Work

Displacement damage energies and recoil spectra from the (n, γ) reaction will be generated for many elements of interest to the fusion program. Similar calculations will also be performed for beta decay displacement damage. Displacment cross sections for 36 elements have recently been sent to Lawrence Livermore Laboratory for inclusion in the NMFE computer system. A new computer code SPECTPV has been included to process the new data from ENDF/B-V. Users need only supply a neutron spectrum. The code then computes spectral-averaged displacements, PKA distributions, and gas production rates.

8.0 Publications

1. A paper entitled, "Neutron Source Characterization and Radiation Damage Calculations for Materials Studies", was presented at the "International Conference on Neutron Irradiation Effects" at Argonne National Laboratory on November 9-12, 1981. The paper will be published in the Journal of Nuclear Materials.

2. A paper entitled "Displacement Damage Calculations Using ENDF/B-V Cross Sections Including Thermal Neutron Capture and Beta Decay Effects", was presented at the Fourth ASTM-Euratom symposium on Reactor Dosimetry", March 22-26, 1982, National Bureau of Standards, Gaithersburg, MD. This paper will be published as part of the proceedings of this meeting.

ON THE USE OF THRESHOLDS IN DAMAGE ENERGY CALCULATIONS

Mark T. Robinson and Ordean S. Oen (Oak Ridge National Laboratory)

1.0 Objective

The purpose of this study is to construct atomistic numerical models of the development of collision cascades in solids and to apply them to studies of radiation damage production, sputtering, and plasma particle backscattering, in the context of fusion first wall materials development.

2.0 Summary

It is pointed out that there is an inconsistency in the use of a displacement threshold with the damage energy model that is part of the standard procedure for expressing radiation effects exposures. A simple correction to the model is presented and its consequences are discussed briefly.

3.0 Program

Title: Damage Analysis and Dosimetry
Principal Investigator: M. T. Robinson
Affiliation: Oak Ridge National Laboratory

4.0 Relevant DAFS and PMI Program Plan Task/Subtask

Subtask II.R. 2.3 Cascade Production Methodology

5.0 Accomplishements and Status

Studies of the effects of irradiation on the properties of materials require a method of estimating exposures which allows the comparison of observations made in a variety of different radiation environments. A widely used standard procedure has been developed for this purpose [1-3]. This is based in part on an analysis by Lindhard, et al. [4], of the energy loss processes involved in atomic slowinq down and in part on a modification of the simple collision cascade theory originated hy Kinchin and Pease [5]. It is the purpose of this communication to point out an inconsistency between the two parts of the model, to present an approximate correction of it, and to discuss its consequences briefly. Fortunately, the correction required is of such a character as to entail no major chanqes in current practice.

As energetic recoil atoms slow down in solids, they expend part of their kinetic energy in exciting electrons and only the remainder, the so-called damage energy [6], is available for producing defects by atomic displacement. Lindhard, et al. [4], calculated the partition of the initial kinetic energy of the primary displaced atom in a monatomic medium into these two forms, as all the knocked-on atoms in the cascade slow down to rest. Their results may be represented by

$$\hat{E}(E) = E\,[1 + k_L\, g(E/E_L)]^{-1} \quad , \tag{1}$$

where E is the initial kinetic energy of the primary recoil and $\hat{E}$ is the resulting average damage energy. The parameters are

$$k_L = (32/3\pi)\; 2^{3/4}\; (m/M)^{1/2}\; Z^{2/3}$$

$$= [0.133743\ \text{amu}^{1/2}]\; Z2/3/M1/2 \quad , \tag{2}$$

$$E_L = 2Z^2\, e^2/a_{12} = [86.93\ \text{eV}]\; Z^{7/3} \quad , \tag{3}$$

$$a_{12} = (9\pi^2/128)^{1/3}\, a_0 /2^{1/2}\, Z^{1/3}$$

$$= [33.13\ \text{pm}]\ Z^{-1/3} \qquad (4)$$

Here, Z and M are the atomic number and mass of the particles of the medium, e and m are the charge and mass of the electron, and a_0 is the radius of the first Bohr orbit of hydrogen (52.9 pm). The remaining function in Eq. (1) is [6,7]

$$g(\varepsilon) = \varepsilon\ t\ 0.40244\ \varepsilon^{3/4}\ t\ 3.4008\ \varepsilon^{1/6} \qquad (5)$$

It is important to emphasize that the slowing down model embodied in Eqs. (1-5) considers only the average behavior of cascades. Furthermore, the initial energy of the primary recoil is assumed to be completely dissipated: there is no displacement threshold energy involved.

The simple cascade theory oriqinated by Kinchin and Pease [5] and extended later by others [8,9] considers that there is a sharp displacement threshold energy E_d. If a lattice atom originally at rest receives a kinetic energy $E < E_d$, it may move away from its oriqinal lattice site briefly, but is constrained to return to it eventually by restorinq forces in the crystal. If the atom receives an energy $E > E_d$, in contrast, it will not be able to return to its oriqinal location, but will remain permanently displaced. In addition, however, it is recognized that if a recoilinq atom with energy $E_d < E < 2\ E_d$ displaces another, there is no net increase in the number of movinq particles, since the final energy of the projectile will be $< E_d$ and it will Simply replace the target atom on its lattice site. Thus, in the absence of energy losses by electron excitation, the Kinchin-Pease model predicts that the average numher of displaced atoms in a cascade will be approximately [8,10]

$$\nu(E) = \begin{cases} 0 & 0 < E < E_d \\ 1 & E_d < E < 2E_d/\kappa \\ \kappa E/2E_d & 2E_d/\kappa < E < \infty \end{cases} . \qquad (6)$$

The parameter κ allows for the nature of the atomic stopping cross section. Both analytical theory [9] and computer simulations [11] suggest a value near 0.8. Equation (6) is approximate in that κ actually varies with energy [8,12], decreasing from unity at $2E_d$ to the asymptotic value used in Eq. (6).

The standard procedure for estimating the number of displacements in an irradiation [1-3] unites the two models outlined above by replacing E, wherever it occurs in Eq. (6), by $\hat{E}$, as evaluated from Eqs. (1-5). It should he noted that $\hat{E}$, not E, then appears in the limits of Eq. (6), a point not always noticed (*see* [3,13], for example). But this scheme involves an inconsistency: a part of the inelastic energy losses discounted in Eq. (1) occurs only after the recoiling atoms have slowed down below

$$L = 2E_d/\kappa , \qquad (7)$$

and cannot, therefore, influence the number of defects produced according to Eq. (6). While electron excitations are relatively less important at low recoil energies than at high, Eq. (1) nevertheless predicts significant inelastic losses at energies below L. For instance, 16.5% of the energy of an aluminum atom of 54 eV kinetic energy is reckoned by Eqs. (1-5) to he lost inelastically. Such an amount appears to require a significant correction to current standard procedures.

The correction to the standard model for inelastic energy losses occurring below the energy L may be estimated in the following simple manner. Let $\hat{E}_1$ he the corrected mean damage energy. Then, the average number of displaced atoms is $\hat{E}_1/L$, as long as $\hat{E}_1 > L$. As these particles slow down to rest from L, each of them experiences an inelastic energy loss $L - \hat{E}(L)$; since

this loss cannot influence the final number of displacements, it must be added back into the damage energy. Hence,

$$\hat{E}_1(E) = \hat{E}(E) + [\hat{E}_1(E)/L]\,[L - \hat{E}(L)] ,$$

which may be solved to yield

$$\hat{E}_1(E) = [L/\hat{E}(L)]\,\hat{E}(E) \qquad L < E < \infty , \tag{8}$$

which is to be used in Eq. (6) instead of Eq. (1).

There are several interesting points to be made about Eq. (8). First, the correction factor is a constant, independent of the primary recoil energy. Thus, as long as the primary recoil spectrum is not dominated by particles having $E_d < E < L$, the spectrum-averaged damage energy (or, equivalently, the damage energy cross section) is multiplied by the same factor. Furthermore, if the objective is to compare different radiation environments with respect to their abilities to produce radiation effects, since the same correction factor is used for all, precisely the same prediction is made as in the current standard procedure.

Second, as the kinetic energy of a recoil approaches L, the modified mean damage energy $\hat{E}_1(E)$ approaches L also, unlike $\hat{E}(E)$ which approaches the lesser value $\hat{E}(L)$. Thus, in treatments using the modified quantity, it is no longer necessary to use the damage energy in definitions of the segment limits as was the case before.

Another way of looking at Eq. (8) is to note that it is equivalent to correcting the threshold energy L for inelastic losses. That is, the number of defects is to be evaluated using not L, but $\hat{E}(L)$ instead, in conjunction with the original damage energy, Eq. (1). In this formulation also, the kinetic energy appears in the expressions for the limits.

Finally, the approximate nature of the correction procedure must be noted. If a threshold were actually introduced into the integrodifferential equation solved by Lindhard, et al. [4], it would be necessary to alter the boundary conditions and there is little doubt that the form *of* the solution would be altered as well, especially in the vicinity of the threshold energy.

To complete the correction of Eq. (1) for threshold effects, it is necessary to include in the model particles with initial enerqies below L. This is done by adding to Eq. (8) the following

$$\hat{E}_1(E) = \begin{cases} 0 & 0 < E < E_d \\ L & E_d < E < L \end{cases} \qquad (9)$$

Finally, if spectral averaging is required, the revised model yields

$$\langle n\, \hat{E}_1 \rangle = L\{ \int_{E_d}^{L} n(T)\, dT + [\hat{E}(L)]^{-1} \int_{L}^{\infty} n(T)\, \hat{E}(T)\, dT \}\ , \qquad (10)$$

which is to be compared to the conventional result

$$\langle n\, \hat{E} \rangle = \int_{0}^{\infty} n(T)\, \hat{E}(T)\, dT\ .$$

In both cases, n(T) is either a normalized primary recoil energy spectrum, a primary recoil production cross section, or some similar weightinq function.

Although the corrected damage energy model has been discussed here in terms of a displacement model of the Kinchin-Pease type [5], it is as easily applied to displacement models *of* the Snyder-Neufeld type [14] in which a displaced atom must overcome an energy barrier before movinq away from its lattice site. An atom receiving energy E in a collision, commences to move

with kinetic energy $E - E_d$. Models of this type are included in the above framework by redefininq L: it is only necessary to replace the factor 2 in Eq. (7) by 3 [12].

The corrected damage energy model of Eqs. (8,9) is easily included in computations. To illustrate this, the well-known machine proqram E-DEP-1 [15] was modified to include the corrections. Followinq Doran and Kulcinski [16], the program already evaluated the second inteqral of Eq. (10), so that it was only required to include the correction factor deduced in Eq. (8) above and the first inteqral in Eq. (10). The effects of the changes in the model are illustrated in Fiq. 1, which shows the total damage energy deposited in aluminum by 4.8 MeV Al ions as a function of the values of L and of E_d. The curves show, respectively, the second integral of Eq. (10) without the correction, the same inteqral with the

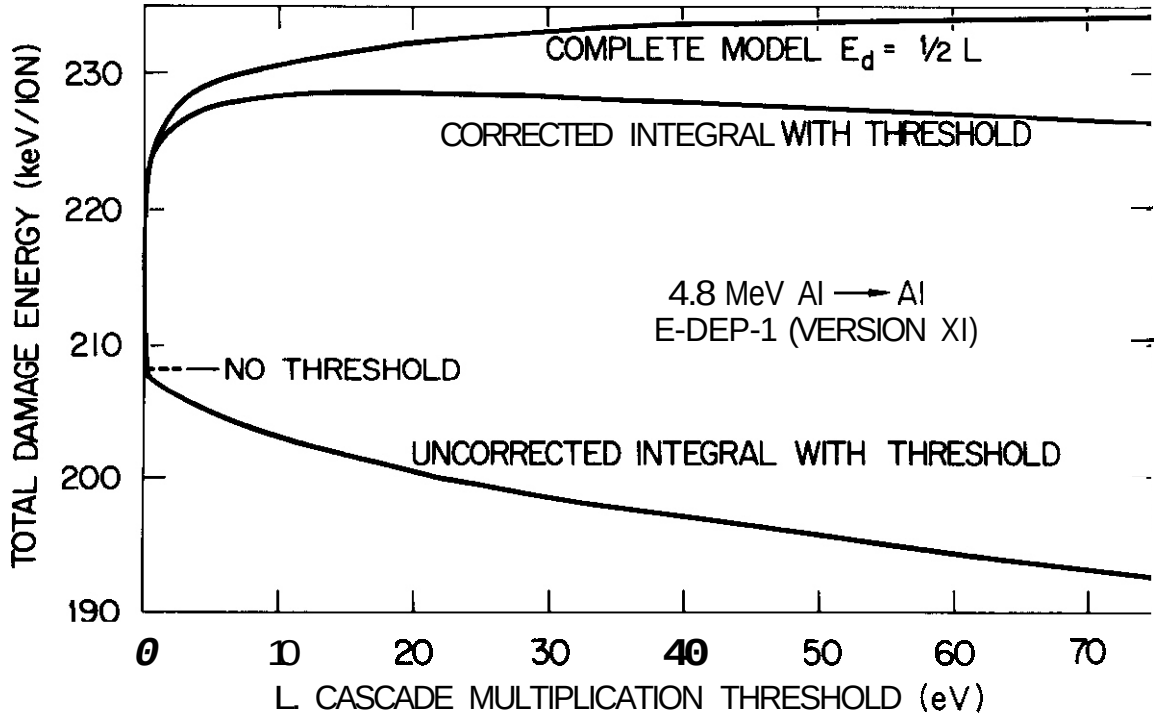

Fig. 1. The influence of a threshold energy on the damaqe energy is shown as calculated with the code E-DEP-1 [14] for 4.8-MeV Al ions incident on Al. The three curves are explained in the text.

correction, and the result of the complete model with E_d = L/2. The rapid rise in the corrected mean damaqe enerqies for very small thresholds reflects the very weak $\varepsilon^{1/6}$ dependence of Eq. (5). Both corrected curves show quite the opposite dependence on L that is displayed by the uncorrected curve. Furthermore, away from the small threshold region, both corrected curves are much less sensitive to the threshold value than is the uncorrected curve.

Although the corrected damaqe enerqy will often lead to exposure correlations which are essentially the same as those based on the uncorrected quantity, this will not always he the case. It may be expected that the corrections will be particularly significant in those situations where the target recoil energy spectrum is dominated by low enerqy particles. Irradiations by light ions provide the most important of these situations. Here, where many tarqet recoils will be produced with intial enerqies between E_d and L, the corrections outlined here may prove to be essential.

5.1 Acknowledgements

It is a pleasure to acknowledqe many stimulatinq discussions of this topic with T. S. Noqgle.

6.0 References

[1] M. J. Norqett, M. T. Robinson, and I. M. Torrens, Nucl. Engin. Design 33 (1975) 50.

[2] D. G. Doran, J. R. Beeler, Jr., N. D. Dudey, and M. J. Fluss, "Report of the working group on displacement models and procedures for damage calculations", U.S.A.E.C. Report HEDL-TME 73-76 (December 1973).

[3] "Standard Recommended Practice for Neutron Radiation Damaqe Simulation by Charged-Particle Irradiation", ANSI/ASTM E 521-77, pp. *983-1001* (1977).

[4] J. Lindhard, V. Nielsen, M. Scharff, and P. V. Thomsen, Kql. Dan. Vidensk. Selsk. Mat.-fys. Medd. 33 (1963) no. 10.

[5] G. H. Kinchin and R. S. Pease, Rep. Progr. Phys. 18 (1955) 1.

[6] M. T. Robinson in Nuclear Fusion Reactors (British Nuclear Energy Society, London, 1970), p. 364.

[7] Equation (9) of Reference 3 omits the linear term in Eq. (5) of the present text.

[8] M. T. Robinson, Phil. Mag. 12 (1965) 741.

[9] P. Sigmund, Radiat. Eff. 1 (1969) 15.

[10] Equation (17) of reference 3 incorrectly omits the factor κ which appears in Eqs. (6, 7) of the present text and uses E instead of $\hat{E}$ in the expressions for the limits.

[11] M. T. Robinson and I. M. Torrens, Phys. Rev. B 9 (1974) 5008.

[12] M. T. Robinson in Radiation-Induced Voids in Metals, edited by J. W. Corbett and L. C. Ianiello (U.S.A.E.C., CONF-710601, 1972), p. 397.

[13] R. S. Averback, R. Benedek, and K. L. Merkle, Phys. Rev. B 18 (1978) 4156.

[14] W. S. Snyder and J. Neufeld, Phys. Rev. 97 (1955) 1636.

[15] I. Manning and G. P. Mueller, Computer Phys. Comm. 1 (1974) 85.

[16] D. G. Doran and G. L. Kulcinski, Radiat. Eff. 9 (1971) 284.

CHANNELING IN HIGH ENERGY DISPLACEMENT CASCADES

H. L. Heinisch (Hanford Engineering Development Laboratory)

1.0 Objective

The objective of this work is to develop computer models for the simulation of high energy cascades which will be used to generate defect production functions for correlation analysis of radiation effects.

2.0 Summary

High energy cascades generated with the MARLOWE code were analyzed using computer graphics to determine how frequently channeling events occur. The effects of channeling on cascade configurations were determined in part by comparing cascades produced in crystalline and amorphous media. Channeling events do occur frequently in high energy cascades, but they have little effect on the overall size and shape of the cascades.

3.0 Program

Title: Irradiation Effects Analysis (AKJ)
Principal Investigator: D. G. Doran
Affiliation: Hanford Engineering Development Laboratory

4.0 Relevant DAFS Program Plan Task/Subtask

Subtask II.B.2.3 Cascade Production Methodology

5.0 Accomplishments and Status

5.1 Introduction

Somewhere in the energy range of 10-50 keV for most metals, displacement cascades undergo a transition from having essentially a single damage area to having

multiple, widely spaced damage regions, known commonly as subcascades. The existence of subcascades is experimentally inferred from transmission electron microscope observations; at very low doses they appear as a collection of damage regions spaced much more closely than the average spacing of primary events,[1] or at higher doses, they are manifested as a higher density of damage regions than the density of primary events.[2] Dramatic evidence for the subcascade phenomenon can be seen in images of disordered regions produced by irradiation in ordered alloys.[3] These disordered regions also bear a remarkable resemblance to the configurations of defects produced in displacement cascades generated with the computer code MARLOWE.[4]

The production of subcascades is, in general, a manifestation of the increase in the mean free path between energetic collisions with increasing energy of the projectile atom. Another phenomenon which may have an influence on the configuration of cascades is channeling. This phenomenon has been observed in computer simulations of cascades, but attempts at experimental observations of it have been generally negative or inconclusive (for example, Reference 3). It occurs when an energetic primary or secondary knock-on atom is given a trajectory between two atomic planes such that relatively low energy collisions tend to confine the trajectory to that plane over a fairly large distance, with a loss of only a small portion of the projectile's energy. Thus, upon de-channeling, the projectile can produce a damage region widely separated from the rest of the cascade.

The question arises, then, as to how important the channeling phenomenon is to the production of subcascades, especially in higher energy cascades where opportunities for channeling events are more numerous. Computer simulations indicate that channeling occurs, though rarely, in cascades of 30 keV or less. In these lower energy cascades, the appearance of channeling is rather dramatic, since normally only a single, fairly compact damage region is produced. In cascades with 100's of keV of energy, damage is produced in subcascades which may or may not be the result of channeling events.

5.2 Computations and Results

Cascades of 200 and 500 keV in Cu, produced with MARLOWE (thermal displacements not included), were analyzed to detenine the contribution of channeling to the cascade configuration. The actual trajectories of energetic projectiles could not be determined, but the apparent trajectories could often be inferred from "debris" (an occasional Frenkel pair) along their paths (Figure 1) or from the relative shape and position of the damage regions (Figure 2). The directions of the trajectories were determined for events between separated damage regions, and classified as being channeling or non-channeling directions.

The measurements were performed using interactive three-dimensional computer graphics. The cascades were rotated until the observer was looking directly along the direction of the trajectory, then the angles of rotation were recorded This technique was judged to produce results with an uncertainty of at least $\pm 2°$. While the measurement techniques could be refined, there is still a good deal of subjectivity involved in inferring the precise trajectory from debris along the path.

The trajectory directions for 74 events in 40 cascades were reduced to the fundamental triangle for the fcc lattice. Directions in the channeling planes (100), (110), (111) lie along the border of the fundamental triangle and on the line from <110> to <211>. Of the events measured, 68% have directions within 2° of a channeling direction. If directions were chosen at random, about 41% of all directions would be in this category. Thus, it seems that channeling events occur frequently in high energy cascades, but they are not the exclusive mechanism by which widely separated damage regions are produced.

How channeling events influence the configurations of high energy cascades was investigated by comparing high energy cascades produced in crystalline and amorphous copper. The MARLOWE code models an amorphous material by performing a random rotation of the lattice after each collision. While this procedure does not rigorously represent the amorphous condition, nevertheless the symmetry which allows channeling is destroyed. Samples of twenty crystalline and amorphous 200 keV cascades were compared.

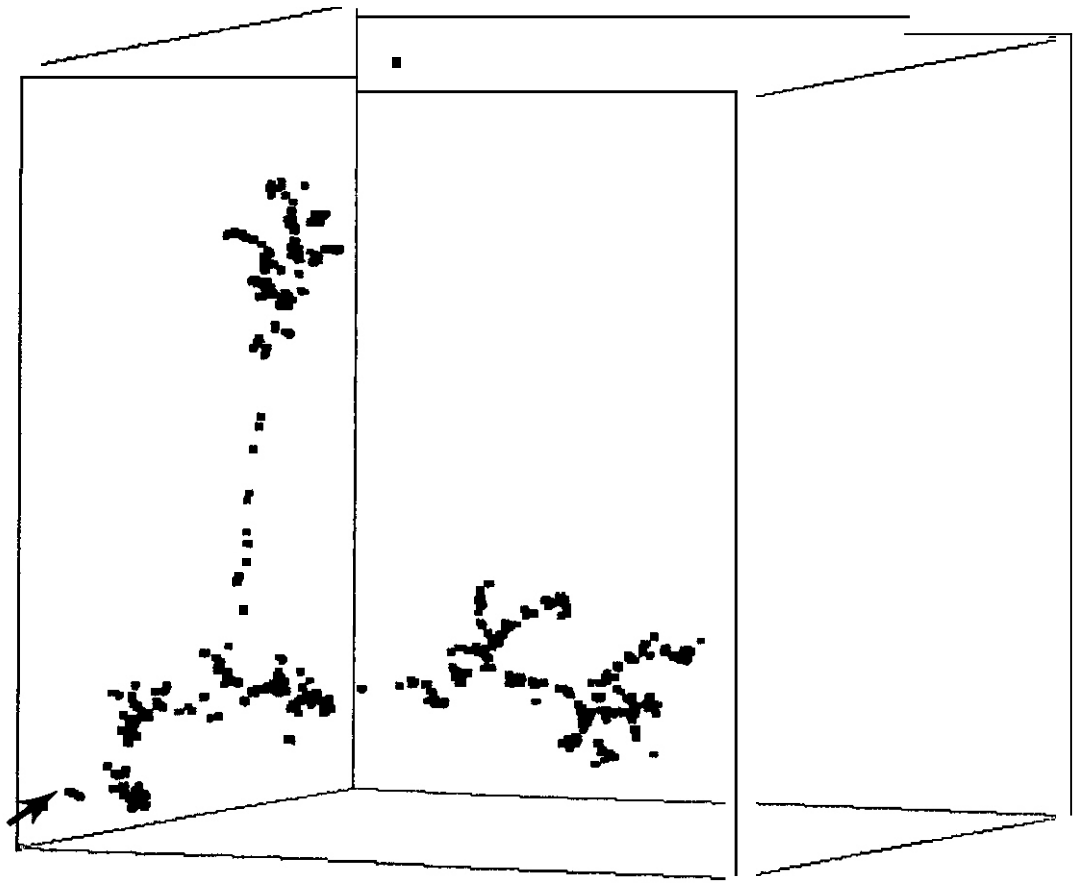

FIGURE 1. 200-keV Cascade in Copper, Vacancies Only, After Recombination. Cube edge is 170 lattice parameters.

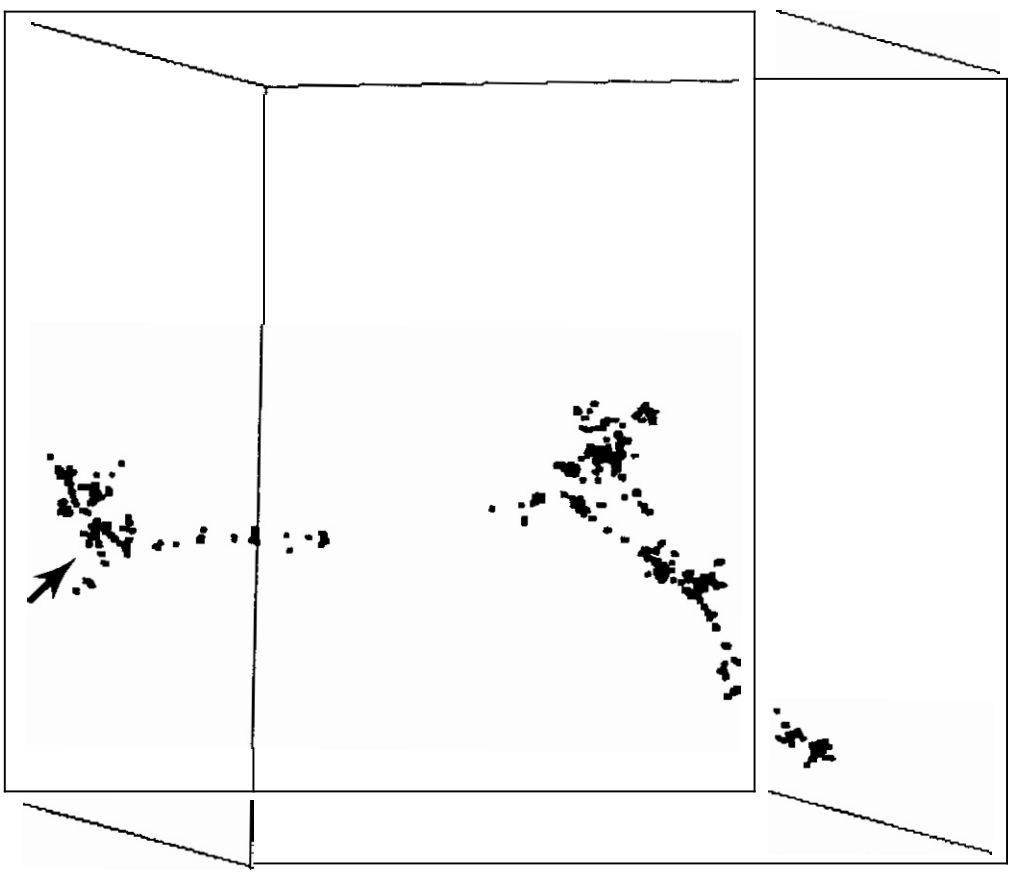

FIGURE 2. 200-keV Cascade in Copper, Vacancies Only, After Recombination. Cube edge is 211 lattice parameters.

The vacancy distributions were compared after some recombination to simulate quenching of the cascade. The maximum extent along the initial recoil direction, as well as the aspect ratio, i.e., the ratio of the maximum length to the average maximum width of a cascade, were measured for each vacancy distribution. The safest conclusion on the basis of the small sample size is that the differences are slight, although the crystalline cascades have slightly larger average values of both maximum extent and aspect ratio.

Figure 3 shows one of the amorphous cascades. It is virtually indistinguishable in its general nature from the crystalline cascades (Figures 1 and 2). However, an inspection of all cascades in both sets allows one to distinguish a difference in character between the amorphous and crystalline cases. In the crystalline case there is a tendency for more clearly separated damage regions, the result of channeling events.

5.3 Conclusions

Channeling events do occur frequently in high energy cascades. Their lengths are seldom much larger than the average dimensions of cascades in which channeling does not occur. Hence, channeling does not appear to be an important phenomenon with respect to cascade sizes at high energies. Channeling may be important in that it produces somewhat more clearly separated damage regions. Thus, if channeling is suppressed, the behavior of the defects subsequent to the collisional phase of the cascade (recombination, clustering, etc.) may be influenced. This could be tested by comparing the crystalline and amorphous cascades after short-term annealing.

As to why channeling in high energy cascades has not been experimentally confirmed, the following observations are pertinent: not all separated damage regions in a cascade are a result of channeling. There tend to be few extraordinarily long channeling events. A minimum size is required for damage regions to be visible in a TEM, and a channeling event does not always lie along a line connecting two major (hence visible) damage regions.

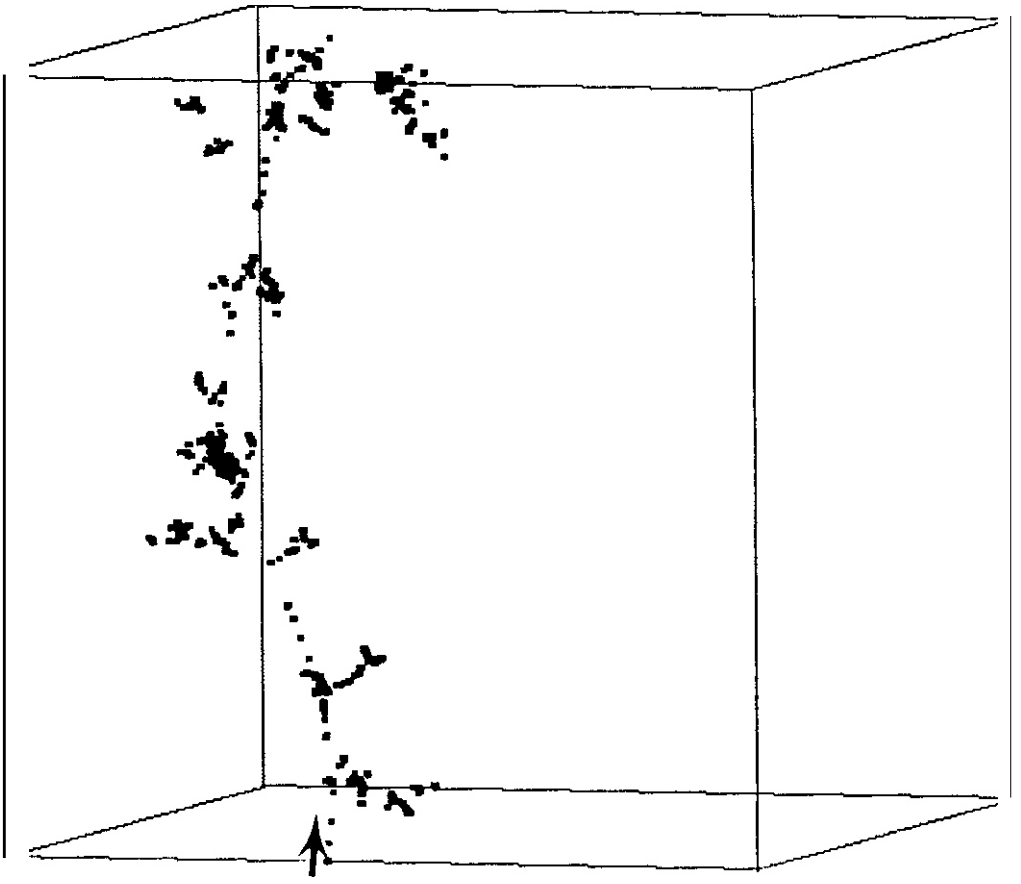

FIGURE 3. 200-keV Cascades in Amorphous Copper, Vacancies Only, After Recombination. Cube edge is 192 lattice parameters.

6.0 References

1. K. L. Merkle, L. R. Singer and R. K. Hart, J. Appl. Phys., 34 (1963) 2800.
2. R. V. Hesketh and G. K. Richards, Proc. Roy. Soc. A, 289 (1966) 353.
3. M. L. Jenkins, N. G. Norton and C. A. English, Phil. Mag. A, 40 (1979) 131.
4. H. L. Heinisch, Phil. Mag. A, in press.

7.0 Future Work

Future work will be concerned with short-term annealing of high energy cascades and determination of defect production functions (see the other contribution in this report).

CASCADE QUENCHING AND SHORT-TERM ANNEALING

H. L. Heinisch (Hanford Engineering Development Laboratory)

1.0 Objective

The objective of this work is to develop computer models for the simulation of high energy cascades which will be used to generate defect production functions for correlation analysis of radiation effects.

2.0 Summary

Defect production in high energy displacement cascades has been modeled using the computer code MARLOWE to generate the cascades and the stochastic computer code ALSOME to simulate the cascade quenching and short-term annealing of isolated cascades. The quenching is accomplished by using ALSOME with exaggerated values for defect mobilities and critical reaction distances for recombination and clustering, which are in effect until the number of defect pairs is equal to the value determined from resistivity experiments at 4K. Then normal mobilities and reaction distances are used during short-term annealing to a point representative of Stage III recovery. The number of free interstitials after short-term annealing is fairly insensitive to the quench model, but the number of free vacancies depends strongly on the clustering criteria used during the quench. Preliminary results for 30-keV copper cascades are in good agreement with some experimental results.

3.0 Program

Title: Irradiation Effects Analysis (AKJ)
Principal Investigator: D. G. Doran
Affiliation: Hanford Engineering Development Laboratory

4.0 Relevant DAFS Program Plan Task/Subtask

Subtask 11.6.2.3 Cascade Production Methodology

5.0 Accomplishments and Status

5.1 Introduction

Earlier simulations [1] of short-term annealing of displacement cascades were done with the stochastic cascade annealing simulation code SCAS, operating on cascades generated with the MARLOWE [2] code. MARLOWE models only the collisional phase of cascade development, which occurs in about 10^{-13} sec. In the previous work, to account for the recombination which occurs as the energetic cascade region quickly comes to thermal equilibrium with the remainder of the crystal (cascade quenching), the closest defect pairs in the MARLOWE cascades were recombined until the "experimental value" of defects remaining at 4K was reached.[1] The cascades were then short-term annealed with the code SCAS. The results of this procedure were annealed cascades which contained many more freely migrating defects, both vacancy and interstitial, than has been inferred from experimental measurements.[3-5]

The least physical part of those earlier cascade simulations is undoubtedly the simulation of quenching by simple static recombination in a highly energetic cascade. Cascade quenching can only be properly simulated by fully dynamical cascade models. However, for cascade energies high enough to be of interest, such an approach may not presently be computationally feasible. And, even if feasible, the dynamical simulations are not practical for generating statistically significant numbers of high energy cascades. Therefore, some simplified parametric model of cascade quenching must be developed to bridge the gap between MARLOWE and short-term annealing in a physically reasonable way.

So far, this parametric model has consisted of the simple recombination of pairs in a static, MARLOWE-generated cascade. As a first step toward a more realistic quench model, a kinetic recombination model using the short-term annealing code has been devised. The annealing code has been modified to preprocess the cascades with quenching values for the parameters, and then to anneal them with normal parameter values. The annealing simulation code, now known as ALSOME, is an expanded version of the SCAS code. It has many more features, but retains the original algorithm.

In ALSOME a mobile defect is chosen at random, based on its relative jump frequency, and its position is changed by one lattice parameter in a randomly chosen direction. Its environment is then searched for possible interactions with other defects, based on critical reaction distances for various types of interactions (e.g., clustering or recombination). The interactions, if any, are performed, and another defect is randomly chosen, etc. The quenching scheme in ALSOME utilizes this same jumping and reacting algorithm, however, the values of the jump and reaction parameters are set to produce defect behavior more representative of that occuring during the quench. In particular, the mobile defect species (single, di-, tri- and tetra- vacancies, single, di- and tri- interstitials) are considered to be equally mobile during the quench, and critical reaction distances are exaggerated.

There are essentially four adjustable parameters presently in this quenching scheme: the recombination, interstitial clustering, vacancy clustering, and the time duration of the quench. According to arguments based on thermal conduction,[6] a localized cascade region with a well-defined temperature much higher than its surroundings exists on the order of 10^{-11} sec. Time is measured in ALSOME in terms of the number of jumps of a single interstitial. The quench time was fixed at 100 jumps, consistent with the 10^{-11} sec. time frame. Sensitivity studies were then performed on the interstitial and vacancy clustering and recombination parameters.

5.2 Results

The average behavior of ten 30-keV cascades in Cu was determined as a function of quenching parameter values. The cascades are treated as isolated cascades, and a volume is prescribed about each cascade such that once a defect exits this volume it does not return. Short-term annealing simulations terminate when no mobile defects remain within this volume. The annealing occurs in two distinct phases: first the migration of interstitial defects which are orders of magnitude more mobile than vacancies, then the migration of the mobile vacancy defects which remain. Throughout the annealing, ALSOME reports on the total number of Frenkel pairs and the numbers and types of mobile and stationary

defect clusters. In particular, the state of the system is noted at the end of the quench, after interstitial migration, and at the termination of short-term annealing.

This is a semi-empirical approach to modeling defect behavior, thus quenching parameter values will be chosen so the results produce the best match to available experimental information. Specifically, the number of defect pairs remaining after the quench should be equal to the value extracted from resistivity data on low temperature irradiated Cu. (The recombination occuring during the quenching phase should be only slightly affected by the lattice temperature, hence the resistivity measurements for cascades produced at low temperatures where defects are immobile should give a reasonable value for the number of pairs remaining after the quench.)

The numbers of freely migrating interstitial and vacancy defects (i.e., those not clustering or recombining within their own cascade) have been inferred from experiments.[3-5] In the simulation these are the defects which escape the cascade region during short-term annealing. For fission neutron irradiated Cu about 15% of the initial interstitials (at ~170K) are free,[3] while about 4% of vacancies in fission neutron irradiated Cu_3Au [4] (at ~470K) are free.

The amount of recombination during the quench is most strongly influenced by the value of the recombination radius. Clustering tends to diminish the amount of recombination during quenching and during short-term annealing as well as the numbers of free defects.

The vacancy clustering scheme is modified so that the vacancy clusters are considered to be loops, and an adjustable factor exaggerates the loop radii. The number of free vacancies is fairly sensitive to vacancy clustering. If vacancy clustering is too efficient, then no vacancies become freely migrating because they are all in large clusters. The free vacancies which remain after short-term annealing often tend to originate from small clusters which are reduced to mobile size by recombination.

The number of free interstitials is fairly insensitive to the quenching parameters. Extreme enhancement of interstitial clustering during the quench reduces the fraction of mobile interstitials from a maximum of about 35% to a minimum of about 20%. Enhanced interstitial clustering also tends to decrease the number of free vacancies, since fewer free interstitials are available to create mobile vacancy clusters.

The sensitivity of free vacancies to clustering and the insensitivity of free interstitials to clustering are a result of the spatial configuration of the defects in the cascade. The vacancies, in close juxtaposition within the cascade core, are easily clustered. The interstitials tend to be in a diffuse cloud about the vacancies, with a certain percentage of them widely disbursed at the periphery of the cascade. A fraction of these will always exit the cascade volume regardless of what is occuring within the more dense regions.

The quenching parameter values which are the best at present have single point defect critical reaction distances for recombination of 3.3 $\underline{a}$ (lattice parameters), for interstitial clustering of 3.3 $\underline{a}$, and for vacancy clustering of 1.3 $\underline{a}$. The results, averaged over ten 30-keV cascades, are shown in Table 1. The times τ=100, 5 x 10^5, 10^{12} are in units of jumps of a single interstitial and refer to the end of the quench, the end of interstitial migration and the end of the simulation respectively.

TABLE 1

SHORT-TERM ANNEALING OF 30-KEV CASCADES IN CU

	Defect Pairs			Mobile Fraction	
	τ=100	τ=5x10^5	τ=10^{12}	Vacancies	Interstitials
Simulation	97	86	79	5%	20%
Experimental	96 (1)	-	-	4% (4)	15% (3)

There are no direct experimental values for the number of defect pairs remaining after short-term annealing of isolated cascades. However, annealing experiments on low fluence, low temperature irradiated copper, with primary cascade-producing irradiation such as ions or high energy neutrons should provide this information for interacting cascades. After Stage I recovery, there should be few mobile interstitials. Those which have escaped their own cascade will have interacted with another. If one assumes that most of the interstitials which escape a cascade recombine with vacancies of other cascades, then the simulation predicts a Stage I recovery of about 32%. Recovery measurements [7] for Cu irradiated with 400 keV Ar ions and d-Be neutrons at 6K indicate a Stage I recovery of 32-36%. Thus, good agreement is obtained if one assumes all the free interstitials eventually result in recombinations. The disposition of the free defects, within this model, will be established when ALSOME is used to simulate interacting cascades.

5.3 Conclusions

The ALSOME annealing code, run in two stages to model cascade quenching and short-term annealing, operating on 30 keV Cu cascades directly from the MARLOWE code, gives results which are in good agreement with quantities extracted from experimental measurements for the number of defect pairs and mobile defects at various stages of cascade development.

6.0 References

1. H. L. Heinisch, D. G. Doran and D. M. Schwartz, Effects of Radiation on Materials, ASTM Special Technical Publication 725 (1981) 191.

2. M. T. Robinson and I. M. Torrens, Phys. Rev. B, 9 (1974) 5088.

3. U. Theis and H. Wollenberger, J. Nucl. Mater., 88 (1980) 121.

4. T. H. Blewitt, A. C. Klank, T. Scott and W. Weber, Proc. International Conference on Radiation-Induced Voids in Metals, Albany, NY, 1971, J. W. Corbett, L. C. Ianniello (Eds.), NTIS, CONF-710601 (1972) 757.

5. J. A. Goldstone, D. M. Parkin and H. M. Simpson, J. Appl. Phys., 51 (1980) 3690.

6. J. B. Sanders, Rad. Effects, 51 (1980) **43.**

7. R. S. Averback, R. Benedek and K. L. Merkle, **3.** Nucl. Mater., 75 (1978) 162.

7.0 Future Work

The energy dependence of the quenching and short-term annealing will **be** investigated. Short-term annealing of interacting cascades will be modeled.

14-MEV NEUTRON IRRADIATION OF COPPER ALLOYS

S. J. Zinkle and G. L. Kulcinski (University of Wisconsin-Madison)

1.0 Objectives

The objectives of this experiment are: 1) to determine defect survivability in copper alloys irradiated at room temperature with 14-MeV neutrons and the influence of solute additions, and 2) to determine whether resistivity measurements can provide useful information on defect survivability when used in conjunction with TEM.

2.0 Summary

Resistivity models found in the literature have been studied in an attempt to analyze the resistivity results of Cu and Cu alloys irradiated with 14 MeV neutrons at room temperature. The unsaturable trap model (UTM) has been found to give reasonable results in the present study. Using the UTM, we have estimated that at least 12% of the defects originally created survive the cascade event.

The effect of clustering on resistivity has also been reviewed. It is found that, to a first approximation, the resistivity of a small cluster ($d < 30$ Å) may be equated to the sum of the resistivities of the individual defects. More refined calculations will require detailed TEM results for defect clusters which are approaching the resolution limit of the electron microscope.

3.0 Program

Title: Radiation Effects to Reactor Materials
Principal Investigators: G. L. Kulcinski and R. A. Dodd
Affiliation: University of Wisconsin

4.0 Relevant DAFS Program Task/Subtask

Subtask II.B.3.2 Experimental Characterization of Primary Damage State; Studies of Metals

Subtask II.C.6.3 Effects of Damage Rate and Cascade Structure of Microstructure; Low-Energy/High-Energy Neutron Correlations

Subtask II.C.16.1 14-MeV Neutron Damage Correlation

5.0 Accomplishments and Status

5.1 Introduction

Electrical resistivity measurements are one of the oldest methods used to study defect concentrations in metals. Various theoretical models can be found in the literature which have been used to explain both electron[1-3] and neutron[4] irradiation-induced resistivity changes. These models have been applied to the resistivity results obtained from a room temperature, 14 MeV neutron irradiation of Cu and Cu alloys.[5]

The three electron resistivity models mentioned above are all variations of a model first proposed by Walker,[1] known as the unsaturable trap model (UTM). In this model, it is assumed that the vacancy is immobile, while the interstitial is mobile and can go to one of several trapping sites: (1) a saturable trap, i.e. a trap which once occupied cannot accommodate any new interstitials. Impurities may be considered as saturable traps. (2) Unsaturable traps, i.e. a trap which can accept interstitials without limit without changing its probability for subsequent interstitial capture. Dislocations and grain boundaries are examples of unsaturable traps. (3) Annihilation with a vacancy.

5.2 Results

Following the analysis of Dworschak et al.[2] using the UTM, the following equations are obtained

$$\frac{d\rho}{d\Phi} = f\sigma_d \rho_F^t \frac{\Gamma_t C_t \rho_F^t}{\Gamma_t C_t \rho_F^t + \Gamma_v \Delta\rho} \tag{1}$$

$$\Delta\rho = \rho_F^t \frac{\Gamma_t C_t}{\Gamma_v} \left\{ \sqrt{1 + \frac{2f\sigma_d \Phi}{\Gamma_t C_t / \Gamma_v}} - 1 \right\} \tag{2}$$

This may be written in the form

$$\frac{\Phi}{\Delta\rho} = \frac{1}{f\sigma_d \rho_F^t} \left(1 + \frac{\Delta\rho}{2C_t \rho_F^t \Gamma_t / \Gamma_v}\right) \tag{3}$$

where f is the fraction of interstitials escaping correlated recombination, σ_d is the displacement cross section, ρ_F^t is the resistivity increment per unit concentration (i.e. 100%) of Frenkel defects, Γ_t and Γ_v are the capture radii of spherical capture volumes of impurity traps and vacancies, respectively, for migrating interstitials, C_t is the concentration of impurities (at/at), and $\Delta\rho$ is the radiation induced residual resistivity increase. It may be seen from Eq. (2) that the asymptotic value of the resistivity change at large fluences scales as $\sqrt{\Phi}$, in agreement with reported experimental results.[5]

A linear relation may be obtained by plotting the quantity $\Phi/\Delta\rho$ vs. $\Delta\rho$, as shown in Figure 1. The intercept of this curve is given by $1/f\sigma_d\rho_F^t$, and the slope is equal to $(1/f\sigma_d\rho_F^t)(1/2C_t\rho_F^t(\Gamma_t/\Gamma_v))$. A least-squares fit to the data yields the relation

$$f\sigma_d\rho_F^t = 9.0 \times 10^{-26} \text{ n-cm}^3$$

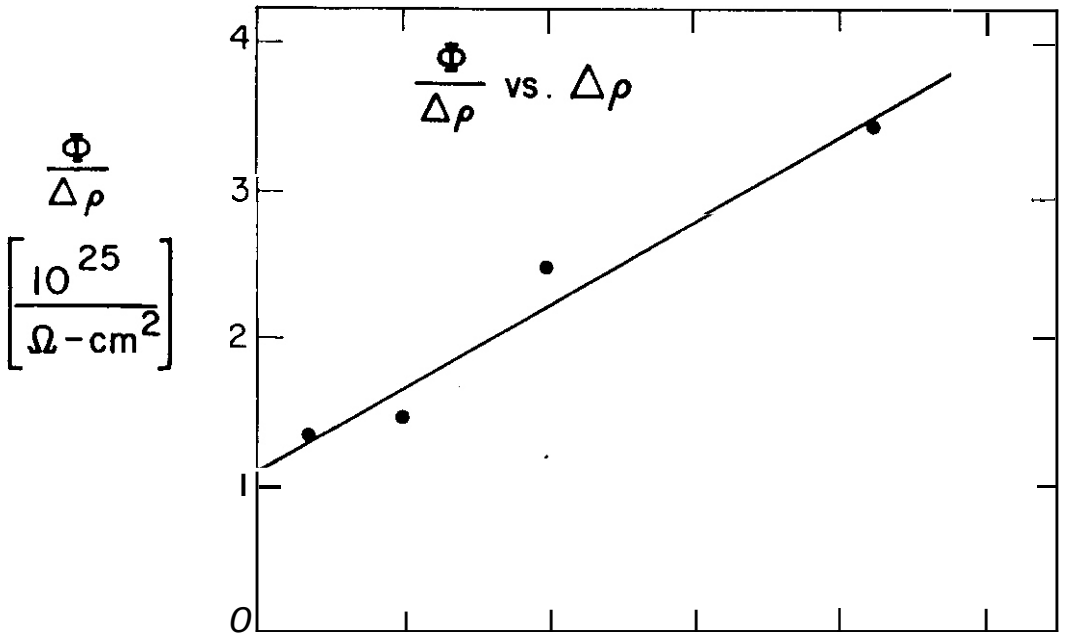

FIGURE 1. Plot of the 14 MeV neutron fluence divided by the radiation-induced resistivity change as a function of the amount of radiation-induce resistivity change for pure copper irradiated to a total fluence of 3×10^{17} n/cm^2 at room temperature.

The quantity ρ_F^t depends on the amount of clustering which has occurred. To obtain a lower limit for the fraction of defects escaping correlated recombination, ρ_F^t may be taken to be equal to the isolated Frenkel pair specific resistivity,[6] $\rho_{F.P.} = 2.0 \times 10^{-6}$ Ω-cm/%F.P.. As will be shown later, the effect of clustering is small for clusters smaller than ~ 30 A and TEM analysis of copper irradiated under identical conditions[7] has shown that most of the clusters are smaller than 30 A. Using a displacement cross section of σ_d = 3690 barns[8] then gives $f \gtrsim 12.1\%$.

These defects may then aggregate to form clusters and loops. This value is in good agreement with the results found by Brager et al.,[6] who found that the number of defects surviving the cascade was at least 9.7%.

5.3 Discussion

The good agreement between the analysis of the resistivity results using the unsaturable trap model and Brager's[7] results is somewhat surprising and may be coincidental. The UTM was developed assuming immobile vacancies and no effect of clustering on the resistivity results. Stage III in copper begins at or slightly below room temperature, and so vacancies should be considered to be mobile during irradiation. Unfortunately, it is difficult to obtain a quantitative estimate of the effect of vacancy mobility on the results. At room temperature, the diffusivity of an interstitial in copper is much greater than for a vacancy (factor of 10^8) so it may be assumed that the vacancy is relatively stationary compared to the interstitial. Since the mechanism of diffusion for vacancies and interstitials is similar and TEM observations of 14-MeV neutron-irradiated copper show approximately the same cluster distributions for both vacancies and interstitials,[9] it is believed that it is a good approximation to replace Dworschak's definition of f (f = fraction of interstitials escaping correlated recombination) with f = fraction of defects escaping correlated recombination.

Theoretical studies of small vacancy and interstitial clusters have shown that there is only a weak effect of clustering on resistivity results.[10,11] However, if these clusters collapse into dislocation loops, then the resistivity contribution per defect can be greatly reduced for large loops. The study of the resistivity contribution of dislocations is an old and difficult problem which has only recently been solved theoretically with satisfactory results.[12] There is evidence[6,13] that it is a good approximation to model the resistivity increase due to a dislocation loop as the resistivity due to a dislocation line of length $2\pi R$ (R equals the radius of the loop) plus the resistivity due to the stacking fault, as applicable. The reason this approximation is reasonable is because most of the resistivity increase in dislocations is due to scattering from the dislocation core. Therefore, the resistivity is ~~not~~ sensitive to dislocation arrange-

ments. Table 1 gives the specific resistivity of dislocations and stacking faults for copper along with two other representative metals for comparison.

For a perfect dislocation loop of diameter **d**, the resistivity is given by

$$\rho_{loop} = (\pi dN)\rho_d \tag{4}$$

where N = number of loops/cm^3.

The resistivity of a cluster of the same size is

$$\rho_{cluster} = \rho_{F.D.} \frac{nd^2 b}{4\Omega_d N_{Cu}} N \tag{5}$$

where **b** = burgers vector = $a_o/\sqrt{2}$
$\rho_{F.D.}$ = specific resistivity of Frenkel defect
Ω_d = atomic volume of defect
N_{Cu} = $4/a_o^3$ = atomic density of copper.

TABLE 1

EXPERIMENTALLY MEASURED AND THEORETICAL VALUES OF RESISTIVITY FOR STACKING FAULTS AND DISLOCATIONS

ρ_{SF}/α [10^{-13} o-cm2]			ρ_d/β [10^{-19} Ω-cm^3]			Reference
cu	Al	Au	cu	Al	Au	
2.5-10, 90-100	---	1.0 ± 0.2	---	---	---	14
< 60	4.0	1.8	---	---	---	15
-"-	---	---	1.3 ± 0.1	1.5 ± 0.3	2.6	12

a = stacking fault density [cm^2/cm^3]
E = dislocation density [cm/cm^3]

Taking $\Omega_d N_{Cu} = 1$ gives

$$\frac{\rho_{loop}}{\rho_{cluster}} = \frac{4\rho_d}{b\rho_{F.D.}} \frac{1}{d} . \qquad (6)$$

For an interstitial cluster ($\rho_{F.D} = 1.4 \times 10^{-6}$ Ω-cm/% defects)[6] this ratio equals unity for d = 10 A. A 25 A diameter perfect loop has a ratio $\rho_{loop}/\rho_{cluster} = 41\%$. For a vacancy cluster ($\rho_{F.D.} = 0.6 \times 10^{-6}$ Ω-cm/% defect),[6] a 25 A diameter loop has a ratio $\rho_{loop}/\rho_{cluster} \simeq 1$.

For a faulted dislocation loop of diameter d, the resistivity is given by

$$\rho_{loop} = \pi d N \rho_d + \frac{\pi d^2}{4} N \rho_{S.F.} \qquad (7)$$

and therefore

$$\frac{\rho_{loop}}{\rho_{cluster}} = \frac{\rho_{S.F.}}{b\rho_{F.D.}} + \frac{4\rho_d}{b\rho_{F.D.}} \frac{1}{d} . \qquad (8)$$

For an interstitial loop with $b = a_o/\sqrt{3}$ and $\gamma_{S.F} = 10 \times 10^{-13}$ Ω-cm^2 this ratio becomes

$$\frac{\rho_{loop}}{\rho_{cluster}} = \begin{cases} 0.7 & d = 50 \text{ Å} \\ 1 & d = 25 \text{ Å} \end{cases}$$

It is therefore seen that for a cluster distribution containing both faulted and unfaulted loops it is a reasonable first approximation to neglect the effect of clustering if the cluster distribution is small ($\lesssim$ 25 Å). This condition is satisfied in the present experiment. However, to obtain more accurate results, it is necessary to obtain from TEM analysis (1) the percentage of faulted and unfaulted loops, and (2) the detailed cluster distribution. These parameters are difficult to determine for experiments similar to the present one since the cluster size is approaching the resolution limit of the electron microscope.

There is also some question about what is the critical size required to cause collapse of a cluster into a dislocation loop. Theoretical estimates range from six[6,16] to 400 defects.[17] Bullough and Perrin[18] used an elastic continuum model and found that a plate-like cluster would collapse into a loop for a cluster sizes greater than 22 vacancies.

5.4 Conclusions

The unsaturable trap resistivity model has been applied to a room temperature 14 MeV neutron irradiation of copper with satisfactory results. It is estimated that at least 12% of the defects created by the irradiation survive the cascade event and migrate to form clusters. A more accurate determination of the defect survival fraction requires more detailed TEM work. It appears that resistivity measurements can be a useful tool for determining defect survivability when used in conjunction with TEM measurements.

6.0 References

1. R. M. Walker in "Radiation Damage to Solids," Proceedings of the International School of Physics, (Enrico Fermi) Course XVIII, ed. by D. S. Billington, p. 594, (1962).
2. F. Oworschak et al., J. Physics F, 5, 400 (1975).
3. R. Poerschke and H. Wollenberger, J. Nucl. Mat., 74, 48 (1978).
4. J. A. Horak and T. H. Blewitt, Phys. Stat. Sol., 9, 721 (1972).
5. S. J. Zinkle and G. L. Kulcinski, "14-MeV Neutron Irradiation of Copper Alloys," DAFS Quarterly Progress Report (August-December 1981).
6. R. C. Birtcher and T. H. Blewitt, J. Nucl. Mat., 98, 63 (1981).
7. H. R. Brager et al., "Damage Development and Hardening in 14 MeV Neutron Irradiation of Copper Alloys at 25°C," paper presented at the 2nd Topical Meeting on Fusion Reactor Materials, August 9-12, 1981, Seattle, WA. Proceedings to be published in J. Nucl. Mat..

8. D. G. Doran and N. J. Graves, "Displacement Cross-Sections and PKA Spectra: Tables and Applications," USERDA Report HEDL-TME 76-70 (December 1976).

9. J. B. Mitchell et al.. "DT Fusion Neutron Radiation Strengthening of Copper and Niobium," Radiation Effects and Tritium Technology for Fusion Reactors, J. S. Watson and F. W. Wiffen (Eds.), Gatlinburg, TN, (1975), Vol. II, p. 172.

10. J. W. Martin and R. Paetsch, J. Physics F, 3, 907 (1973).

11. J. W. Martin, J. Physics F, 2, 842 (1972).

12. R. A. Brown, J. Physics F, 7, 1283 (1977).

13. J. G. Rider and C. T. B. Foxon, Phil. Mag., 13, 289 (1966).

14. J. Poldk, Phys. Stat. Sol., 11, 673 (1965).

15. R. A. Brown, Phys. Rev., 156, 692 (1967).

16. E. J. Savino and R. C. Perrin, J. Physics F, 4, 1889 (1974).

17. J. A. Sigler and D. Kuhlmann-Wilsdorf. The Nature of Small Defect Clusters, Report of a Consultants Symposium held at AERE, Harwell, July 4-6, 1966, AERE Report R-5269, ed. by M. J. Makin, p. 125.

18. R. Bullough and R. C. Perrin, Radiation Damage in Reactor Materials, Vol. II, Vienna IAEA, (1969), p. 233.

7.0 Future Work

Resistivity results from copper alloys irradiated to a fluence of 3 x 10^{17} n/cm^2 will be examined in an attempt to determine defect survivability. Micro-hardness and TEM investigations of the copper and copper alloys will be undertaken at HEDL.

CHAPTER 3

FUNDAMENTAL MECHANICAL BEHAVIOR

YIELD STRENGTH–MICROHARDNESS COMPARISONS IN 14–MeV NEUTRON–IRRADIATED VANADIUM AND TITANIUM

E. R. Bradley (Pacific Northwest Laboratory)

1.0 Objective

The purpose of this study is to determine the effects of 14–MeV neutron irradiation on the strength and microstructure of materials whose properties are sensitive to interstitial impurities. The ultimate application of this work is to identify potential material impurity limits for the successful operation of fusion reactors.

2.0 Summary

Yield strength and microhardness measurements have been made on vanadium and titanium specimens following irradiation at 25°C with 14–MeV neutrons. Five fluence levels, ranging from 1×10^{21} to 2×10^{22} m^{-2}, were examined. The yield strength in both materials increased with irradiation and approximately followed a $(\phi t)^{0.5}$ fluence dependence. Microhardness measurements in the vanadium increased with irradiation to 6×10^{21} m^{-2} and remained constant thereafter. No significant microhardness increase was observed in the titanium until the highest fluence level (2×10^{22} m^{-2}), where a small increase was noted. These results suggest that yield strength-microhardness correlations in irradiated metals may be limited to specific materials and neutron fluences. The flow characteristics of irradiated metals were found to be important in interpreting microhardness data.

3.0 Program

Title: Mechanical Properties
Principal Investigator: R. H. Jones
Affiliation: Pacific Northwest Laboratory

4.0 Relevant DAFS Program Plan Task/Subtask

Subtask II.C.6	Effects of Damage Rate and Cascades on Microstructures
Subtask II.C.11	Effects of Cascades and Flux on Flow
Subtask II.C.18	Relating Low- and High-Exposure Microstructures

5.0 Accomplishments and Status

5.1 Introduction

The effects of high-energy neutron irradiation on the mechanical properties of potential fusion reactor materials are important for the design and operation of fusion reactors. Since the irradiation volumes for high-energy neutrons are small, miniature specimens have been used to measure mechanical properties. Tensile tests on irradiated wire[1,2] and sheet[3] specimens have been used to successfully determine the effects of high-energy neutron irradiation on the yield strength of metals and alloys. Microhardness data are also being used to obtain mechanical property data from small specimens, and correlations between microhardness and tensile properties have been reported for some materials.[4,5] Additional information on correlating mechanical property data from miniature specimens is needed to assure the reliability of the correlations for different materials and irradiation conditions.

This report presents yield strength and microhardness data for vanadium and titanium as a function of 14-MeV neutron fluence. Except for the highest fluence level, yield strength data have been presented and discussed previously;[2] consequently, the relationships between yield strength and microhardness in vanadium and titanium are emphasized in this report.

5.2 Experimental Procedures

The 0.5-mm diameter titanium wire and 0.1-mn thick titanium foil were obtained from A. D. MaKay, Inc.; Materials Research Corporation supplied the 0.5-mm

diameter vanadium wire; and the vanadium foil material was prepared from wire stock by cross-rolling to about 0.1 mm. Chemical analysis of the wire materials indicated a total interstitial impurity content of 500 wt-ppm for the titanium and 1300 wt-ppm for the vanadium. Oxygen was the primary impurity in both materials; with concentrations of 400 and 920 wt-ppm, respectively, for titanium and vanadium.

Vanadium and titanium wires were annealed in vacuum (10^{-5} Pa) for 1 hr, straightened by a small amount of plastic deformation, and annealed for an additional hour prior to irradiation. Annealing temperatures for the vanadium and titanium specimens were 1223K and 873K, respectively. These procedures produced an equiaxed grain size of about 25 μm in the vanadium and 10 μm in the titanium. The same annealing treatment was used on the foil materials.

The foil and wire specimens were placed in adjacent planes within 1.5-mm thick capsules and were irradiated at 25°C with 14-MeV neutrons obtained from the RTNS II at LLNL.(a) The specimen fluence was determined by the average readings from niobium dosimeters that were located at the front and back of the capsules. The position of the capsules relative to the neutron source was periodically reversed during the irradiation to minimize differences in fluence between the foil and wire specimens. The average fluence for these experiments ranged from 1×10^{21} to 2×10^{22} m^{-2}

Autoradiographs were used to locate the position of the neutron beam on the specimens after irradiation, and gage sections (0.25 by 5 mm) were produced by electropolishing the wire specimens at this location. The minimum diameter along the gage sections was measured with an optical microscope equipped with a calibrated eyepiece. The average of five measurements around the circumference of the specimen was used to calculate tensile properties.

(a) RTNS II - Rotating Target Neutron Source II. LLNL - Lawrence Livermore National Laboratory.

Flow stress determinations were made by uniaxially straining the wire specimens in an Instron tensile testing machine. The strain rate was $3 \times 10^{-4}\ s^{-1}$, and the tests were conducted at room temperature. The specimens were held in split grips, and the displacement of the grips was measured by a linear variable differentia1 transformer (LVDT). The average tensile properties of a given material and fluence were determined from six to eight specimens.

Microhardness measurements were made on 3-mm diameter transmission electron microscope (TEM) discs using a TUKON microhardness testing machine with a Vickers diamond point indenter (100-g load). Measurements were taken from the central portion of the discs to avoid edge effects, and average microhardness values for a given material and fluence were determined from at least eight measurements.

5.3 Results

The tensile and microhardness data for the vanadium and titanium specimens in Table 1 represent the average and standard deviations of the respective measurements for each fluence level. Except for the upper yield point in the vanadium specimens, the standard deviations are less than 10%. The upper yield point was sensitive to the alignment of the grips, which is reflected by the higher standard deviations. The microhardness numbers were converted to flow stress, σ_f, using the relation[4]

$$\sigma_f = 3.27\ \mathrm{OPH} \qquad (1)$$

where DPH is the Vickers hardness number in kg/mm^2.

5.3.1 Vanadium

No consistent correlation between yield strength and microhardness was observed in the irradiated vanadium. The measured yield strength increase and the increase calculated from the microhardness data are plotted as a

TABLE 1

SUMMARY OF TENSILE AND MICROHARDNESS DATA

Material	Neutron Fluence, m^{-2}	Tensile UYS, MPa	Tensile LYS,(a) MPa	Tensile UTS, MPa	Microhardness DPH, kg/mm^2	Microhardness σ_f, MPa
Vanadium	0	470 *80	340 *30	400 *30	150 ±2.7	490 ±9
	1.3×10^{21}	495 *15	350 *30	390 ±20	-	-
	2.9×10^{21}	545 *75	400 ±25	410 *30	164 ±6.8	536 *22
	5.6×10^{21}	555 ±110	430 *15	-	175 ±6.6	572 ±21
	8.3×10^{21}	590 ±90	445 *30	-	175 ±5.8	572 ±19
	2.0×10^{22}	630 ±50(b)	520 ±30(b)	-	174 ±8.3	569 *27
Titanium	0		220 ±10	320 ±20	134 ±2.6	438 ±9
	1.3×10^{21}		230 ±10	315 *15	136 ±2.6	445 ±9
	2.9×10^{21}		250 ±15	335 *15	136 ±3.8	445 *12
	5.6×10^{21}		260 *15	320 *15	135 ±4.0	441 *13
	5.7×10^{21}		270 *15	330 *15	-	-
	8.3×10^{21}		290 ±10	340 ±10	137 ±4.4	448 *14
	2.0×10^{22}		300 *20	335 ±15	142 ±6.3	464 *21

(a) 0.2% yield strength for titanium.
(b) Unirradiated tensile properties UYS = 490 *60 MPa and LYS = 375 *25 MPa.

function of fluence in Figure 1. The lower yield strength increased continuously with irradiation, and the data approximately followed a $(\phi t)^{0.5}$ fluence dependence. The strength increases that were calculated from the microhardness data showed reasonable agreement with the tensile data up to a fluence of 6×10^{21} m^{-2}, above which the microhardness saturated and the yield strength continued to increase with fluence. These results indicate that yield strength-microhardness correlations in vanadium irradiated at 25°C are limited to a relatively small neutron fluence range.

The saturation in microhardness for fluences above 6×10^{21} m^{-2} is probably associated with the change in flow characteristics that was observed in the irradiated specimens. The load-elongation curves for the unirradiated wires

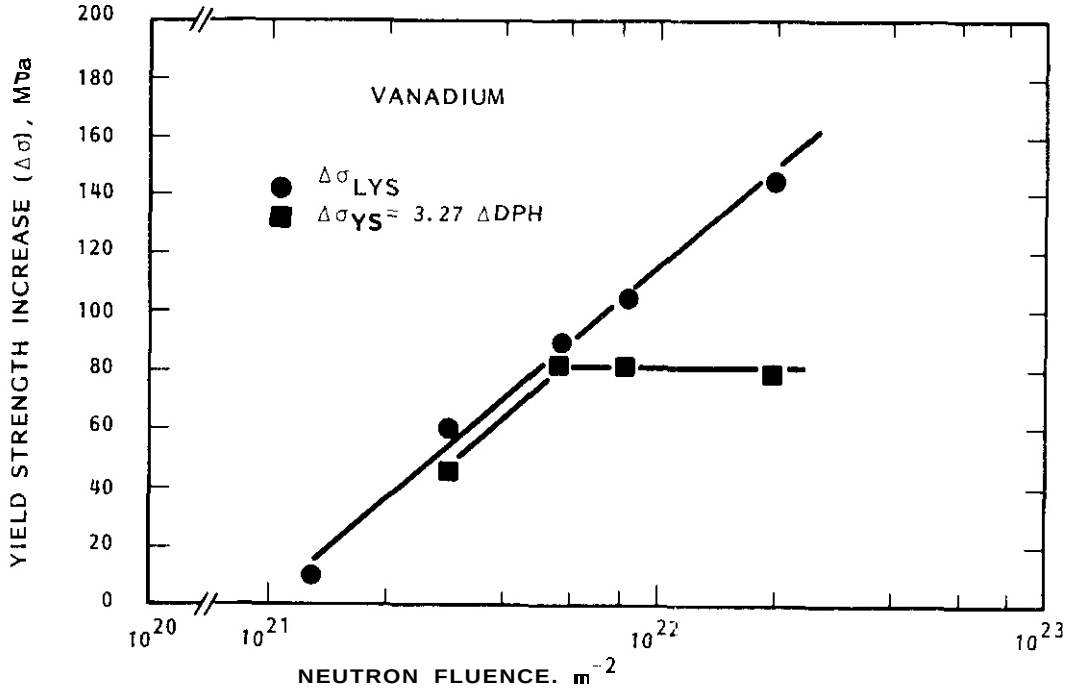

FIGURE 1. Comparison of Measured Yield Strength Increase and Calculated Increase Based on Microhardness Data for Irradiated Vanadium

consisted of upper and lower yield regions, a region of uniform strain with its associated strain hardening, and finally, plastic instability that led to ductile failure. Reductions in area were about 80% at fracture. The predominant effect of neutron irradiation was to reduce or eliminate the homogeneous flow portion of the curves. At fluence levels of 6×10^{21} m^{-2} and above, plastic instability occurred immediately after yielding. Ductile failures were observed with no change in the reduction in area at fracture.

Similar flow behavior has been observed in fission neutron-irradiated vanadium[6] and vanadium alloys[7] and was explained by dislocation channeling. The irradiation-produced obstacles to dislocation glide are swept from the lattice by the initial movement of dislocations. Further deformation is localized in these softer regions of the lattice, and plastic instability occurs immediately after yielding. Little or no strain hardening is observed under these conditions.

5.3.2 Titanium

No direct correlation between yield strength and microhardness was found in the titanium specimens (see Figure 2). The yield strength increased continuously with irradiation and approximately followed a $(\phi t)^{0.5}$ fluence dependence. Microhardness measurements showed no significant increase until the highest fluence level (2×10^{22} m^{-2}), where a small increase was noted. The fluence dependence of the yield strength in titanium was similar to that observed in vanadium, but the response of microhardness to neutron irradiation differed in the two materials.

Load-elongation curves for titanium showed the parabolic-type hardening that is typical of fcc and hcp polycrystalline materials. The load increased with deformation due to strain hardening until the ultimate tensile strength was reached. Plastic instability then led to ductile failure after about 80%

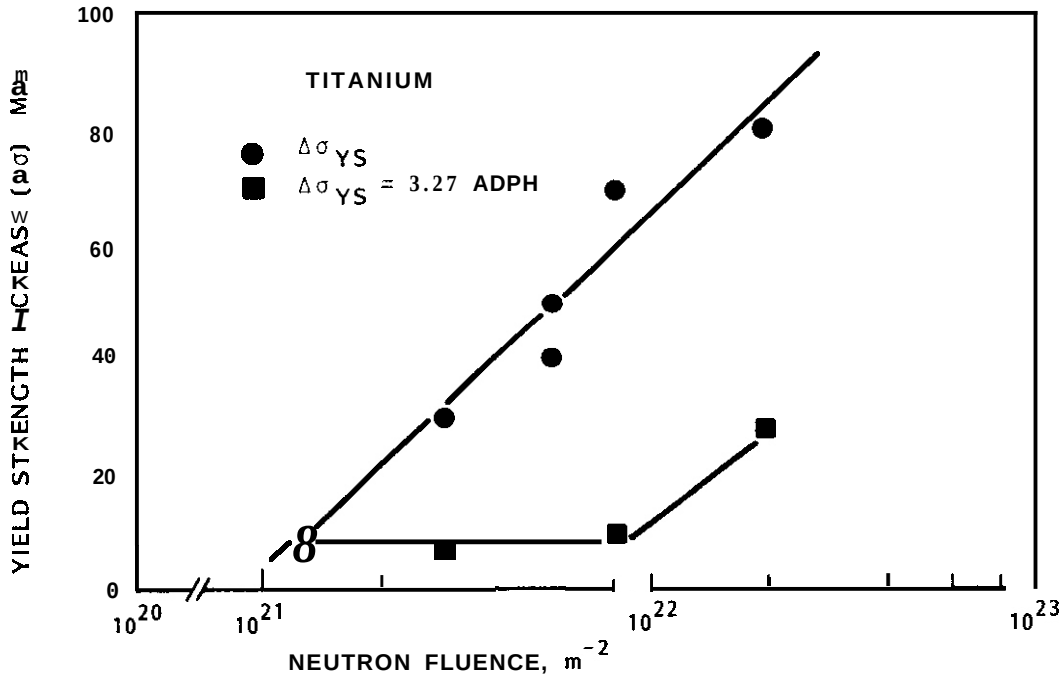

FIGURE 2. Comparison of Measured Yield Strength Increase and Calculated Increase Based on Microhardness Data for Irradiated Titanium

reduction in the cross-sectional area. The ultimate strength was unaffected by neutron irradiation. A small decrease in total elongation was observed, which is consistent with the lower amount of strain hardening in the irradiated specimens.

5.4 Discussion

These results suggest that yield strength-microhardness correlations in irradiated metals may be limited to specific materials and fluence ranges. The flow characteristics and microstructural features that are responsible for the observed strength measurements can influence these correlations.

The increased yield strength in irradiated metals is caused by irradiation-produced obstacles to dislocation movement. For the irradiation conditions used in these experiments, small defect aggregates or clusters represent the primary obstacles. Thompson[8] predicted a $(\phi t)^{0.5}$ fluence dependence for radiation-induced defect strengthening, which is consistent with the present results obtained from tensile tests of vanadium and titanium wires. A similar fluence dependence has also been reported in 14-MeV neutron-irradiated nickel[9] and copper.[4]

Microhardness is a complex mechanical property that depends on both the yield strength and strain-hardening characteristics of the material. Equation 1 is based on an empirical relation between the Vickers indenter hardness number (DPH) and the true flow stress at about 8% strain.[10] At this strain level, dislocation substructures are well developed and provide a significant contribution to the true flow stress. Neutron irradiation can influence both the yield strength and the density and distribution of dislocations formed during the deformation process. This is especially evident when dislocation channeling removes the irradiation-produced defects from the lattice and dramatically changes the dislocation distributions. Dislocation channeling is a general phenomenon in metals irradiated at low temperatures; therefore,

other yield strength–microhardness correlations from low–temperature irradiation data may be restricted to a limited fluence range as was observed in the irradiated vanadium.

In addition to a potential change in dislocation distribution, a change in deformation mode may also have contributed to the results obtained for the irradiated titanium. Higashiguchi and Kayano[11] found that neutron irradiation enhanced deformation twinning in titanium. Their results indicate that deformation was initiated by dislocation slip; but at higher strain levels, deformation proceeded by a combination of slip and mechanical twinning. The contribution from twinning increased with neutron fluence, and dislocation channeling was observed at higher fluence levels. If similar deformation processes occurred in the high–energy neutron–irradiated titanium wires, the difference in microhardness response between the titanium and vanadium may be related to the enhanced mechanical twinning in the titanium. Although a detailed analysis of deformation characteristics would be required to confirm this suggestion, the present results clearly indicate the need to consider deformation characteristics when interpreting yield strength–microhardness correlations.

5.5 Conclusions

Comparing the yield strength and microhardness responses to 14–MeV neutron–irradiated vanadium and titanium has led to the following conclusions:

- No consistent relationships were found between yield strength and microhardness in vanadium or titanium irradiated at 25°C with 14–MeV neutrons over the fluence range from 1×10^{21} to 2×10^{22} m^{-2}
- Dislocation channeling appeared to limit the fluence range for yield strength–microhardness correlations to below 6×10^{21} m^{-2} in vanadium.

- Deformation characteristics need to be considered when interpreting yield strength-microhardness correlations.

6.0 References

1. R. H. Jones et al.. "Microstructure and Tensile Properties of T (d,n) and Be (d,n) Neutron Irradiated Nickel, Niobium, and 316 SS," J. Nucl. Mat. 85-86, 889-893 (1979).

2. E. R. Bradley and R. H. Jones, "Strength Changes in Vanadium and Titanium Irradiated with 14 MeV Neutrons," PNL-SA-9287, in Proceedings of the Second Topical Meeting on Fusion Reactor Materials, Seattle, Washington, August 1981.

3. J. B. Mitchell, Exploratory Experiments Comparing Damage Effects of High Energy Neutrons and Fission-Reactor Neutrons in Metals, UCRL-52388, Lawrence Livermore Laboratory, Livermore, California (1978).

4. N. F. Panayotou, "Prediction of the Change in the Offset Yield Strength of Copper Due to High Energy Neutron Irradiation Using Vickers Micro-Hardness Data," DAFS Quarterly Progress Report, DOE/ER-0046/5, 65 (1981).

5. G. E. Lucas and F. Haggag, "The Role of Luders Strain in Determining Flow Properties in Steel from an Instrumented Hardness Test," DAFS Quarterly Progress Report, DOE/ER-0046/6, 105-114 (1981).

6. G. R. Smolik and C. W. Chen, "Radiation Hardening in Vanadium," J. Nucl. Mat. 35, 94 (1970).

7. F. W. Wiffen "The Effect of 70°C Irradiation on the Tensile Properties of Vanstar-7," ADIP Quarterly Progress Report, DOE/ET-0045/7, 145-153 (1981).

8. M. W. Thompson, Defects and Radiation Damage in Metals, Cambridge University Press, 344 (1969).

9. R. H. Jones, E. R. Bradley, and D. L. Styris, "Flow Behavior of Nickel Irradiated with 14-MeV Neutrons and 16-MeV Protons," PNL-SA-9592, submitted to J. Nucl. Mat.

10. F. A. McClintock and A. S. Argon, Mechanical Behavior of Materials, Addison-Wesley, Reading, Massachusetts, 443-465 (1966).

11. Y. Higashiguchi and H. Kayano, "Twinning Deformation at Room Temperature of Fast-Neutron Irradiated Titanium," Radiation Effects 45, 225-234 (1980).

7.0 Future Work

Work will continue on determining the combined effects of high-energy neutron irradiation and impurities on the mechanical properties of fusion reactor materials. The effects of oxygen in niobium will be determined by comparing the yield strength increase in niobium doped with 300 wt-ppm oxygen to data from undoped specimens obtained previously in this program. The Nb-O specimens have been irradiated with 14-MeV neutrons at 25°C to fluence levels ranging from 1×10^{21} to 2×10^{22} m^{-2}. Yield strength-microhardness comparisons will also be made for these materials.

CRITICAL FLAWS IN FUSION REACTOR MATERIALS

R. H. Jones (Pacific Northwest Laboratory)

1.0 Objective

The purpose of this evaluation was to identify critical flaws in fusion reactor first walls. Comparisons between the size of flaws which allow coolant leakage into the plasma, threshold flaw sizes for fatigue stress or environmentally induced sub-critical crack growth and flaw sizes for unstable crack growth were made. Degradation processes which reduce critical flaw sizes were also evaluated.

2.0 Summary

Critical leak rate, fatigue and environmentally induced sub-critical crack growth and unstable crack growth flaw sizes for austenitic and ferritic stainless steels were compared. The results of this analysis indicate that the critical leak rate flaw size is about 0.2 mm, the threshold flaw sizes for fatigue and corrosion fatigue sub-critical crack growth of 316 SS and HT-9 range from 0.2 to 2 mm and the flaw sizes for unstable crack growth of irradiated 316 SS and HT-9 are 4 mm and 50 mm, respectively. These results suggest that the threshold for sub-critical crack growth in fatigue is a critical material property. Also, creep processes are shown to have a significant effect on the critical leak rate flaw size.

3.0 Program

Title: Mechanical Properties
Principal Investigator: R. H. Jones
Affiliation: Pacific Northwest Laboratory

4.0 Relevant DAFS Program Plan Task/Sub-Task

II.C.8. Effects of Helium and Displacements on Fracture

II.C.9. Effects of Hydrogen on Fracture

II.C.12. Effects of Cycling on Flow and Fracture

5.0 Accomplishments and Status

5.1 Background

The lifetime of fusion reactor first wall materials will be a function of many factors such as load, temperature and neutron irradiation history and plasma–wall and coolant–wall interactions. Fatigue crack growth has been identified by Cramer et al.[1] as the primary structural failure mode for Tokamak first walls. More recently, Watson et al.[2] evaluated the effect of irradiation creep, swelling, wall erosion and embrittlement on the fatigue life of a Tokamak first wall made of 316 SS. They concluded that fatigue crack growth is the life-limiting process in Tokamak reactors and that the shortest lifetime occurs when a flaw exists on the coolant side. Embrittlement induced by neutron irradiation and surface erosion were predicted to decrease the lifetime by increasing the crack propagation rate.

A fusion reactor–vacuum first wall may lose its vacuum integrity before its structural integrity by allowing coolant to leak into the plasma. A leak before break criterion has been assessed for 20% CW 316 SS by Wolfer and Jones[3] and the results show that unstable flaw growth is favored as the stress and wall thickness increases and the critical stress intensity, K_{IC}, decreases. A leak producing flaw was defined as any through wall flaw which was too small for unstable crack growth. In a separate study, Jones and Bruemmer[4] concluded that a 0.1 mm wide through-wall flaw in a helium cooled reactor would allow the helium concentration in the plasma to reach 50% in a 1000s period. Since first wall thicknesses are expected to be greater than 1 mm, a through wall flaw with a width to length ratio of 1/10 would be sufficient to shut down a reactor. Flaws of this dimension may be present in the as–fabricated first wall or may grow to this dimension during reactor operation. Flaws of this size will be difficult to locate by non–destructive testing, NDT, techniques in a non–radioactive structure and even more difficult once the reactor has been operating and the first wall and blanket structure are radioactive. Since detection of flaws becomes more difficult with

decreasing flaw size it is important to know the smallest critical flaw so that NDT evaluation can be limited to flaws greater than or equal to the critical size.

Analysis of whether a flaw will merely cause a leak or will grow in an unstable manner causing a break is an important aspect of any critical flaw size analysis. Factors which decrease K_{IC} or increase the yield strength, a_Y, will decrease the flaw size for unstable crack growth and hence favor a break before leak failure. Temper, hydrogen and helium ernbrittlement, radiation induced grain boundary segregation and phase changes are processes which can decrease K_{IC} while radiation induced hardening can increase the yield strength.

Sub-critical crack growth can occur in corrosive or hydrogen environments during static or dynamic loading conditions. Static load sub-critical crack growth is commonly called stress corrosion cracking while dynamic load sub-critical crack growth is known as corrosion fatigue. A threshold stress intensity exists below which measureable crack growth cannot be detected in corrosive environments. At static loads this threshold is called the K_{ISCC} while with dynamic loads this threshold is called the ΔK_{ISCC}. A critical flaw size can be derived from these threshold stress intensities which defines the flaw size which will propagate under a given environment and loading condition. Knowledge of the size of the threshold flaw sizes in corrosion fatigue or stress corrosion is important because they may define the smallest flaw size. Environmentally critical flaws do not present as critical a problem for reactor operation as a leak or a break; however, the environmentally enhanced crack growth rate may be sufficiently high that a leak or a break will form in a relatively short time.

The purpose of this research was to determine and compare the critical flaw sizes of fusion reactor materials. These results will be useful for focusing attention on the physical processes controlling the lifetime of fusion reactors with the expectation that systems can be designed which are insensitive to the presence of flaws smaller than those which can be readily detected with NDT techniques. These results may also point out the need for improved NDT techniques or the need for better data to define the critical

flaw sizes. Critical flaw sizes for unstable crack growth, stress corrosion, corrosion fatigue and hydrogen embrittlement for 316 SS and HT-9 are compared to the critical leak rate flaw size.

5.2 Definitions

A critical leak rate flaw is defined as a flaw which allows the coolant to enter the plasma chamber and reach a sufficient concentration to quench the plasma during a burn cycle. A critical leak rate flaw must penetrate the first wall from the coolant side to the plasma side while the crack length is the length of the crack in the toroidal or poloidal field directions. Critical leak rate flaws were calculated for the UWMAK II[5] and NUMAK conceptual reactor designs.

A structurally critical flaw is defined as a flaw which will cause unstable crack growth in a valid plane strain fracture toughness test (ASTM E399) loaded to its yield strength. It is recognized that the stress singularity around the crack tip of a test specimen is represented by a stress intensity factor, K, which is specific to the geometry and stress system of that specimen. Application of the critical flaws given in this report to reactor design is possible by using the appropriate stress intensity formula for the geometry and stress system of a component. The structurally critical crack length was determined from the following relationship:

$$a_{cr} = \frac{K_{IC}^2}{3.9\ \sigma_Y^2} \qquad (1)$$

where K_{IC} is the critical plane strain fracture toughness. A load equal to the yield strength of the material was chosen as a method of rating various materials at equivalent stresses rather than an equal stress since design stresses are frequently a function of the material strength.

Environmentally critical flaws are defined as the flaw size at which subcritical crack growth can no longer be detected for plane strain fracture toughness tests loaded to the yield strength of the material in a hydrogen or corrosive environment. A crack growth rate of 10^{-7} mm s^{-1} was used to define

this threshold. For statically loaded specimens, the threshold in hydrogen is K_{TH}, the threshold in a corrosive environment is K_{ISCC} while the threshold for cyclically loaded specimens is ΔK_{ISCC}.

5.3 Critical Leak Rate Flaws

A flaw which penetrates the vacuum boundary separating the plasma chamber and coolant passages will allow the higher pressure coolant to leak into the plasma chamber. Since the energy loss from the plasma due to Bremsstrahlung radiation is proportional to Z^2, where Z is the atomic or charge number of the impurity, the power loss per atom of coolant which leaks into the plasma increases with increasing Z. For the coolants considered in conceptual designs, the order of increasing Z is helium, lithium, water and lithium-lead. However, the leak rate of the coolants through a flaw is also a function of their phase state and mass. Phase state is important since gases have higher leak rates than liquids. For gases at low pressures where molecular flow conditions control the leak rate, the leak rate is proportional to $(M)^{-\frac{1}{2}}$ where M is molecular weight. The leak rate of liquid coolants such as water or lithium is a complicated process because of the temperature and pressure gradients through the wall. A liquid coolant will be drawn into a flaw by the pressure differential between coolant and plasma chamber and by capillarity. Boiling will occur when the temperature increases and the pressure decreases to the critical temperature-pressure conditions for that liquid. Gas flow conditions will control the flow beyond this point. A detailed analysis is necessary to determine whether capillary flow, evaporation rate or gas flow is the rate limiting step. By contrast, gas flow through orifices is relatively simple with well developed leak rate equations[6]; therefore, the critical leak rate flaw analysis is based on helium coolant leaking into the plasma chamber.

The flow of gases through orifices can be characterized by viscous or molecular flow with a transitional flow condition existing between viscous and molecular flow. Viscous flow occurs at high pressures when the mean free path between gas molecules is small compared to the orifice and intermolecular collisions determine the flow characteristics. Molecular flow occurs at low

pressures when the mean free path between gas molecules is large and mlecular collisions with the walls of the orifice determine the flow characteristics. The conditions which define the limits of each flow regime are as follows:

Viscous: $aP > 500$

Molecular: $aP < 5$

Transition: $5 < aP < 500$

where a is the orifice size in cm and P is the pressure in the orifice in μm of Hg. For flaws in a fusion reactor first wall there is a large pressure drop from the coolant side to the plasma side such that the flow is viscous on the coolant side and molecular on the plasma side. All three conditions exist within a flaw in a fusion reactor first wall so that the leak rate must be determined experimentally. This was done for helium flow through small intergranular creep cracks in 316 SS tubes[4] and it was found that both viscous and molecular flow equations predicted the experimentally measured flow rates with reasonable accuracy. Both equations worked satisfactorily because flow is a combination of viscous and molecular flow; however, the viscous flow equation was more accurate at larger flaw sizes. Therefore, for this analysis, it was assumed that gas flow through flaws originating on the coolant side of a fusion reactor first wall is dominated by viscous flow.

At high pressures, the leak rate of a gas through a rectangular shaped orifice, such as a crack, can be expressed by the following equation:

$$Q = \frac{0.26\ Y\ a^2 \delta^2}{t} \left(\frac{P_1 + P_2}{2}\right) \left(P_2 - P_1\right) \qquad (2)$$

where a is the crack length, δ is the crack opening, t is the wall thickness, P_1 is the pressure on the plasma side, P_2 is the coolant pressure and Y is a function of a/δ. The symbols in equation 2 were chosen to be consistent with fracture mechanics and not gas flow theory since the purpose of this report is to relate the leak rate flaws to structural flaws. The relation between the parameters in equation 2 and a fusion first wall are shown in figure 1.

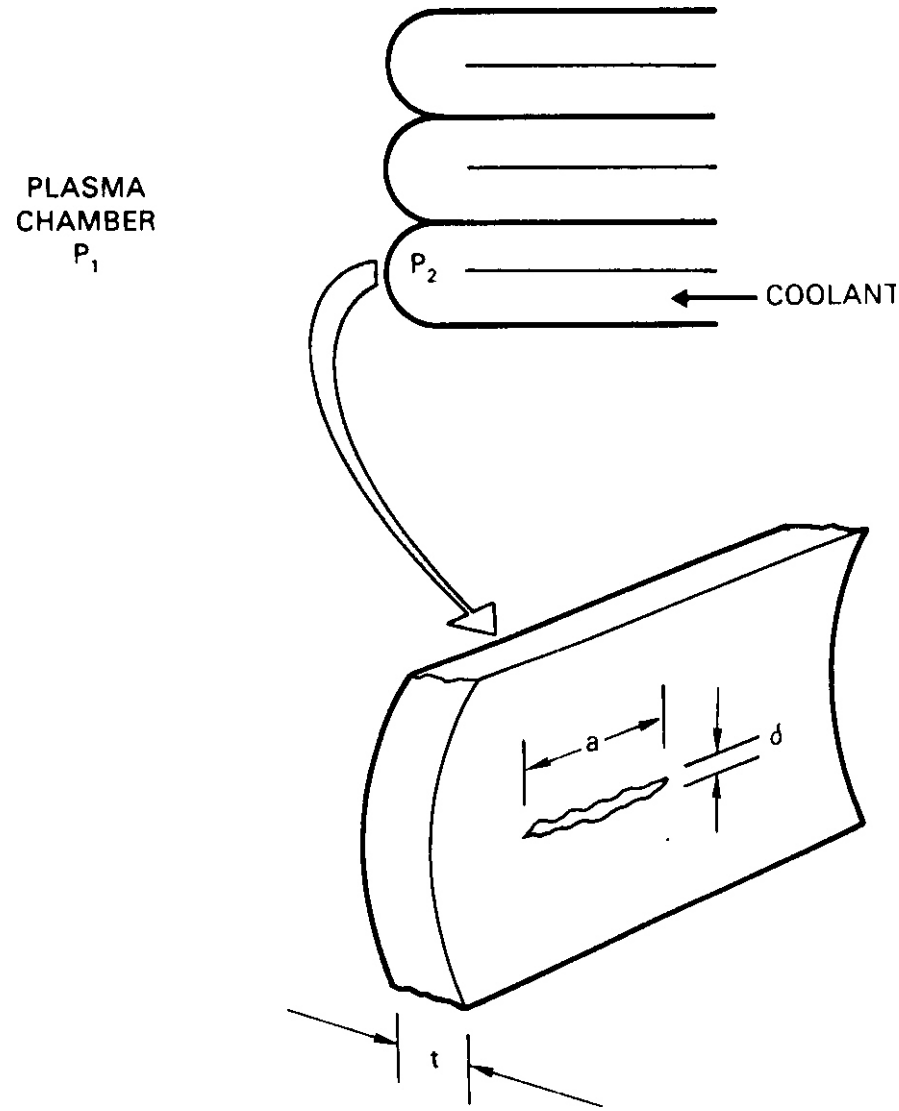

FIGURE 1. Fusion Reactor First Wall and Flaw Geometry

The following assumptions were made in the derivation of equation 2:

1) the gas is incompressible,
2) the flow-velocity profile is constant throughout the flaw,
3) there is no turbulent motion of the gas, and
4) the flow velocity at the tube walls is zero.

For assumptions 2 and 3 to be valid, the cross-section of the orifice should be uniform along the gas flow path. This is clearly not the case for intergranular creep cracks produced in the 316 SS leak rate samples as shown in figure 2d. However, even with these irregularities the viscous flow equation gave flow rate values that were only 5 times larger and equal to the measured flow rates for 0.01 and 0.02 cm long cracks, respectively. Therefore, it was concluded that the viscous flow equation is adequate for estimating the size of a critical leak rate flaw in a fusion reactor but that the resulting flaw size must be considered as an estimate. More quantitative critical flaw size determinations must be made experimentally.

Before equation 2 can be used to estimate the critical leak rate flaw size, a value for Y must be determined. The ratio δ/a can be viewed in two ways: 1) the absence of time dependent flow where δ can be described by fracture mechanics and 2) where time dependent flow causes an increase in δ/a. For case 1, the crack opening can be determined from the following expression[7].

$$\delta = \frac{0.49\ K_I^2}{\sigma_Y E} \qquad (3)$$

where K_I is the mode I stress intensity, σ_Y is the yield strength and E is the tensile elastic mdulus. K_I can be determined from the following expression:

$$K_I = h\ \sigma\ \sqrt{\pi a} \qquad (4)$$

where σ is the stress and h is a constant which is taken to be 1.12 for this analysis. A value of δ/a independent of crack length can be determined using

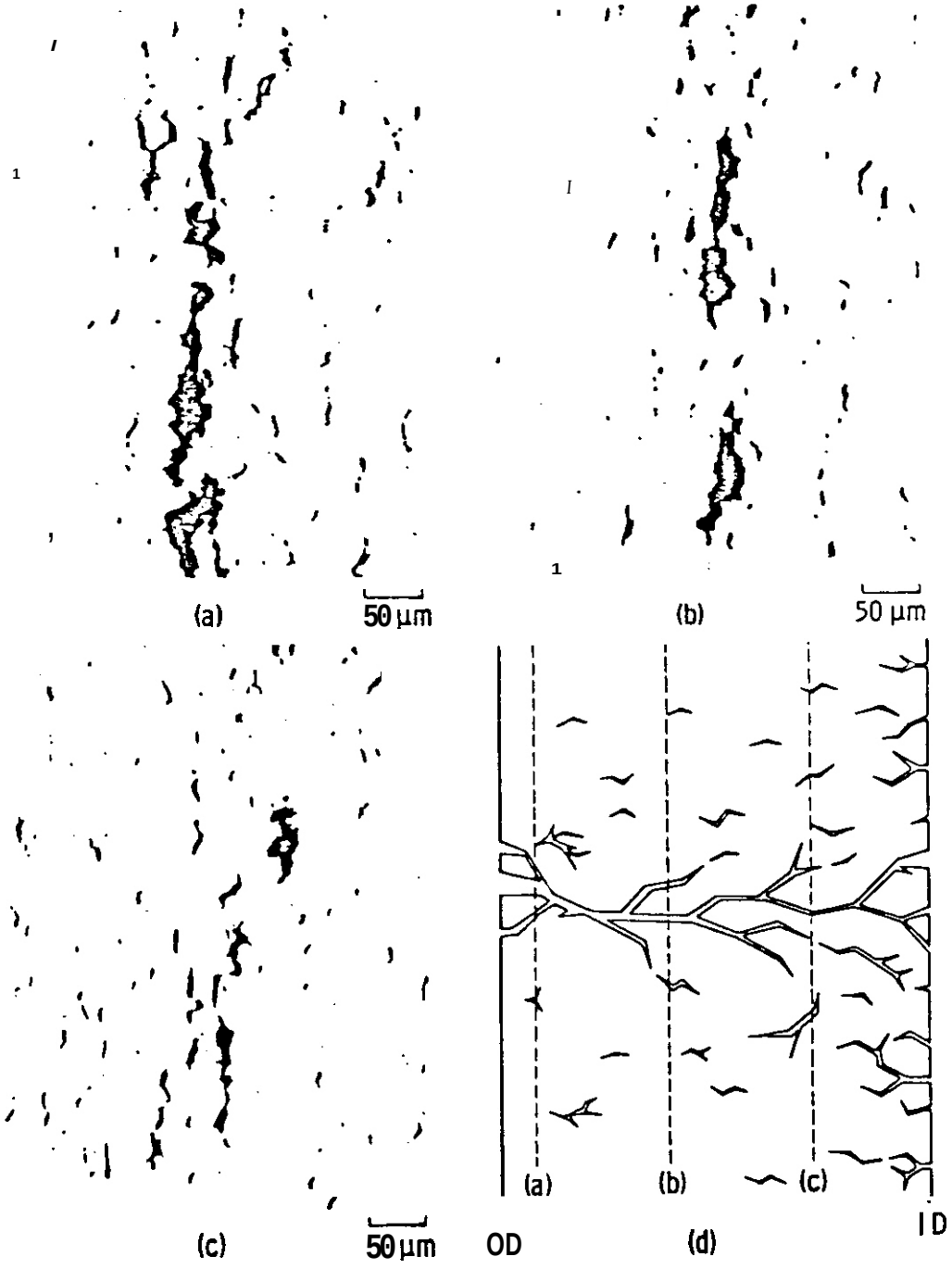

FIGURE 2. **Optical Metallography Following a** Through-Wall-Crack/Through-**Stress-Rupture Specimen** S-23(a-c) ; **Schematic Illustrating the Cracking Path Through the Thin Wall Tube** (d).

equations 3 and 4 and setting the stress equal to the yield strength. This simplification allows a single value of Y to be used for varying crack lengths in equation 2. For a yield strength of 200 MPa and Youngs mdulus of 2 x 10^5 MPa, δ/a is equal to 0.00185. For the case where time dependent flow occurs, δ/a is time dependent and could assume values greater than 0.00185 and less than or equal to 1. In order to simplify the calculations, a constant value of 0.2 was chosen for δ/a for the case when creep allows the crack to open beyond the fracture mechanics criteria. The value of 0.2 was chosen because this was the approximate value found for intergranular creep cracks formed in 316 SS tubes[4]. Worden[6] gives values of Y for δ/a values of 1 to 0.1 and this data was used to extrapolate to δ/a values of 0.001. The data for Y versus δ/a[6] is shown plotted in figure 3 where it can be seen that the relationship is linear on a log-log plot for values of δ/a of 0.1 to 0.4. This data was used to obtain a value for Y at δ/a equal to 0.00185. This requires an extrapolation over two orders of magnitude into a δ/a regime which has not been measured experimentally. Therefore, the value of Y for a/a equal to 0.00185 must be considered as an estimate. For δ/a equal to 0.00185, Y is equal to 0.008 while for δ/a equal to 0.2, Y is equal to 0.4.

Helium leak rates for δ/a values of 0.00185 and 0.2 are given in figure 4 as a function of the crack length a. The leak rate is linear with the crack length on a log-log plot with a slope of 4 which results in a leak rate of helium, N_{He}, proportional to a^4. Therefore, small increases in the crack length can result in large increases in N_{He}. Since Y is proportional to $(\delta/a)^{0.83}$, the leak rate, $\dot{N}_{He}$, is proportional to $\delta^{2.8}$ and; therefore, small increases in the crack opening, δ, can also produce large increases in N_{He}. This can be seen by noting the change in N_{He} at constant crack length for δ/a values of 0.00185 and 0.2. For a crack length of 0.1 cm the leak rate increases from 3 x 10^{-8} moles/s to 3 x 10^{-2} moles/s for δ/a values of 0.00185 and 0.2, respectively. Therefore, it can be seen that creep processes can have a very large effect on the critical leak rate flaw size. This effect can also be shown for a critical leak rate of 10^{-3} moles/s where the critical leak rate flaw size is 1.25 cm in the absence of creep crack opening and 0.045 cm when creep results in a δ/a ratio of 0.2.

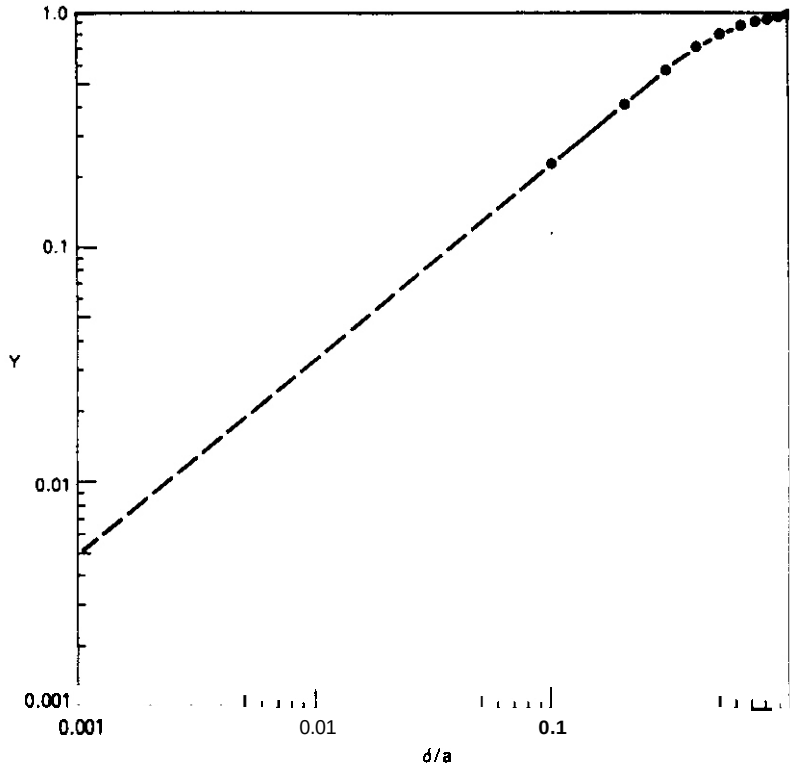

FIGURE 3. Relationship Between the Crack Opening to Length Ratio, δ/a, and the Parameter Y in the Leak Rate Equation.

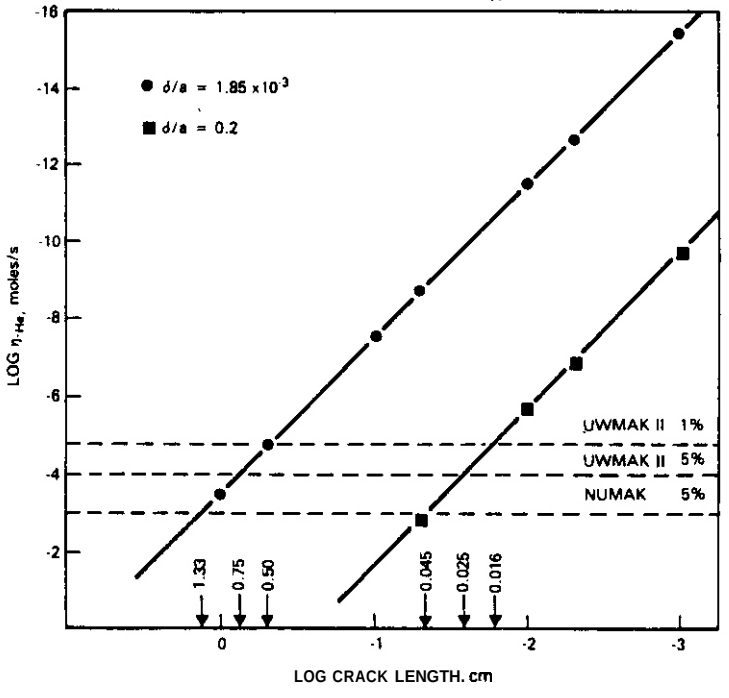

FIGURE 4. Crack Length, a, Versus Helium Leak Rate for δ/a Ratios of 1.85×10^{-3} and 0.2.

A critical leak rate for a given reactor can be estimated from the plasma volume, the ion density in the plasma and the largest helium concentration that the plasma can tolerate. It has been assumed that there is no plasma impurity control and that any shortening of the burn cycle is detrimental. These assumptions represent a worst case since plasma impurity control measures would allow larger leak rates before the critical helium concentration would be reached in a single burn cycle. It has also been assumed that all the helium in the plasma is removed during each refueling cycle. This of course will not occur since helium coolant will continue to leak into the plasma chamber during the refueling cycle. However, since the refueling time is short relative to the burn period, the helium in-leakage would be small and may be ignored without causing serious error.

The critical leak rate flaw size has been estimated for the UWMAK II and the NUMAK reactors assuming the NUMAK has a helium cooling system similar to UWMAK II. The UWMAK II has 5×10^{21} ions and the NUMAK 5×10^{22} ions in the plasma. For a 1000s burn period and a critical helium concentration in the plasma of 5% the critical leak rates are 10^{-4} moles/s, and 10^{-3} moles/s for the UWMAK II and NUMAK reactors, respectively. These leak rates correspond to critical flaws sizes of 1.33 cm and 0.75 cm for the NUMAK and UWMAK II reactors, respectively, in the absence of creep crack opening and 0.045 cm and 0.025 cm with creep crack opening. For a critical helium concentration of 1% the critical leak rate is 8×10^{-4} moles/s for the UWMAK II reactor. This leak rate corresponds to critical leak rate flaw sizes of 0.50 cm and 0.016 cm for the UWMAK II reactor, in the absence of creep crack opening and in the presence of creep crack opening, respectively.

5.4 Sub-critical and Critical Crack Growth Flaws

5.4.1 Austenitic Stainless Steels

Sub-critical flaw growth can occur in materials loaded statically in the presence of hydrogen or a corrosive environment or loaded cyclically in the absence or presence of hydrogen or a corrosive environment. In many

instances, the lowest stress intensity for sub-critical flaw growth occurs with cyclic stresses in a corrosive environment which is commonly known as corrosion fatigue.

Flaw sizes for sub-critical and critical crack growth of austenitic stainless steels are given in Table I[8-10]. The critical flaw sizes were calculated using equation 1 and assuming a macroscopic stress equal to the yield strength of the material. Therefore, the assumed stress was 550 MPa for 20% CW 316 SS and 200 MPa for annealed 304 SS. Corrosion fatigue and stress corrosion data for annealed 304 SS was used to estimate flaw sizes for sub-critical crack growth of austenitic stainless steels because of the lack of this type of data for 316 SS.

The following conclusions can be made regarding critical flaws in austenitic stainless steels: 1) a helium cooled reactor will be shut-down because of a critical leak before a large break in the first wall and 2) fatigue stresses will cause sub-critical flaw growth at lower stresses or for shorter flaws than static stresses. Fatigue or corrosion fatigue will cause growth of sub-critical flaws to a size where they become a critical leak rate flaw while static stresses require flaws that are larger than the critical leak rate flaw size. This comparison demonstrates the desirability of a steady state fusion reactor which minimizes cyclic stresses in the blanket and first wall material over a pulsed fusion reactor in which the stresses and temperatures will cycle.

The flaw size comparison given in Table I is useful for showing the kind of test data needed to evaluate materials for fusion reactors. A list of test data needed to evaluate austenitic stainless steels for fusion reactor applications is listed below along with the reason this data is needed:

- fracture toughness of 316 SS (25°C-450°C) irradiated at the fusion He/dpa: helium is known to embrittle 316 SS and will therefore reduce the critical flaw size. Welded test samples should be included in this series.

TABLE I CRITICAL FLAW SIZES IN AUSTENITIC STAINLESS STEELS

Failure Criterion	Conditions	Stress MPa	Stress Intensity MPa$\sqrt{m}$	Critical Flaw Size, mm	Ref.
Coolamt Leak Rate	Helium coolant leakage into plasma chamber during 1000s burn	---	---	1% H_2O 16 5% H_2O 25	---
Unstable Flaw Growth	[illegible] 400°C Unirradiated	[illegible]	110	10	3
	Irradiated, 10^{25} cm^{-2} fast neutrons, 400°C	550	70	4	3
Fatigue Crack Growth	20% CW, 316 SS Unirradiated 550°C, vacuum	550	12	0.1	8
Corrosion Fatigue Crack Growth	[illegible] Unirradiated, 95°C, Argon	200	1	0.8	8
	Sensitized 304 SS 95°C, H_2O/1.5 ppm O_2	200	[illegible]	[illegible]	[illegible]
Stress Corrosion Crack Growth	[illegible] 95°C, H_2O/1.5 ppm O_2	200	15	1.4	9
	Sensitized 304 SS 228°C, H_2O/1.0 ppm O_2	200	17	1 8	10

- fatigue and/or corrosion fatigue (300-500°C) of 316 SS irradiated at the fusion He/dpa: this test and material condition will probably define the smallest critical flaw size. Welded test samples should be included in this series.

Other tests which are not listed but may prove to be important include in-reactor corrosion fatigue to check for effects of grain boundary impurity segregation or radiolysis on corrosion fatigue or stress corrosion.

5.4.2 Ferritic Stainless Steels

Flaw sizes for sub-critical and critical crack growth of ferritic stainless steels are given in Table II[11-14]. The critical flaw sizes were calculated using equation 1 and assuming a macroscopic stress equal to the yield strength. A yield strength of 450 MPa was taken for HT-9 except for the hydrogen embrittlement evaluation where the results[13] of as-quenched material were used to give a better indication of hydrogen embrittlement in irradiation hardened material. Since the hydrogen embrittlement data for as-quenched HT-9 was from tensile data and not fracture toughness data, the critical flaw size was estimated from a calculated value for K_{IC} using the following equation:

$$K_{IC} = C\ (E\ \sigma y\ \ell\ \epsilon_f)^{1/2} \qquad (6)$$

expressed by Hahn and Rosenfield[15] where C is a constant, E is the Young modulus, σ_Y is the yield strength, ℓ is a characteristic distance ahead of the crack tip and ϵ_f is the strain to failure. A value for K_{IC} for hydrogen charged, irradiation hardened HT-9 was estimated from the following data, equation 6 and assuming that C and ℓ are equal for the quenched and hydrogen charged and quenched and tempered conditions:

	QUENCHED AND TEMPERED NO HYDROGEN	QUENCHED HYDROGEN CHG'D
K_{IC}, MPa$\sqrt{m}$	120	75 (calc.)
$a_{Y'}$ MPa	650	1225
ϵ_f	0.17	0.036

TABLE II CRITICAL FLAW SIZES IN FERRITIC STAINLESS STEELS

Failure Criterion	Conditions	Stress MPa	Critical Stress Intensity MPa $\sqrt{m}$	Critical Flaw Size, mm	Ref.
Coolant Leak Rate	Helium coolant leakage into plasma chamber during 1000s burn	---	---	1% He:0.16 5% He:0.25	--
Unstable Flaw Growth	HT-9 Unirradiated 427°C	450	275	95	11
	HT-9 Irradiated 10^{22} cm^{-2}, 427°C	450	200	50	11
	1% Cr Steel, Temper embrittled 25°C	≤50	40	1	12
	HT-9, Hydrogen embrittled, ≥5 C	650	≥5	3 (calc)	13
Fatigue Crack	HT-9, Unirradiated	450	8	0.1	14
Stress Corrosion Crack Growth	12 Cr steel, 25 C Water	650	20	0.2	12

Ferritic stainless steels show similar trends to austenitic stainless steels in that fatigue stresses produce sub-critical crack growth with the smallest flaw size. Ferritic stainless steels appear to be more sensitive to stress corrosion than austenitic stainless steels where the critical flaw size for sub-critical crack growth in water at 25°C is 0.2 mm. Ferritic stainless steels can be embrittled by grain boundary impurity segregation (temper embrittlement) resulting in a critical flaw size of 1 mm in a 12 Cr steel at 25°C. The temper embrittlement, hydrogen embrittlement and stress corrosion cracking of ferritic steels at reactor service temperatures will presumably be greater than at 25°C unless the ductile to brittle transition temperature, DBTT, is shifted to the reactor service temperature by radiation hardening and helium. Smidt[11] has measured the fracture properties of HT-9 irradiated to 10^{22} cm^{-2} and his results indicate that the critical flaw size was reduced from 95 mm to 50 mm. It is possible that the critical flaw size of HT-9 irradiated to higher fluences at a fusion He/dpa will be less than 50 mm; however, this data is not presently available.

The data in Table II indicates the need for more data which is relevant to the fusion reactor environment. A list of test data needed to evaluate ferritic stainless steels for fusion reactor applications is listed below along with the reason this data is needed:

- o fracture toughness (25°C-450°C) of HT-9 irradiated to fluences of $>10^{23}$ cm^{-2} at fusion He/dpa: radiation hardening and helium will raise the DBTT and decrease the upper shelf fracture toughness.
- o fatigue, stress corrosion or corrosion fatigue tests (300-500°C) of HT-9 irradiated to fluences of $>10^{23}$ cm^{-2} at a fusion He/dpa: fatigue, stress corrosion and corrosion fatigue tests of irradiated material will define the smallest critical flaw size.
- fatigue, stress corrosion or corrosion fatigue tests (300-500°C) of temper embrittled and irradiated HT-9: HT-9 which was temper embrittled by improper thermal-mechanical treatment (such as during

welding, heat treatment or fabrication) prior to irradiation could conceivably produce the smallest critical flaw size and would therefore represent the worst case.

As in austenitic stainless steels, the critical helium leak rate flaw size is similar in size to that for sub-critical crack growth during fatigue and less than the critical flaw size for unstable flaw growth. However, the flaw size for unstable flaw growth of temper embrittled HT-9 is only 5x greater than a critical leak rate flaw size while the smallest flaw size for unstable flaw growth of austenitic stainless steel was 20x greater than the critical leak rate flaw size. Therefore, the transition between leak before break in ferritic stainless steels may be less than for austenitic stainless steels. This situation changes if temper embrittlement does not occur in ferritic stainless steels and if irradiation to fluences greater than 10^{22} cm^{-2} does not significantly decrease the critical flaw size for unstable flaw growth.

6.0 References

1. B. Cramer et al. Fusion Reactor First Wall/Blanket Systems Analysis, Interim Report, MDAC/EPRI 472-1, Oct. 1977.

2. R. D. Watson, R. R. Peterson and W. G. Wolfer, "The Effect of Irradiation Creep, Swelling, Wall Erosion and Embrittlement on the Fatique Life of a Tokamak First Wall" in Proceedings of the Second Meeting on Fusion Reactor Materials, Aug. 1981.

3. W. G. Wolfer and R. H. Jones, "Flow and Fracture in the Fusion Environment" in the Proceedings of the Second Meeting on Fusion Reactor Materials," Aug. 1981.

4. R. H. Jones and S. M. Bruemmer, Damage Analysis and Fundamental Studies Quarterly Report for Oct.-Dec. 1980, DOE/ER-0046/4, p. 65.

5. Wisconsin Tokamak Reactor Design, UWMAK II, UWFDM-68, May 1975, University of Wisconsin, Madison, Wisconsin.

6. D. G. Worden, "Flow of Gases Through Tubes and Orifices" in Scientific Foundations of Vacuum Technology, F. Dushman and J. M. Lafferty, J. Wiley & Sons, New York, 1962, p. 80.

7. J. F. Knott, "Fundamentals of Fracture Mechanics," 1979, Halsted Press, New York, p. 89.

8. D. J. Michel and H. H. Smith, "Environmental Effects on Elevated Temperature Fatigue Crack Propagation in Type 316 SS for Fusion Reactor Applications," in Environmental Degradation of Engineering Materials, Virginia Polytechnic Institute, Sept. 1981, p. 313.

9. F. P. Ford and M. Silverman, Corrosion, Vol. 36, No. 11, (1980), p. 597.

10. R. D. Caligiuri, "Low Temperature Sensitization of Weld Heat Affected Zones in 304 SS," in proceedings of EPRI International Workshop on Low Temperature Sensitization, Paper No. 4.

11. F. A. Smidt, J. Hawthorne, and V. Provenzano, Alloy Development for Irradiation Performance, Quarterly Report, DOE/ER-0045/2, p. 163.

12. M. O. Speidel, "Corrosion Fatigue in Fe-Cr--Ni Alloys," in Stress Corrosion Cracking and Hydrogen Embrittlement of Iron Base Alloys, Conference held at Unieux-Firminy, France, June 1973, R. W. Staehle, J. Hochmann, R. D. McCright and J. E. Slater, eds., NACE-5, p. 1071.

13. J. M. Hyzak and R. E. Stoltz, Alloy Development of Irradiation Performance Quarterly Report, DOE/ER-0045/3, p. 180.

14. D. A. Mervyn, Alloy Development for Irradiation Performance Quarterly Report, DOE/ER-0045/3, p. 226.

15. G. T. Hahn and A. R. Rosenfield, in Applications Related Phenomena in Titanium Alloys, ASTM STP 432 (1968) 5.

7.0 Future Work

Threshold flaw sizes for static and cyclic stresses will be measured for unirradiated 316 SS and HT-9 in aqueous solutions. Measurements will be made at anodic and cathodic potentials to determine threshold flaw sizes for stress corrosion and hydrogen embrittlement processes. Also, samples heat treated to produce grain boundary impurity segregation will be tested to determine the effect of impurity segregation on threshold and critical flaw sizes in 316 SS and HT-9.

LOCAL DISPLACEMENT FIELDS IN IRRADIATED MATERIALS

J. L. Bennetch and W. A. Jesser (University of Virginia)

1.0 Objective

The objective of this work is to demonstrate a new HVEM method to map the displacement field about a crack tip in irradiated microtensile samples.

2.0 Summary

In microtensile samples irradiated to high doses, cavities form which can be used as internal markers. From measurements of the elongation or displacement of these markers, a displacement map of the strain field in front of crack tip can be constructed.

3.0 Program

Title: Simulating the CTR Environment in the HVEM
Principal Investigators: W. A. Jesser and R. A. Johnson
Affiliation: University of Virginia

4.0 Relevant DAFS Program Plan Task/Subtask

Task II.C.13 Effects of Helium and Displacements on Crack Initiation and Propagation

5.0 Accomplishments and Status

5.1 Introduction

In the theoretical analysis of the mechanical behavior of irradiated materials, the shape of the strain field in front of a crack tip is of considerable importance. In the past, experimentalists have usually measured localized

strain by first placing a grid on the surface of a tensile sample. The distortion of this grid after a tensile test would be related to the strain field. To increase the resolution of this method, a second reference grid or grating can be superimposed on the distorted first grid to produce Moiré patterns". However, the smallest increment of displacement which can be measured by the Moiré method is about 750 Å. To adequately check theoretical treatments of fracture behavior more precision is desireable. In addition, strain behavior in the interior of the sample is useful.

An alternative method was devised to plot strain field maps in irradiated materials using radiation induced cavities as markers. From transmission electron micrographs, one can construct a displacement map, related in turn to the strain field or the plastic zone, by first measuring the elongation of individual cavities or the relative displacements of pairs of cavities. This is accomplished by enclosing regions of equal displacement with isodisplacement contours. The smallest increment of displacement resolvable by the TEM method is only limited to the resolution of the electron microscope; in principle, displacements two orders of magnitude better than those found by the Moiré fringe method could be detected. Moreover, the TEM technique allows direct correlation of slip systems with crack propagation characteristics.

5.2 Experimental Procedure

A microtensile rectangular sample (2.5 mm x 12.5 mm) was punched out from a 40 μm thick sheet of solution annealed type 316 stainless steel. After the center had been electrothinned, the sample was then bombarded with 80-keV helium ions at ∿ 300" C to a total fluence ∿ 10^{18} ions/cm^2. Then, a post irradiation anneal at 900" C was performed in vacua, allowing the coalescence and growth of cavities for markers inside the irradiated material. Next, the specimen was pulled in a high voltage electron microscope (HVEM) at room temperature by means of a hydraulically operated single tilt tensile stage. Further details on experimental apparatus have been previously published in DAFS reports and elsewhere[2-5]. All measurements of cavities were performed di-

rectly from HVEM electron photographic plates.

5.3 Results and Discussion

5.3.1 Electron Beam Direction, E

One of the attractive features of this method of analysing local strain is the option of correlating slip systems directly with crack propagation characteristics. As a prelude to this correlation, an accurate determination of beam direction, B, must be obtained. However, this procedure is not always straightforward. For instance, the progression of a crack in helium irradiated 316 stainless steel was followed in-situ during tension in a thick portion of the foil (> 1 μm), as typified in Figure 1. Here is seen a crack approaching a grain boundary through a grain filled with large cavities. This portion of the foil was too thick for electron diffraction patterns to be produced in a 500 kV HVEM, so an indirect method was necessary to find B. Fortunately, two (111) type slip bands of different widths, w_1 and w_2, were visible in the micrograph, noticeable as light bands in Figure 1. Analysis of these widths shows that the normal of foil surface is very close to a $[\bar{1}22]$ direction.

5.3.2 Slip Systems

By knowing B and assuming the trace of the two (111) planes lay along $[01\bar{1}]$ directions, one could identify pertinent crystallographic directions and slip systems in the micrograph in Figure 1. Figure 2, a schematic of the micrograph in Figure 1, illustrates these features. Notice that the wide slip band corresponds to a (ill) plane while the two narrower bands correspond to a (111) plane. The light area roughly parallel to the crack flank extends along the $[\bar{4}1\bar{3}]$ direction, the direction of the trace of a steeply inclined $(11\bar{1})$ slip plane. Finally, the tensile axis is apparently parallel to the $[22\bar{1}]$ direction in the central grain.

Not all of these planes are active in the slip process, however, as can be

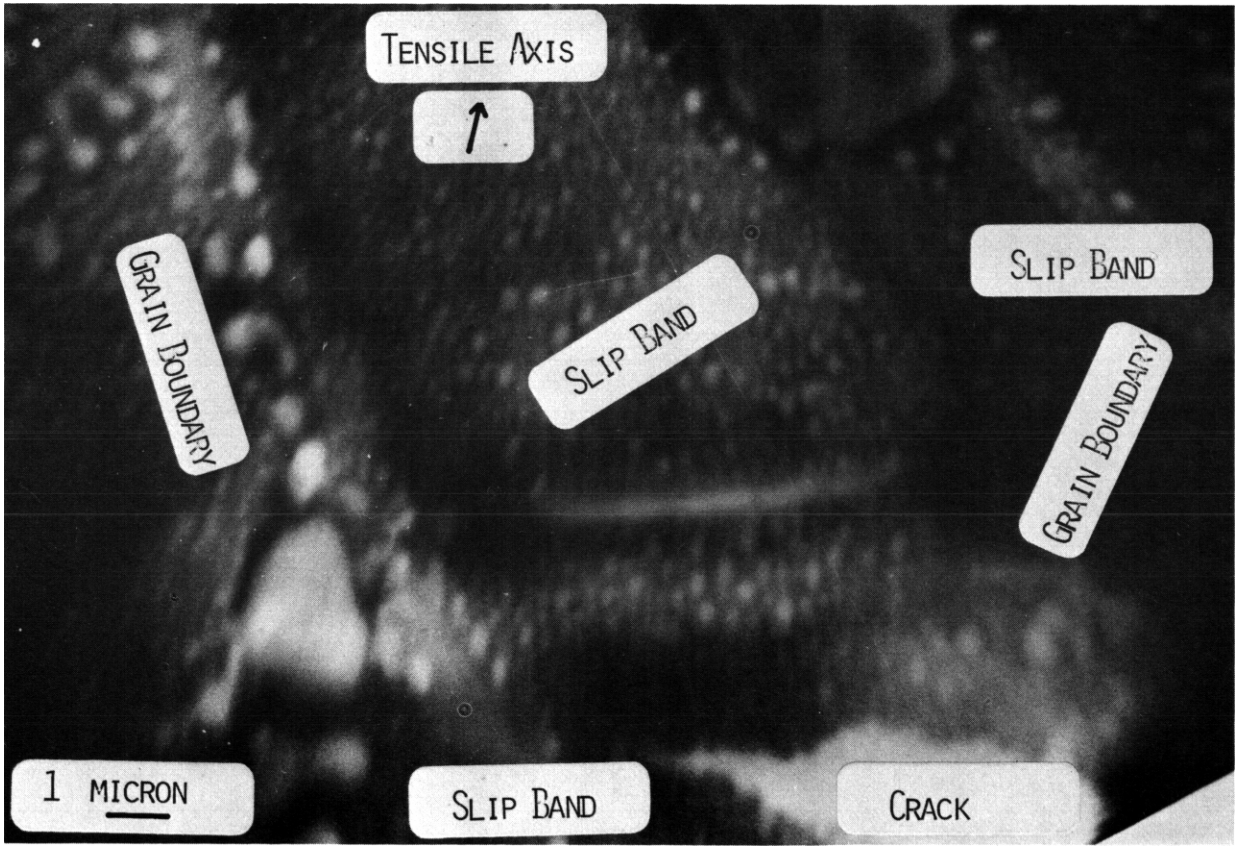

Figure 1 HVEM micrograph of crack propagating through helium irradiated 316 stainless steel

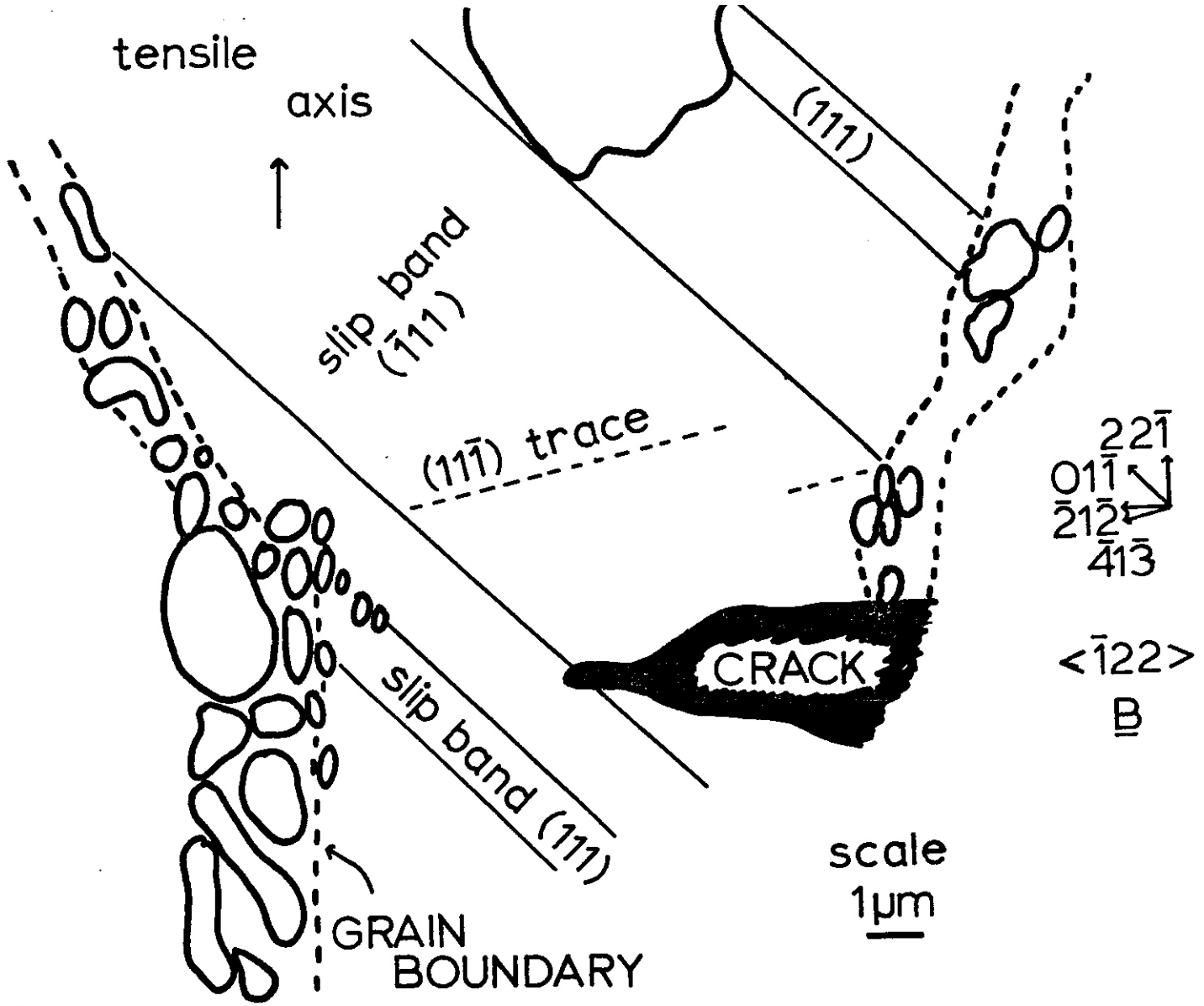

Figure 2. Schematic of micrograph in Figure 1 identifying slip bands and pertinent crystallographic directions.

seen by an examination of the Schmid factors. Table 1, a listing of the slip systems for a $[22\bar{1}]$ tensile axis, shows four slip systems with large positive Schmid factors: $(111)[10\bar{1}]$, $(111)[01\bar{1}]$, $(11\bar{1})[011]$ and $(11\bar{1})[101]$. Subsequent micrographs verified this analysis, showing that the crack advanced along $[\bar{2}1\bar{2}]$ until it reached the forward (111) slip band. Then it turned upward, advancing diagonally on that plane along the $[01\bar{1}]$ direction. Simultaneously, holes parallel to the main crack flanks opened up along the $(11\bar{1})$ planes. Then the crack switched directions again, crossing the grain boundary along the $[\bar{4}1\bar{3}]$ direction - the trace of the $(11\bar{1})$ plane.

Other interesting observations can be made concerning the slip process in this sample. First, a careful examination of Figure 1 shows that the cavities elongated only in the direction of the tensile axis. Next, elongation of the cavities in this direction can be accounted for by a linear combination of slip dislocations on the active (111) and $(11\bar{1})$ planes, as seen by the following vector addition equation: $2\frac{a}{2}[10\bar{1}] + 2\frac{a}{2}[01\bar{1}] + \frac{a}{2}[011] + \frac{a}{2}[101] = a[33\bar{2}]$. The addition of these Burgers vectors, weighted approximately according to their Schmid factors, yields a direction less than 6" from the tensile axis which is in the plane of the specimen.

5.3.3 Displacement Hap

A displacement map (related to the plastic zone or strain field) in front of a crack tip was constructed from Figure 1, by use of the abovementioned techniques. Illustrated in Figure 3, the map shows three distinct strained regions, one immediately in front of the crack tip, a large asymmetric region roughly parallel to the crack flanks and another smaller region in the next grain adjacent to the grain boundary. Within each of the three regions are areas of larger displacement, indicating higher localized strain or greater local thinning of the foil had taken place there. Either the main crack itself propagated directly through these thinned regions or first holes opened up in front of (or parallel to) the crack at these sites, as shown in subsequent micrographs. Moreover, the outline of the regions of highest dis-

TABLE 1

SUMMARY OF POSSIBLE SLIP SYSTEMS FOR A $[22\bar{1}]$ TENSILE AXIS

tensile axis	slip plane	slip direction	Schmid factor	
$[22\bar{1}]$	(111)	$[1\bar{1}0]$	0.900	
		$[10\bar{1}]$	+0.408	operative
		$[01\bar{1}]$	+0.408	operative
	$(\bar{1}11)$	$[01\bar{1}]$	-0.136	
		$[101]$	-0.045	
		$[110]$	-0.181	
	$(11\bar{1})$	$[011]$	+0.227	operative
		$[101]$	+0.227	operative
		$[1\bar{1}0]$	0.000	
	$(1\bar{1}1)$	$[10\bar{1}]$	-0.136	
		$[110]$	-0.181	
		$[011]$	-0.045	

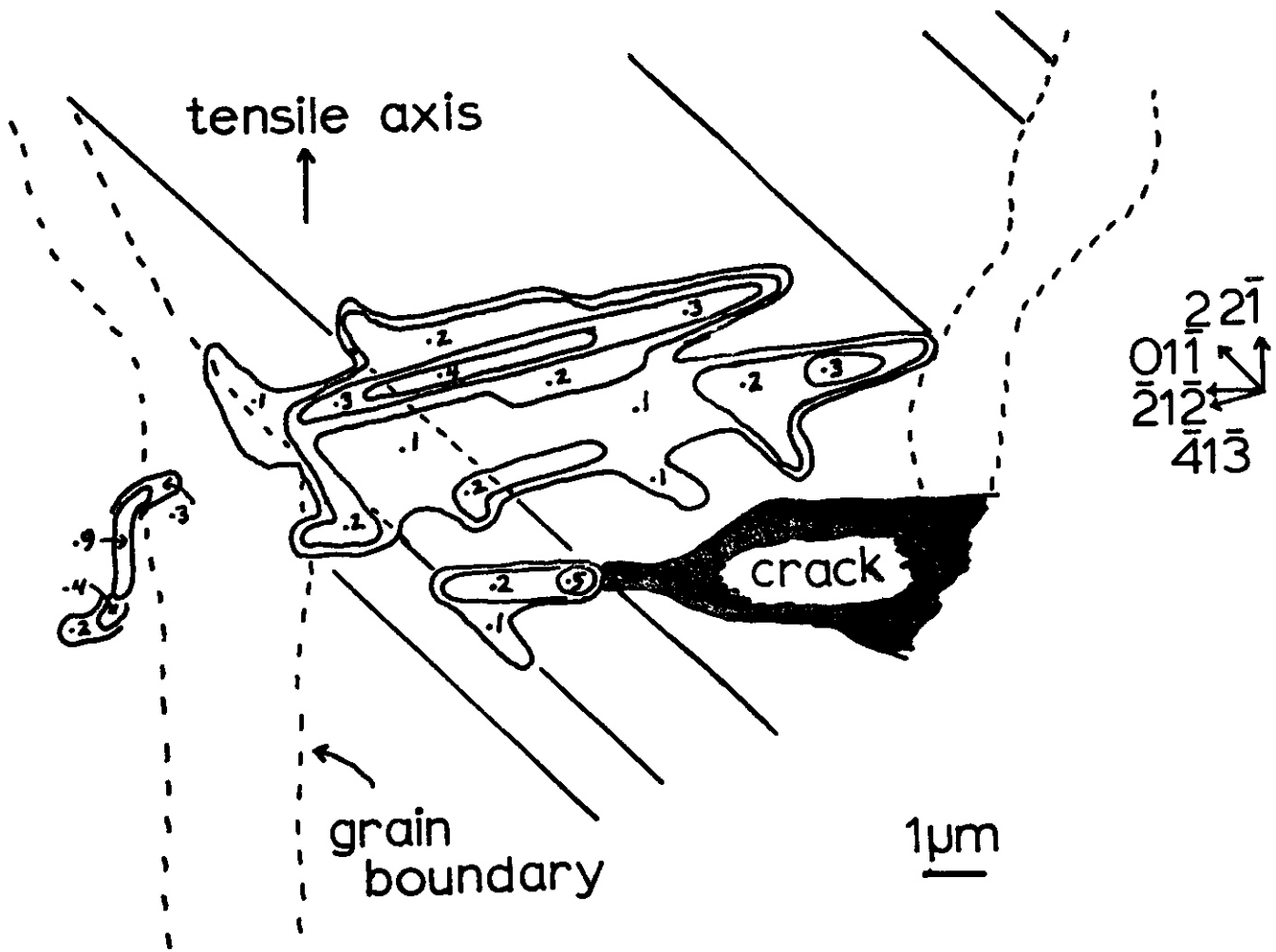

Figure 3 Displacement map generated from Figure 1 The isodisplacement contours are labelled in microns

placement seemed to roughly parallel the $[01\bar{1}]$ and $[\bar{4}1\bar{3}]$ directions, which are the directions of the traces of the two most active slip planes, (111) and $(11\bar{1})$. This suggests at least in plane stress situations such as are likely encountered in thin foils that the details of the shape of the plastic zone about the crack tip depend on the relative orientation of the active slip systems.

Theoretical predictions of the shape of the plastic zone by Irwin[6] suggest that there should be another equally shaped plastic zone located symmetrically on the lower side of a crack. Hahn and Rosenfield[7] have experimentally verified a two lobe plastic zone shape by way of etch pit studies in an iron-silicon alloy. The absence of such a zone in Figure 1 may be the result of an asymmetry in the tensile system.

For a situation of plane stress (a state of stress approximately true for thin foils), the size of the plastic zone r_Y can be estimated from stress-field equations. In that case, one gets the following equation, assuming the normal component of the stress is set equal to the yield strength, σ_{ys}[8].

$r_Y = \frac{1}{2\pi}(\frac{K}{\sigma_{ys}})^2$ where K = stress-intensity factor. For instance, for a bulk type 4340 steel, r_Y is calculated to be 0.25-2.0 mm for plane stress[9] while from Figure 3, r_Y is 2-4 μm, 2 to 3 orders of magnitude smaller. Radiation damage can reduce K by a factor of 4-5[10] while simultaneously increasing σ_{ys}. However, in unirradiated HVEM microtensile samples, it has been found that r_Y is of the same order of magnitude as the r_Y derived in Figure 3. At this time, it is not clear how to relate stress intensity measurements derived from HVEM microtensile samples to bulk values.

5.4 Conclusions

1. Bubbles elongated parallel to the tensile axis and foil plane.

2. The shape of the plastic zone is dependent upon the orientation of the act-

ive slip systems relative to the crack direction and tensile axis

3. Holes opened up in front of the crack tip, and the crack itself propagated through, regions of large localized strain.

6.0 References

1. P. S. Theocaris, Moiré Fringes in Strain Analysis (Pergamon Press, New York, 1969), 67.

2. W. A. Jesser, J. A. Horton, and L. L. Scribner, "Adaption of an Ion Accelerator to a High Voltage Electron Microscope," Radiation Effects, 29 (1976), 79.

3. J. W. Bennetch, J. A. Horton, and W. A. Jesser, "Ion Accelerator-HVEM Link" in Proceedings of the 35th Annual EMSA Meeting, ed. by G. W. Bailey (Claitor's Publishing Co., Baton Rouge, Louisiana, 1977), 96.

4. W. A. Jesser, J. A. Horton, J. W. Bennetch, L. L. Scribner, and H. G. F. Wilsdorf. "Instrumentation for SAMI Studies," ed. by R. M. Fisher and T. Imura, in Proceedings of the US-Japan HVEM Seminar:" New Applications and Extensions of the Unique Advantages of the HVEM for Physical and Materials Research (Nagoya University, Nagoya, Japan, 1977), 30.

5. W. A. Jesser, "Light Ion Accelerator-High Voltage Electron Microscope Facility for CTR Radiation Damage Studies," 1978 Conference on the Applications of Small Accelerators in Research and Industry, North Texas State University, Denton, Texas (Nov. 6-8, 1978), IEEE Transactions on Nuclear Science NS-26 (1979), 1252.

6. G. R. Irwin, "Analysis of Stresses and Strains Near the End of a Crack Traversing a Plate," Transactions, ASME, Journal of Applied Mechanics, 24 (1957)

7. G. T. Hahn and A. R. Rosenfield, "Local Yielding and Extension of a Crack Under Plane Stress," Acta Metallurgica, 13 (1965) 293.

8. G. R. Irwin, "Plastic Zone Near A Crack and Fracture Toughness," 1960 Sagamore Ordnance Materials Conference, Syracuse University, 1961

9. R. W. Hertzberg, Deformation and Fracture Mechanics of Engineering Materials (John Wiley and Sons, New York, 1976), 285.

10. S. H. Bush, "Structural Materials for Nuclear Power Plants," Journal of Testing and Evaluation, 2 (1974), 435.

CHAPTER 4

CORRELATION METHODOLOGY

ON THE CORRELATION OF YIELD STRENGTH CHANGES IN 316 STAINLESS STEEL IRRADIATED WITH HIGH ENERGY AND FISSION REACTOR NEUTRONS

H. L. Heinisch and R. L. Simons (Hanford Engineering Development Laboratory)

1.0 Objective

The objective of this work is to develop correlation methods for irradiation effects on tensile properties of materials important to magnetic fusion energy devices.

2.0 Summary

Data on change in yield strength of SA 316 stainless steel irradiated with 14-MeV, Be(d,n) and fission reactor neutrons do not correlate with respect to damage energy. The data suggest possible temperature on additional spectral effects. A simple defect production function, based on the production of lobes in computer simulated cascades, correlates the data much better than damage energy.

3.0 Program

Title: Irradiation Effects Analysis (AKJ)
Principal Investigator: D. G. Doran
Affiliation: Hanford Engineering Development Laboratory

4.0 Relevant DAFS Program Plan Task/Subtask

Subtask II.B.1.6 Calculation of Defect Production Cross Sections
Subtask II.C.16.1 Correlation Model Development

5.0 Accomplishments and Status

The testing of irradiation effects on material properties in potential fusion reactor materials using non-fusion sources of radiation requires that a correlation of the effects expected in the fusion environment and the test environment

be known. The primary effect of neutron radiation is the production of displacement damage. Understanding and accounting for any differences in the way displacement damage is produced in different radiation environments is thus extremely important.

Experiments conducted by Vandervoort, et al.[1] determined the increase in yield strength (ΔYS) of solution annealed 316 stainless steel irradiated with 14 MeV neutrons, Be(d,n) produced neutrons and fission reactor neutrons. One result of that investigation was a comparison of the increase in yield strength as a function of damage energy for the three neutron spectra. Acknowledging that there were some systematic differences between the 14 MeV and fission data, Vandervoort, et al. nevertheless concluded that damage energy is an effective parameter for correlation of the yield strength changes. A close examination of this data, replotted in Figure 1, reveals that the fission data are distinctly different from the 14-MeV and Be(d,n) data. In fact, to make the two sets of data points coalesce requires an adjustment of the damage energy by a factor of ~1.75. Hence, damage energy is apparently not an accurate parameter for correlation of this data.

It should be roted that the irradiation temperature in the fission reactor was 65°C, whereas the other irradiations occurred at 25°C. It is possible that the apparent correlation inadequacy of the damage energy is, at least in part, a temperature effect. The question of the effect of irradiation temperature should be resolved by experiments in progress by Westinghouse Hanford Company which include irradiations of solution annealed 316 stainless steel at carefully controlled temperatures in RTNS-II and the Omega West Reactor.

It *is* also possible that the lack of correlation with respect to damage energy reveals an additional neutron spectral effect. The high energy neutrons (~14 MeV) of the Be(d,n) and T(d,n) reactions produce most of their displacement damage in the form of high energy cascades having hundreds of keV of damage energy, whereas the fission reactor neutrons produce most displacement damage in cascades having tens of keV of damage energy. It is not unreasonable to consider that a minimum cascade energy is required to produce the defects that cause hardening.

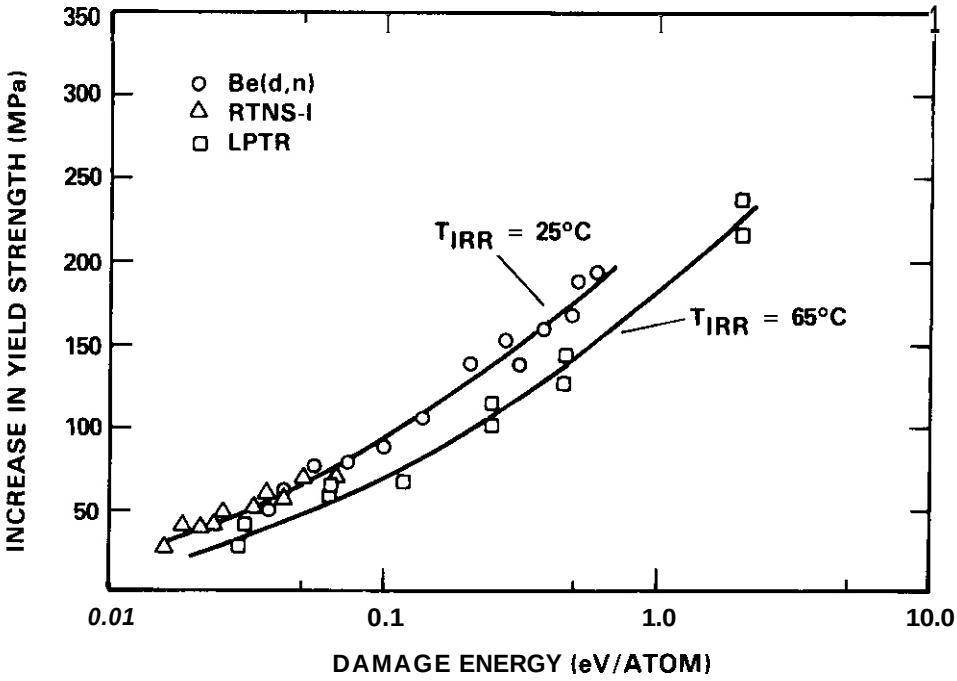

FIGURE 1. Increase in Yield Strength for SA 316 Stainless Steel Irradiated in Various Neutron Environments Plotted as a Function of Damage Energy. This is a replotting of Figure 2 of Vandervoort, et al.(1)

Vandervoort et al. also measured the sizes and density of the clusters visible in an electron microscope for several specimens. The majority of cluster diameters were reported to range from 10 to 20 nm. Assuming spherically shaped inclusions of equal radii acting as obstacles in the slip plane, the ΔYS can be related to the microstructure by the relations $\Delta YS \propto \sqrt{Nd}$, where N is the cluster density and d is the cluster diameter.[3] Assuming the average cluster size is the same in all the specimens, we compared ΔYS with $\sqrt{N}$, as shown in Figure 2. The ΔYS is linearly related to $\sqrt{N}$, and the data from the three irradiation environments are well correlated. To gain insight into how the cluster density may be related to the neutron spectrum, we turned to results from computer simulations of displacement cascades.

Recent analysis of computer simulations of displacement cascades[2] revealed that the high energy cascade structure consists of a grouping of distinct damage regions, which were called "lobes." The number of lobes was found to increase

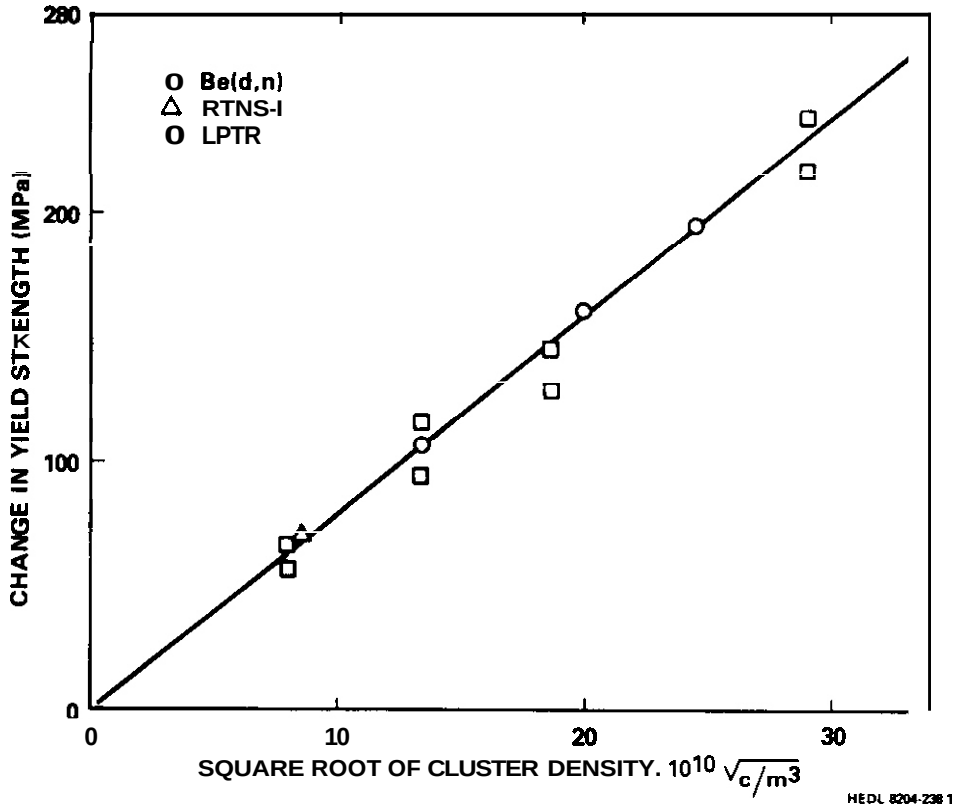

FIGURE 2. Increase in Yield Strength of SA 316 Stainless Steel as a Function of the Observable Cluster Density Measured by Vandervoort, et al.(1)

approximately linearly with energy above 20 keV. At energies between 10 and 20 keV, cascades undergo a transition from essentially single damage region production to multiple damage regions (lobes). The sizes of single damage regions increase with energy, and there is an indication that, on the average, a minimum-sized damage region must be produced before additional lobe production occurs.

The relationship between cascade structure and yield strength changes was tested by constructing a lobe production function, folding it into the primary recoil spectra, and plotting the yield strength change versus lobe production. The lobe production function we used is simply the linear relationship between the number of lobes and the cascade damage energy obtained from the computer simulations.[2] The function was given a threshold for production of "effective damage regions" at 12 keV, which is in the energy range of the onset of production of lobed cascade structures (i.e., more than one distinct damage region). The

yield strength data of Vandervoort, et al. are plotted as a function of cascade lobe production in Figure 3. The data appear to be better correlated by this simple lobe production function than by the damage energy.

The changes in yield strength of SA 316 stainless steel irradiated with 14 MeV, Be(d,n) and fission reactor neutrons are not correlated well on the basis of damage energy, but they appear to be correlated better on the basis of the microstructure, as observed from both electron microscopy and cnmputer simulations. The success of the cascade lobe production function, determined from computer simulations, demonstrates that cascade effects may play an important role in correlating changes in mechanical properties obtained in different irradiation environments.

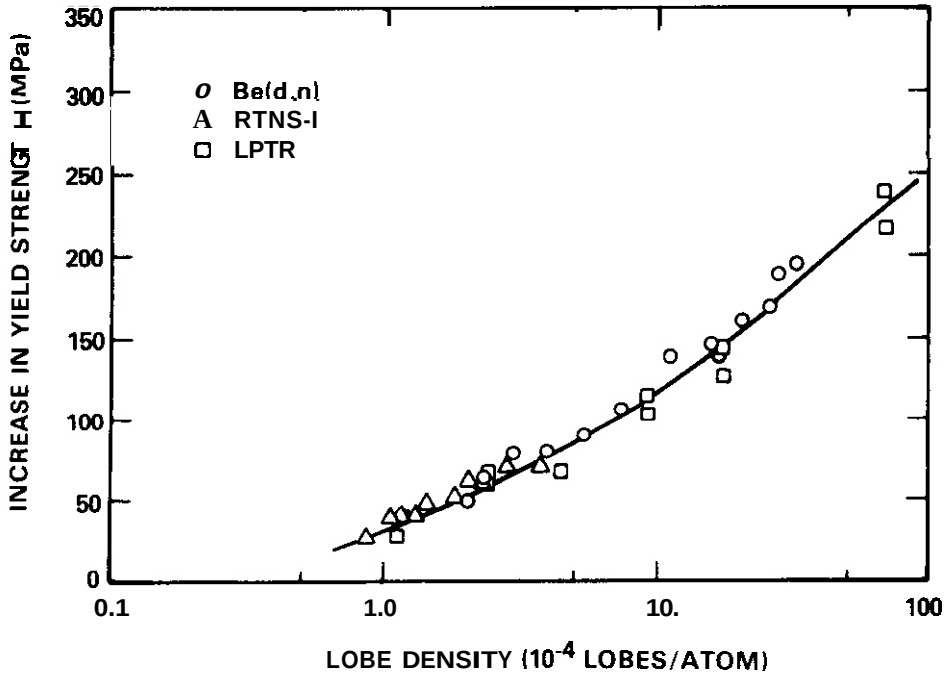

FIGURE 3. Increase in Yield Strength of SA 316 Stainless Steel as a Function of Cascade Lobe Density.

6.0 References

1. R. R. Vandervoort, E. L. Raymond and C. J. Echer, Rad. Effects, 45 (1980) 191.

2. H. L. Heinisch, Proceedings of the Second Topical Meeting on Fusion Reactor Materials, Seattle, WA, August 9-12, 1981, also J. Nucl. Mater. (in press).

3. G. D. Johnson, F. A. Garner, H. R. Brager and R. L. Fish, Effects of Radiation on Materials: Tenth Conference, ASTM STP 725 (1981) 393.

7.0 Future Work

Analysis of experimental data and computer simulations will continue in an effort to develop a more detailed understanding of the spectral effects on yield strength. Temperature effects will be addressed in the forthcoming HEDL experiments.

THE INFLUENCE OF DISLOCATION DENSITY AND RADIATION ON CARBON ACTIVITY IN AISI 316

W. G. Wolfer and F. A. Garner* (University of Wisconsin, *Hanford Engineering Development Laboratory)

1.0 Objective

The objective of this effort is to identify the role of each major element in the microchemical evolution of AISI 316 and the dependence of that role on preirradiation treatment and parameters such as neutron energy and flux, temperature and stress.

2.0 *Summary*

The interaction of carbon and dislocations induced by cold-working of AISI 316 is not as large as previously estimated. It appears however that it still may be sufficient at low irradiation temperatures to prolong the transient regime of swelling. At higher temperatures other as-yet unidentified physical mechanisms are required to explain the effect of cold-work on swelling. A possible high temperature mechanism is advanced which is based on the stability of carbide nuclei in a rapidly evolving dislocation network.

3.0 Program

Title: Irradiation Effects Analysis (AKJ)
Principal Investigator: D. G. Doran
Affiliation: Hanford Engineering Development Laboratory

4.0 Relevant DAFS Program Plan Task/Subtask

Task II.C.2.4 Modeling

5.0 Accomplishments and Status

5.1 Introduction

In a previous analysis of the role of cold-work on the swelling behavior of AISI 316, it was postulated that carbon would be bound in the stress-field of dislocations. As a result, the apparent carbon solubility would be enhanced in a cold-worked steel relative to that in annealed material.[**]) This argument was advanced as a possible explanation of the role of cold-working in the reduction of the swelling of 300 series alloys. Although this argument is correct in principle, the enhancement of solubility with dislocation density appears to be much less than was calculated earlier.

It was assumed in the previous analysis that the solute distribution around a dislocation is given by

$$C(r,\phi) = C_o \exp (U/kT) , \qquad (1)$$

where C_o is the solubility in a stress-free lattice and

$$U(r,\phi) = A \sin \phi/r . \qquad (2)$$

Here, r is the distance from the dislocation core, ϕ the angle with respect to the glide plane, and

$$A = \frac{Gb}{3\pi} \left(\frac{1 + \nu}{1 - \nu}\right) V \qquad (3)$$

is the strength of the interaction of the interstitial carbon atom with the dislocation stress-field. The parameter A is expressed in terms of the shear modulus G, the Burger's Vector b, Poisson's ratio ν and the relaxation volume or partial molar volume V of the solute.

Close to the dislocation core, $C(r,\phi)$, as computed by Equation (1), will actually exceed an atom fraction of 1.0. Therefore, it was assumed previously, that

wherever $C \geq 1$, the actual carbon atom fraction is equal to 1.0. This corresponds however to a region of carbon saturation comprising a cylinder of about 25 Burger's vectors in diameter. If indeed that much carbon was trapped, precipitation of carbides would occur along the entire length of all dislocations.

The previous analysis should be modified, however, by replacing the Boltzmann statistics implied in Equation (1) with the correct Fermi-Dirac statistics, subject to the obvious condition that each interstitial site near the dislocation can be occupied by only one carbon atom.

5.2 Effect of Dislocation on Solute Solubility

According to Fermi-Dirac statistics, Equation (1) must be replaced by

$$\frac{C(r,\phi)}{1 - C(r,\phi)} = \frac{C_o}{1 - C_o} \exp (U/kT) \; . \tag{4}$$

Where both $C_o \ll 1$ and $U \ll kT$, then the Boltzmann statistics and Equation (1) become valid.

In order to obtain the average solute concentration, it is necessary to integrate $C(r,\phi)$ over an annular cylindrical volume surrounding the dislocation having an inner core radius of **b**, the Burgers vector, and an outer radius of R, where

$$R = (\pi\rho)^{-\frac{1}{2}} \tag{5}$$

and ρ is the dislocation density. Hirth and Carnahan [2] have performed this integration, expressing the result as a series expression. Using their result, we can express the enhanced solubility as

$$\Delta C = \gamma \left(\frac{a}{\beta}\right)^2 \{\tfrac{1}{2} (1 - 2C_o) (1 - C_o)^2 \ln \beta + \sum_{m=1}^{\infty} (-\gamma)^{m-1} \sum_{n=1}^{\infty} \frac{(1 - \beta^{-2a})}{na^2} \left[\frac{(ma/2)^{n+1}}{(n+1)}\right]^2\} \; ; \tag{6}$$

where

$$\gamma = C_o/(1 - C_o) ,$$
$$8 = R/b ,$$
$$a = A/(bkT) ,$$
$$\Delta C = C_{ave} - C_o .$$

Equation (6) was evaluated numerically for AISI 316 with the following assumed values:

shear modulus G = 10 MPa,
Poisson's ratio v = 0.3,
atomic volume $\Omega = 1.132 \times 10^{-29}$ m^3,
carbon misfit volume V = 0.64 Ω.

As discussed in Reference 1, the ideal carbon solubility for an Fe-Ni-Cr alloy with 14%nickel is given by

$$\log_{10} C_o = 2.37 - 6170/T , \qquad (7)$$

where T is the absolute temperature in °K.

Table 1 contains calculated values for C_o and C_{ave} for various temperatures and dislocation densities relevant to the fast reactor irradiation of AISI 316. It can be seen from the results in Table 1 that the enhancement of carbon solubility by trapping in the dislocation stress-field is not very large except for high dislocation densities. For cold-worked materials ($\sim 10^{16}$ cm^{-2}), the enhancement of carbon solubility varies from +31% at 700°C to +108% at 300°C.

5.3 Discussion

Our previous analysis of carbon solubility was motivated by several observations.[1,3] First, the swelling of AISI 316 appears to be suppressed temporarily in a similar manner by either cold-work or carbon. Second, carbide precipitates are known to favor edge dislocations as nucleation sites. Third,

TABLE 1

SOLUBILITY OF CARBON (ATOMIC FRACTION) IN AISI 316
AS A FUNCTION OF DISLOCATION DENSITY

Temperature		Ideal Solubility	Solubility C_{ave} with Dislocations		
°C	°K	C_o	$\rho=10^{12}$ m^{-2} (annealed)	10^{14} m^{-2} (lower bound of irradiation-induced densities)	10^{16} m^{-2} (20% cold-worked)
300	573	4.00×10^{-9}	4.00×10^{-9}	4.08×10^{-9}	8.48×10^{-9}
400	673	1.59×10^{-7}	1.59×10^{-7}	1.61×10^{-7}	2.88×10^{-7}
500	773	2.44×10^{-6}	2.44×10^{-6}	2.47×10^{-6}	3.93×10^{-6}
600	873	2.01×10^{-5}	2.01×10^{-5}	2.02×10^{-5}	2.96×10^{-5}
700	973	1.07×10^{-4}	1.07×10^{-4}	1.08×10^{-4}	1.48×10^{-4}
800	1073	4.17×10^{-4}	4.17×10^{-4}	4.19×10^{-4}	5.47×10^{-4}

cold-working also appears to delay the phase development of some phases and the microchemical evolution of the alloy matrix. Finally, there appears to be no effect of cold-work on swelling when carbon and other solutes are absent.[4] This phase development appears to be instrumental in determining the duration of the transient regime of swelling. It was argued that the higher solubility of carbon in cold-worked material would provide a smaller effective supersaturation, and thus a lower driving force for carbide nucleation. In light of the present results the previous argument must be incorrect in that the magnitude of the reduction in driving force is deemed insufficient to provide a basis for the effect of cold work at all temperatures. Perhaps at lower temperatures (~300°C)a factor of two reduction is significant. Note in Reference 3 that factors of two in carbon level lead to pronounced changes in the duration of the transient regime of swelling. At most higher temperatures however an

alternative mechanism must be found to explain the effect of cold work on swelling and its dependence on carbon level.

It is well known that nucleation of carbide precipitates is generally very heterogeneous, and occurs preferentially at favorable sites. In spite of the negligible effects of dislocations to enhance the average solubility of carbon, the local enrichment of carbon near the dislocation core can be very large indeed. Furthermore, the large strain field near dislocations can substantially reduce the nucleation barrier for carbide precipitation.

In a cold-worked material it then seems reasonable to expect that a large number of small carbide nuclei exist already prior to irradiation. In solution-annealed material, on the other hand, carbide nuclei are fewer in numbers but larger in size, and associated with favorable sites other than dislocations.

When irradiated, individual dislocations begin to climb and interact, leading to a reduction in density in case of the cold-worked material. Carbide nuclei, which were stable in the dislocation stress-field, become now subcritical in the absence of the dislocations. As a result, carbide nuclei may redissolve, and carbon may precipitate later at more stationary sites such as grain boundaries, slow growing Frank loops and possibly voids. This argument would most likely apply at the higher irradiation temperatures.

In contrast, the larger carbide nuclei present in solution-annealed materials would not be so vulnerable and might remain stable under irradiation, and carbon precipitation would then continue at the already established carbide particles.

An aiternate approach to this issue is to question either the validity or the general applicability of the original observation that prompted this study. In an earlier study [4] it was shown that in the absence of solutes such as carbon there did not appear to be any influence of cold-work on swelling in AISI 316. This observation was made in steel irradiated at 550°C in the Oak Ridge Research Reactor. Although this reactor has an order of magnitude lower

displacement rate than that of EBR-II, the temperature of 550°C is very close to the 525°C transition temperature observed for the effect of carbon in the steel during EBR-II irradiation. (Above ~525°C swelling increases with carbon additions; the opposite is true below ~525°C.) If a synergism exists between the influence of carbon and cold-work, perhaps the interaction is not best observed at a temperature where the competing influences of carbon on swelling are balanced against each other.

5.4 Conclusions

The interaction of carbon and dislocations induced by cold-working of AISI 316 is not as large as previously imagined. It appears however that it still may be sufficient at low irradiation temperatures to prolong the transient regime of swelling. At higher temperatures other as-yet unidentified physical mechanisms as required to explain the effect of cold-work on swelling. A possible high temperature mechanism is advanced which is based on the stability of carbide nuclei in a rapidly evolving dislocation network.

6.0 References

1. F. A. Garner and W. G. Wolfer, "The Influence of Dislocation Density and Radiation on Carbon Activity and Phase Development in AISI 316," DAFS Quarterly Progress Report, DOE/ER-0046/4, p. 88.

2. J. P. Hirth and B. Carnahan, Acta. Met., 26 (1978) 1795-1803.

3. F. A. Garner, "The Microchemical Evolution of Irradiated Stainless Steels," Proc. Symposium on Phase Stability During Irradiation, October 5-9, 1980, Pittsburgh, PA, p. 165.

4. H. R. Brager and F. A. Garner, "Further Examination of Swelling of 'Pure' AISI 316 Irradiated in ORR," DAFS Quarterly Progress Report, DOE/ER-0046/7, p. 172.

MICROCHEMICAL EXAMINATION OF ANNEALED AISI 316 (DO-HEAT) IRRADIATED IN HFIR

H. R. Brager and F. A. Garner (Hanford Engineering Development Laboratory)

1.0 Objective

The objective of this effort is to determine the relative contributions of helium and the radiation-induced microchemical evolution on the swelling behavior of austenitic alloys.

2.0 Summary

A new and simple examination technique involving X-ray analysis of large areas of extraction replicas was used to determine the average precipitate composition of an irradiated specimen. When applied to specimens irradiated in **HFIR**, the level of nickel and silicon segregated into precipitates is found to correlate with the level of swelling. The high level of nickel (29 wt.%) found in the precipitates of annealed AISI 316 (DO-heat) at 47 dpa and 550°C agrees with the level found independently by Garner and Porter in comparable specimens of a different heat of 316 irradiated in EBR-II.

3.0 Program

Title: Irradiation Effects Analysis (AKJ)
Principal Investigator: D. G. Doran
Affiliation: Hanford Engineering Development Laboratory

4.0 Relevant DAFS Program Plan Task/Subtask

II.C.17 Microstructural Characterization

5.0 Accomplishments and Status

5.1 Introduction

In earlier reports [1-2] it was shown that there were two possible interpretations of the effect of helium on swelling derived from the available swelling data on AISI 316 (DO-heat) irradiated in HFIR and EBR-II. The major question being addressed is whether the swelling rate will continue to increase with additional fluence as observed in EBR-II or whether the large helium levels and void densities produced in HFIR will suppress an increase in the swelling rate beyond the limit of the current HFIR data.

The first interpretation assumes that cold-worked AISI 316 eventually reaches the same steady-state swelling rate in both HFIR and EBR-II.[3] Noting that the steady-state swelling rates for both annealed and cold-worked specimens irradiated in the low He/dpa environment of EBR-II are identical, it is reasonable to postulate that they will be independent of cold-work in HFIR also. As shown in Figure 1, the HFIR data on annealed steel exhibit a swelling rate which is not only comparable to that of the composite HFIR/EBR-II curve for 20% cold-worked 00-heat but is also comparable to the steady-state swelling rate observed in other U.S. breeder steels irradiated in EBR-II.

The second approach (Figure 2) is to assume that the higher void densities induced by HFIR irradiation will lead to earlier swelling but lower steady-state swelling rates.[4] In effect it is assumed in this approach that no additional curvature occurs in the swelling curve beyond the 60 dpa HFIR data point. However, the void densities in the annealed steel irradiated in HFIR are comparable (~ a factor of two lower) to those of the cold-worked steel and yet no suppression of an increase in the swelling rate was observed in the annealed specimens.[9]

The difference in the two interpretations actually arises from a more fundamental question. What are the relative contributions of helium production and microchemical evolution to the nucleation and growth of voids? In order to assess

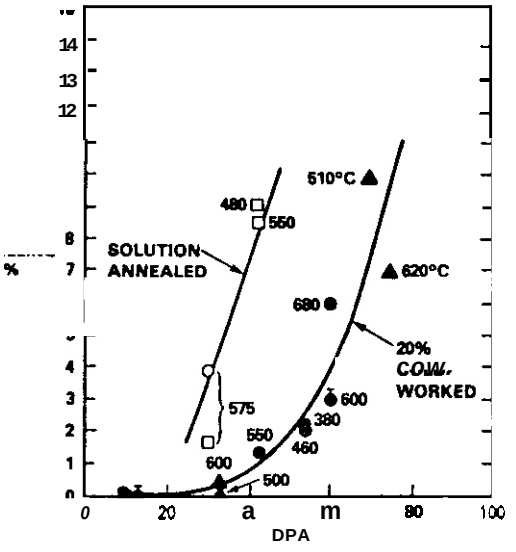

FIGURE 1. Comparison of Annealed and Cold-Worked DO-Heat in HFIR kith That of Cold-Worked DO-Heat in EBR-II.(1-3) All temperatures used are the nominal irradiation values quoted for the original experiments. The HFIR displacement levels have not yet been corrected upward by 12% to reflect the displacement contribution of the $^{59}Ni(n,\alpha)^{56}Fe$ reaction.(6) Solid circles are HFIR data and solid triangles are EBR-II data; open circle is microscopy datum and open squares are immersion density data.

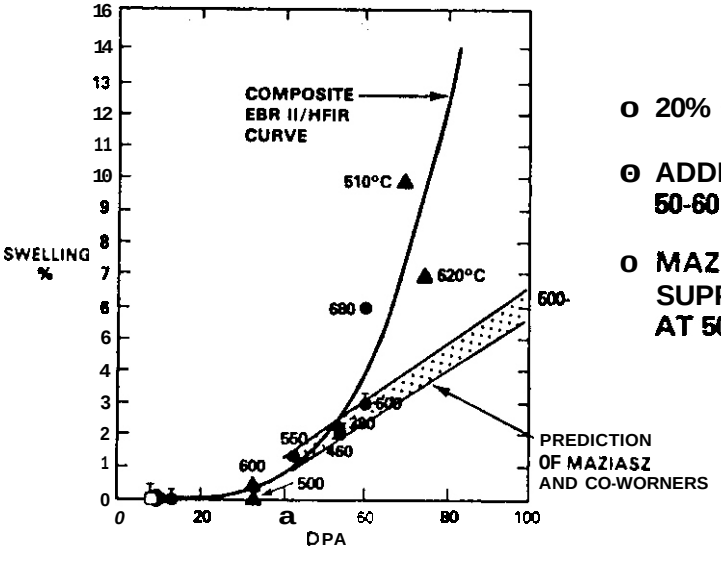

- **20% CW 316 DATA ONLY**
- **ADDITIONAL CURVATURE ABOVE 50-60 dpa?**
- **MAZIASZ AND CO-WORKERS PREDICT SUPPRESSION OF SWELLING RATE AT 500-600°C**

FIGURE 2. Comparison of the Composite Swelling Curve for 20% Cold-Worked DO-Heat (from Figure 1) with Predictions Based on HFIR Data Only and Rate Theory Principles Emphasizing the Influence *of* Void Density. (1-4)

this question the microchemical evolution of cold-worked DO-heat was examined and no major differences were found in the microchemical evolution experienced in HFIR and EBR-II.[1-3] However, in all cases where substantial swelling was observed, there was significant segregation of elements, resulting in depletion of nickel and silicon (and sometimes molybdenum and carbon) from the matrix and their enrichment in second phase precipitates. If the solution annealed specimen, which swelled ~9%, behaved as expected by microchemical concepts of swelling, it is anticipated that the second phases formed during irradiation are significantly enriched in nickel and silicon. Attention has now been focused on the microchemical evolution in HFIR of the DO-heat steel in the annealed condition.

5.2 Examination of Annealed DO-Heat

An annealed specimen of DO-heat irradiated at a nominal temperature of 480°C to a nominal dose of 42 dpa in HFIR was supplied by P. J. Maziasz of Oak Ridge National Laboratory. The actual temperature is probably much higher due to an earlier underestimate of the gamma heating level. Maziasz estimates the actual temperature to be ~550°C.[4]

Prior to the final thinning of this specimen for microscopy and X-ray analysis, extraction replicas were made and examined. A new and simple approach was used to determine the average composition of the precipitates in this specimen and to test the hypothesis that higher swelling rates can be correlated with higher levels of nickel removal into precipitates.

A single-step carbon extraction replica was made after electropolishing the specimen surface. EDX analysis was then performed at 2 Kx to 10 Kx on large areas of the replica, including many thousands of precipitate particles. A typical EDX spectrum from many precipitates is shown in Figure 3.

As shown in Table 1, nine separate examinations yielded a remarkably consistent average precipitate composition. As anticipated, the precipitates were uniformly high in nickel (29.2 wt.%) and silicon (10.5 wt.%). The precipitates also contained ~1.3% vanadium, formed primarily by the transmutation of ^{50}Cr.[5]

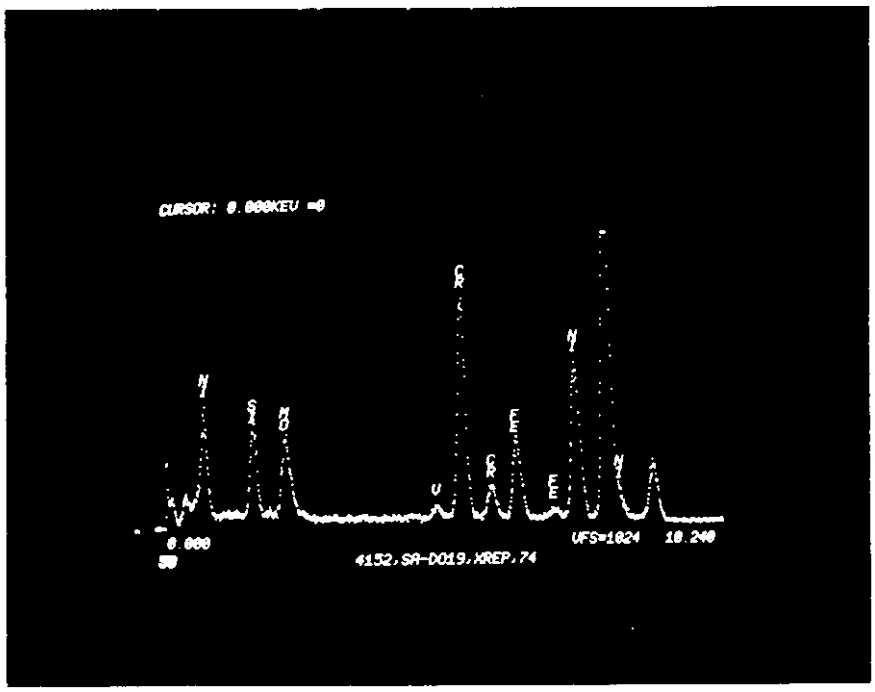

FIGURE 3. Typical EDX Spectra Obtained for Annealed 316 (DO-heat) From Thousands of Precipitates on a Carbon Extraction Replica. This specimen was irradiated to 47 dpa at ∿550°C. Both the temperature and displacement level have been corrected upward to reflect recent insights on the radiation environment in HFIR.

TABLE 1

EDX MEASUREMENTS: AVERAGE COMPOSITION OF PRECIPITATES ON THE CARBIDE EXTRACTION REPLICA FROM SOLUTION-ANNEALED 316 (DO-HEAT)

Spec. # DO-19 $\phi t \sim 47$ dpa T ∿550°C.

	Composition (wt.%)					
Analysis #	Si	V	Cr	Fe	Ni	Mo
72	11.3	1.5	29.1	12.3	29.7	15.9
73	10.7	1.1	29.2	12.7	29.3	16.7
74	10.2	1.3	30.1	12.7	28.9	16.6
75	10.3	1.2	30.4	12.1	29.2	16.5
76	10.5	1.3	29.3	12.5	29.3	16.8
77	10.2	1.1	32.4	13.6	29.0	13.4
78	10.3	1.6	31.9	11.2	28.a	16.0
79	10.4	1.3	29.7	11.9	28.9	17.6
80	10.6	1.5	29.8	12.3	29.4	16.0
Average	10.5	1.3	30.2	12.4	29.2	16.2

Note: Corrected displacement level and temperature.

The identities of the phases in this specimen are now being determined.

5.3 Examination of 20% Cold-Worked DO-Heat

This method of estimating the average precipitate composition by examining many particles was also applied to extraction replicas taken from a 20% cold-worked specimen examined earlier.[1-3] The irradiation proceeded in HFIR to a reported dose of 42 dpa at a nominal temperature of 550°C and swelled only 1.5%. The actual temperature is thought to be closer to 650°C.[1-3]

A typical EDX spectrum is shown in Figure 4, and Table 2 shows that, compared to the annealed specimen, the average nickel content in the precipitates is lower (12.3 wt.%), the silicon is lower (6.1 wt.%) but the vanadium content is larger (2.5%). These precipitates are rich in molybdenum (25.8 wt.%) which is consistent with their earlier identification as being comprised mostly of the Laves phase.

5.4 Discussion

It must be recognized that comparison of these two HFIR specimens with similar specimens irradiated in EBR-II must include the difference and uncertainties in their irradiation temperatures as well as the fact that their reported displacement doses are also underestimated by ~12%.[6] This latter factor arises from the previous oversight of the displacement contributions arising from the $^{59}Ni(n,\alpha)^{56}Fe$ reaction.

Since the actual irradiation temperatures of the annealed and cold-worked specimens vary by ~100°C, one would not expect the precipitate identities to be the same, as shown by Yang and coworkers.[7] The extraction technique used here also does not allow a confident measure of the relative volume of precipitation, as the extraction efficiency varies between replicas and between given areas of a particular replica.

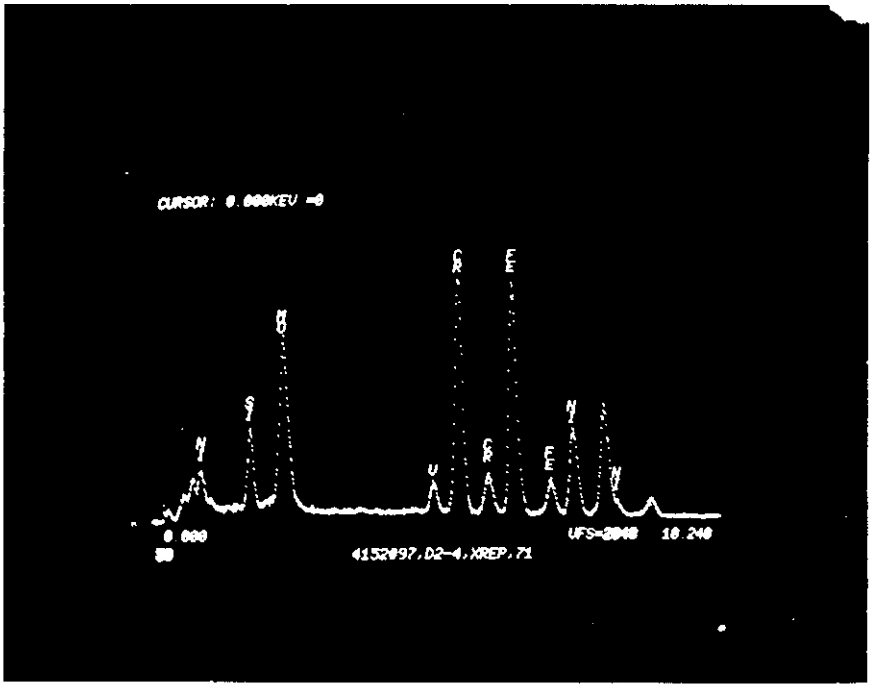

FIGURE 4. Typical EDX Spectra for Precipitates on an Extraction Replica of 20% Cold-Worked AISI 316 (DO-heat) Irradiated in HFIR to 47 dpa and ~650°C.

TABLE 2

EDX MEASUREMENTS: AVERAGE COMPOSITION OF PRECIPITATES ON THE CARBIDE EXTRACTION REPLICA FROM 20% CW 316 (DO-HEAT)

Spec. # D2-4 $\phi t \sim 47$ dpa $T \sim 650°C$

	composition (wt.%)					
Analysis #	Si	V	Cr	Fe	Ni	Mo
56	6.1	2.6	22.2	30.5	12.0	26.3
57	5.8	2.6	23.8	30.2	13.4	23.9
58	6.4	2.5	22.4	29.0	12.2	27.2
59	6.1	2.6	24.0	28.5	12.5	26.0
60	6.5	2.5	22.7	28.2	12.7	27.1
67	5.4	2.3	25.9	30.7	11.5	24.0
71	6.0	2.6	23.8	28.9	12.0	26.5
Average	6.1	2.5	24	30	12.3	26

Note: Corrected displacement level and temperature.

It is safe to say however that the precipitates in the specimen with the higher swelling level exhibit higher levels of silicon and nickel. The determination of the consequences of this segregation on the average matrix alloy content awaits examination of the thin film specimen.

Recently it has been shown that the irradiation of annealed AISI 316 leads to a correlation of the swelling with the level of precipitation and its nickel content.[8] In that study the precipitate< were in stressed specimens and were bulk extractedby another technique. The heat of steel used in the referenced report exhibits a swelling behavior similar to that of the 00-heat.

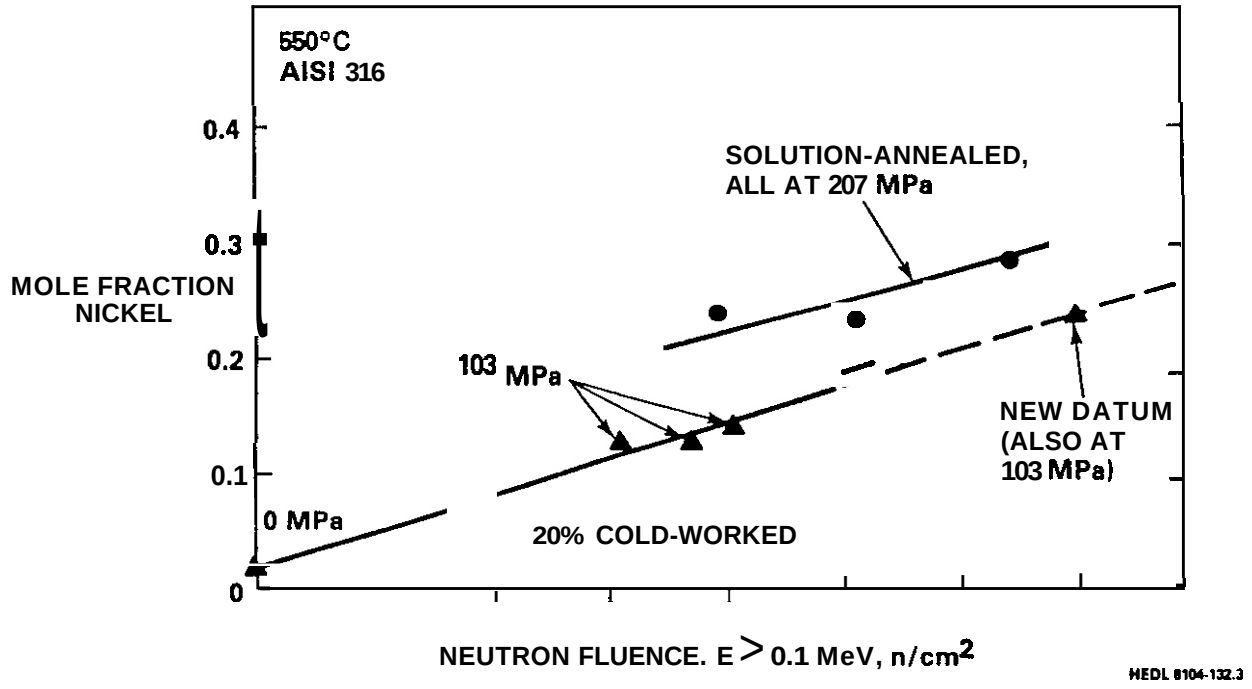

FIGURE 5. Nickel Content of Precipitates Extracted From Pressurized Tubes of AISI 316 (N-lot, heat 87210) Irradiated in EBR-II at 550°C, as Reported by Garner and Porter. (8)

5.5 Conclusions

A new and simple examination technique involving X-ray analysis of large areas of extraction replicas was used to determine the average precipitate composition of an irradiated specimen. When applied to specimens irradiated in HFIR, the level of nickel and silicon segregated into precipitates is found to correlate with the level of swelling. The high level of nickel (29 wt.%) found in the precipitates of annealed AISI 316 (DO-heat) at 47 dpa and 550°C agrees with the level found independently by Garner and Porter in comparable specimens of a different heat of 316 irradiated in EBR-II.

6.0 References

1. H. R. Brager and F. A. Garner, "Influence of Neutron Spectra on the Radiation-Induced Evolution of 316," Proc. International Conference on Neutron Irradiation Effects, Argonne National Laboratory, November 9-12, 1981 (to be published in J. Nucl. Mater.).

2. H. R. Brager and F. A. Garner, "The Radiation-Induced Evolution of AISI 316 (DO-heat) in HFIR and EBR-II," DAFS Quarterly Progress Report, DOE/ER-0046/7, November 1981, p. 127.

3. H. R. Brager and F. A. Garner, "Comparison of the Swelling and the Microstructural/Microchemical Evolution of AISI 316 Irradiated in EBR-II and HFIR," DAFS Quarterly Progress Report, DOE/ER-0046/6, August 1981, p. 162, also Proc. Second Topical Meeting on Fusion Reactor Materials, Seattle, WA, August 9-12, 1981.

4. P. J. Maziasz, "Some Effects of Increased Helium Content on Void Formation and Solute Segregation in Neutron-Irradiated Type 316 Stainless Steel," accepted for publication in J. Nucl. Mater.

5. J. F. Bates, F. A. Garner and F. M. Mann, "The Effect of Solid Transmutation Products on Swelling in 316 Stainless Steel," to be published in J. Nucl. Mater., also DAFS Quarterly Progress Report, DOE/ER-0046/7, p. 199.

6. F. A. Garner and F. M. Mann, "The Impact of the $Ni^{59}(n,\alpha)^{56}Fe$ Reaction on Damage Calculations for HFIR," this report.

7. W. J. S. Yang, H. R. Brager and F. A. Garner, "Radiation-Induced Phase Development in AISI 316," Proc. TMS-AIME Symposium on Phase Stability During Irradiation, J. R. Holland, D. I. Potter and L. K. Mansur (Eds.), Pittsburgh, PA, October 5-9, 1980, p. 257.

8. F. A. Garner and D. L. Porter, "The History Dependence of the Microchemical Evolution of Irradiated AISI 316 and 304L Stainless Steels," in Ref. 7, p. 176.

9. P. J. Maziasz, F. W. Wiffen and E. E. Bloom, "Swelling and Microstructural Changes in Type 316 Stainless Steel Irradiated Under Simulated CTR Conditions," Radiation Effects and Tritium Technology for Fusion Reactors, CONF-750989, Volume 1, pp. 259-288.

FACTORS INFLUENCING THE SWELLING OF 300 SERIES STAINLESS STEELS

F. A. Garner (Hanford Engineering Development Laboratory) and D. L. Porter (Argonne National Laboratory - Idaho Falls)

1.0 Objective

The objective of this effort is to define the dependence of swelling of austenitic stainless steels on temperature, neutron flux and spectra, stress and composition. This is being done in order to provide a better framework from which to predict perturbations of swelling arising from history-sensitive variables unique to the fusion environment.

2.0 Summary

It appears that the primary difference between the swelling of AISI 304 and 316 lies in the duration of their transient regime. This difference appears to arise primarily from their difference in nickel content. It also appears that the major effect of temperature on swelling lies in the transient regime, most particularly at relatively low temperatures. There is a considerable temperature range over which the swelling may be considered to be independent of temperature but slightly dependent on the displacement rate. The influence of the displacement rate also lies primarily in the transient rather than steady-state regime. Since steady-state swelling is not as sensitive to temperature as expected, that implies that the swelling is not as sensitive as anticipated to the density of temperature-sensitive microstructural components such as voids and dislocation loops. This suggests that swelling will therefore not be as sensitive to helium content, another parameter which affects microstructural densities.

3.0 Program

Title: Irradiation Effects Analysis (AKJ)
Principal Invesitgator: D. G. Doran
Affiliation: Hanford Engineering Development Laboratory

4.0 Relevant DAFS Program Plan Task/Subtask

Task II.C.1 Effects of Material Parameters on Microstructure
Task II.C.2 Effects of Helium on Microstructure

5.0 Accomplishments and Status

5.1 Introduction

In order to develop a fission-fusion correlation for a given property change one must be certain that the prevailing description be correct for that property change in the fission environment. Otherwise the impact of fusion-relevant differences in helium/dpa ratio, solid transmutants or reactor operational history may be incorrectly predicted.

Recently, it has become apparent that the effect of helium on the swelling of AISI 316, for instance, is not as strong as previously anticipated.[1-2] Since helium is known to affect the void density, this implies that the swelling is not as dependent on void density as previously anticipated. Since the void and dislocation loop densities are very sensitive to temperature and displacement rate, any reassessment of the parametric sensitivity of swelling would naturally include these variables.

Another set of relevant variables involves the original composition of the alloy and the details of its subsequent microchemical evolution during irradiation.[3] It appears that one of the major questions to be addressed in the development of fission-fusion correlations for swelling is the definition of the relative contributions of helium and composition-related variables. The influence of differences in solid transmutants may also be of importance here.

There are only two compositionally-related structural materials for which there are sufficient data in the open literature to define the flux and temperature dependence of swelling and also to cast some light on the composition dependence of swelling. These are the two 300 series stainless steels AISI 316 and AISI 304L.

Reference 3 provides an overview of much of the published data on AISI 316. Reanalysis of the data on 304L has led to the conclusion that our prevailing conception of the parametric dependence of swelling must be altered in some respects. These changes also have a strong impact on the prediction of swelling response to changes in helium/dpa ratio.

5.2 The Dependence of Swelling on Nickel Content

The AISI 316 and 304 steels are quite similar in composition with two important differences. AISI 304 has less nickel (~9 vs. ~12-14%) and less molybdenum (0.02 vs. 2.5%). While some sensitivity of swelling has been observed to molybdenum content in AISI 316 [4-5] a major sensitivity to the nickel content has been observed.[6] Figure 1 shows a very steep dependence of swelling in austenitic alloys on nickel content at levels below 35%. This figure does not show whether the observed sensitivity arises from nickel's influence on the duration of the transient regime, or on the rate of swelling in the steady-state regime or both.

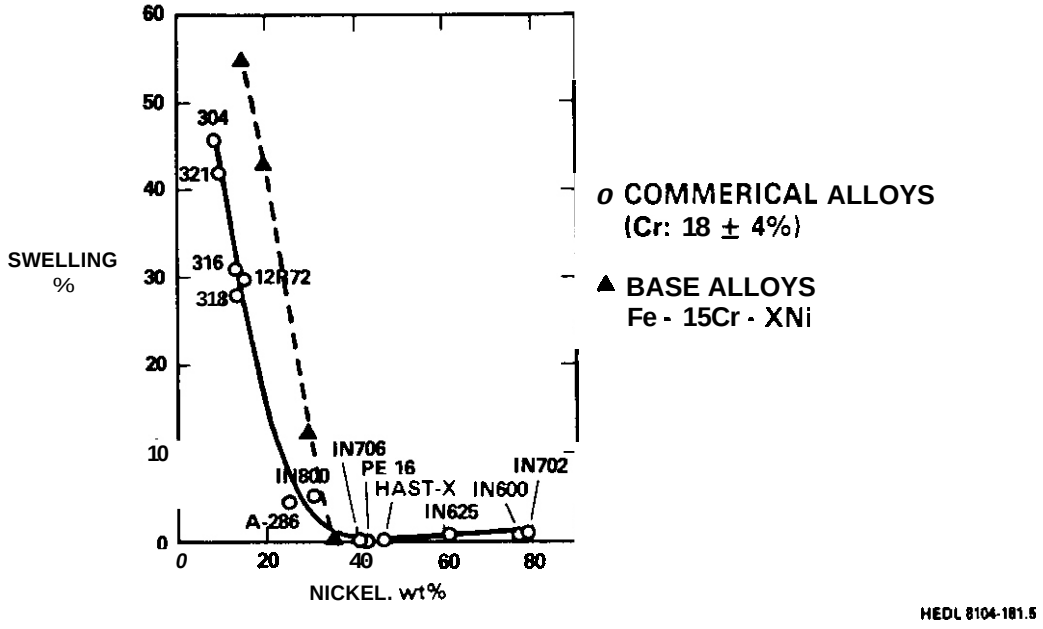

FIGURE 1 Swelling in Commercial and Base Alloys When Bombarded to 140 dpa With 5-MeV Ni^+ Ions at 625°C as Reported by Johnston and coworkers.(6)

There has been only a few published studies where AISI 316 and 304 has been irradiated side-by-side and yielded sufficient data with which to assess the role of nickel content on swelling of 300 series alloys. In the authors' opinion there are only two of these data sets on which to confidently base such an assessment. Figure 2 shows data published by G. L. Hofman [7] which clearly shows an extension of the duration of the transient regime of swelling with increasing nickel content. The data are not available to sufficient damage levels to draw any conclusions concerning the dependence on nickel of the steady-state swelling rate. Seidel and Einziger [8] have published data (Figure 3) however which show that the deformation rate due to creep and swelling is eventually the same for the two alloys, with 316 having the longer transient regime.

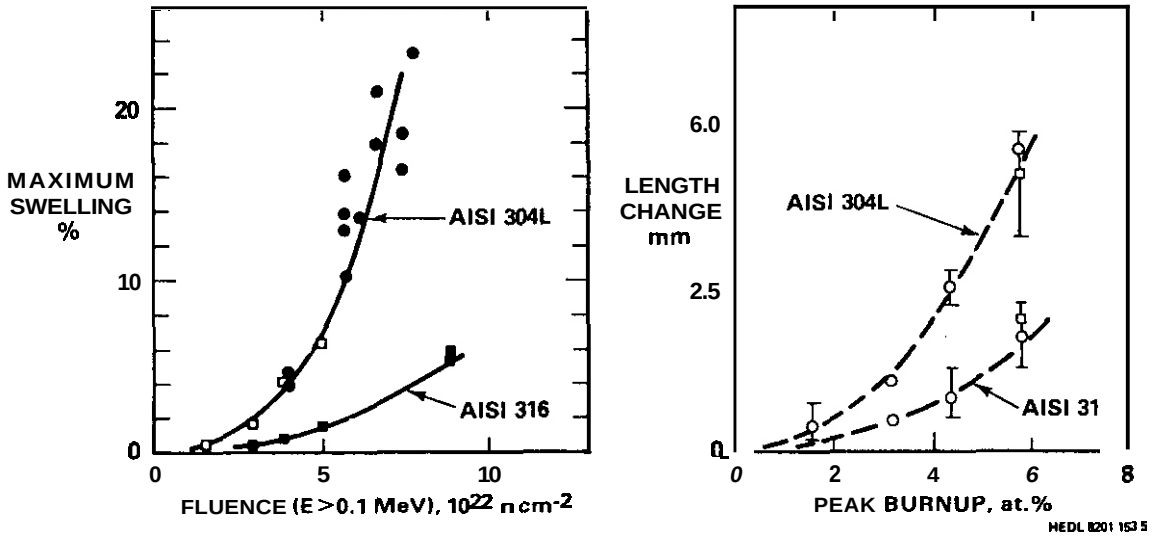

FIGURE 2. Comparison of the Swelling Behavior of Annealed 304 and 316 Stainless Steel When Used as Mark-I1 EBR-II Driver Fuel Cladding, as Reported by Hofman. (7)

It therefore appears that the primary influence of the differences in nickel and molybdenum levels lies not in the steady-state swelling rate but in the duration of the transient. This is in agreement with results of earlier studies. Bates [4] ascribed the role of molybdenum as slightly changing the "initialization fluence of swelling." Johnston and coworkers [6] demonstrated that nickel's primary influence on the swelling of Fe-Ni-Cr ternary alloys is to extend the duration of the transient regime of swelling (Figure 4).

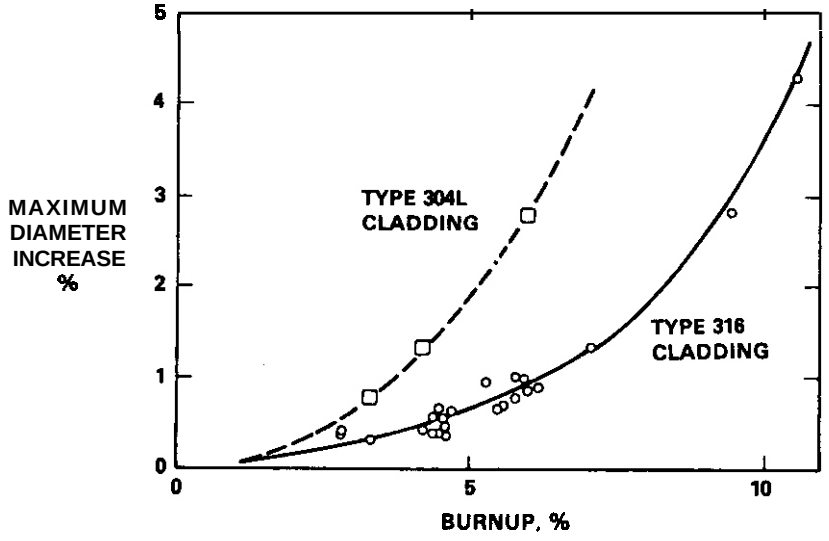

FIGURE 3. Comparison of the Deformation Behavior of Annealed 304 and 316 Stainless Steel at Higher Fluence, as Reported by Seidel and Einziger. (8)

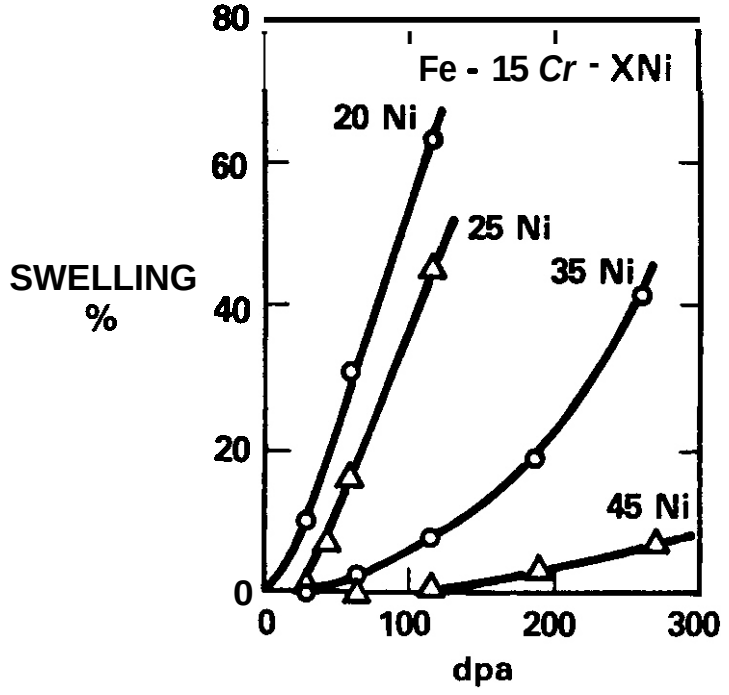

FIGURE 4. Dose Dependence of Swelling in Simple Ternary Alloys (Fe-15Cr-XNi) When Irradiated at 675°C With 5 MeV Nickel Ions, as Reported by Bates and Johnston. (6)

5.3 The Temperature Dependence of Swelling of AISI 304

In the development of swelling correlations for U.S. breeder reactors, the traditional approach has been to ignore differences in displacement rate within the data set and to incorporate the difference in neutron spectra by correlating swelling vs. the neutron fluence above a 0.1 MeV threshold. The fraction of the spectra above 0.1 MeV varies in the traverse across the EBR-II reactor and decreases in roughly the same manner as does the displacement rate per neutron. As shown in Figure 5, there is some variation in the displacements per threshold neutron, however, that has not been factored into earlier equation development efforts.

Another factor to consider is that most of the published incubation-plus-linear swelling correlations used one of two different methods to determine the "steady-state" swelling rates. As shown in Figure 6 the curvilinear approach anticipates that curvature in swelling may persist to very high fluences, while the linear approach assumes the transient to be relatively short. The linear approach always leads to an underestimation of the swelling rate, espeically if the swelling has not yet reached substantial levels.

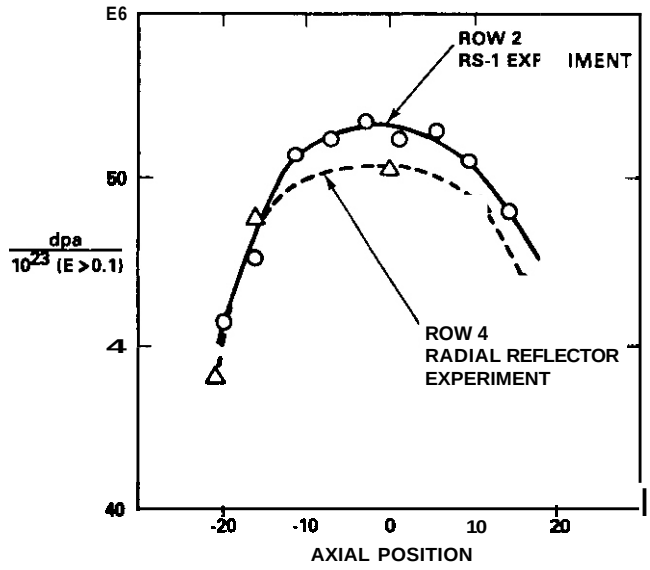

- CONVERSION FACTOR OF 50 dpa PER 10^{23} n/cm^2 (E>0.1) IS A POSITION-DEPENDENT APPROXIMATION
- GOOD ONLY FOR EBR II
- 68-77 dpa/10^{23} (E>0.1) IN HFIR

FIGURE 5. Displacement Characteristics of EBR-II Neutrons as a Function of Core Position for Two Recent Irradiation Experiments.

DETERMINATION OF "STEADY-STATE" SWELLING RATE

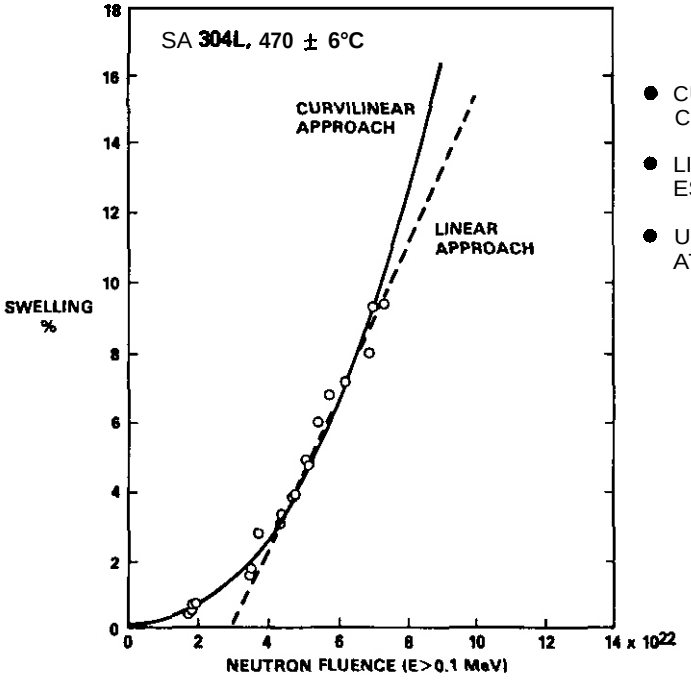

- CURVILINEAR APPROACH ASSUMES CURVATURE PERSISTS TO HIGH SWELLING
- LINEAR APPROACH ALWAYS UNDER-ESTIMATES ULTIMATE RATE
- UNDERESTIMATION ALWAYS GREATEST AT LOW FLUENCE **OR** LOW SWELLING

FIGURE 6. Comparison of Two Methods of Determining the "Steady-State" Swelling Rate. The data shown are described in reference 10 and were derived from annealed AISI 304L fuel capsule tubing irradiated in EBR-II.

With this background, let's consider the two major 304L data sets. The original perceptions of the temperature dependence of swelling were derived from analysis of the annealed 304L (L=low carbon) hexagonal thimbles that contained the control and safety rods in EBR-II. One of the most extensive swelling data sets on these components was published by Fish and coworkers [9] in 1973 and is shown in Figure 7. The strongly peaked swelling distribution along the thimbles arises primarily from the almost as strongly peaked fluence distribution shown in Figure 8. Note also that since the thimbles are directly in contact with the sodium coolant, no substantial exposure can be attained for temperatures below 370°C or above 440°C.

The data in Figure 7 were also plotted **vs.** fluence for relatively narrow temperature increments by Fish and coworkers. Figure 9 shows that the duration of the transient regime is strongly dependent on the flux and temperature variation

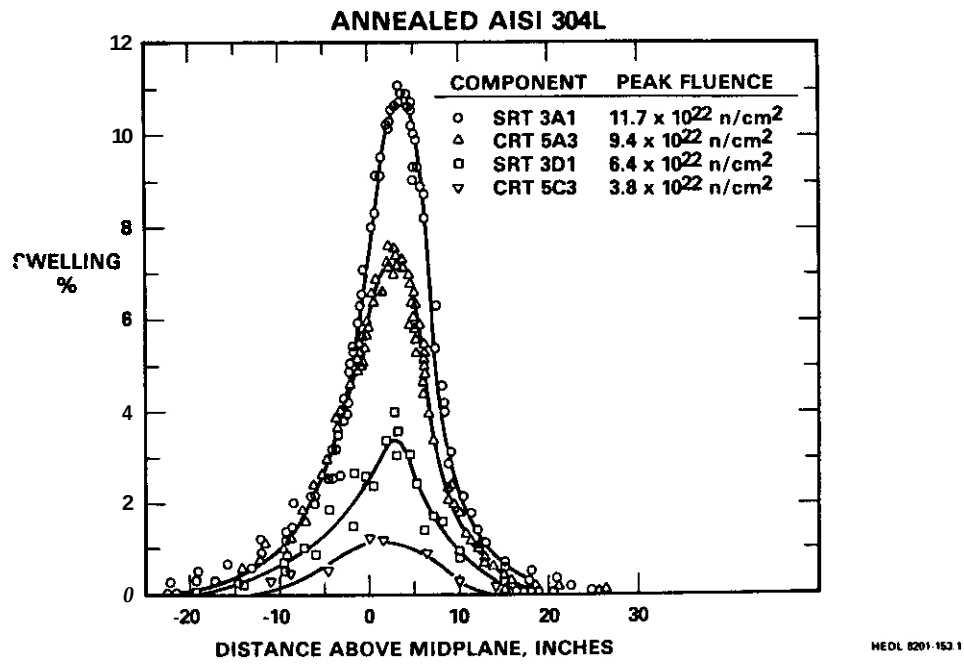

FIGURE 7. Swelling of Annealed AISI 304L Control Rod and Safety Thimbles in EBR-II. (9)

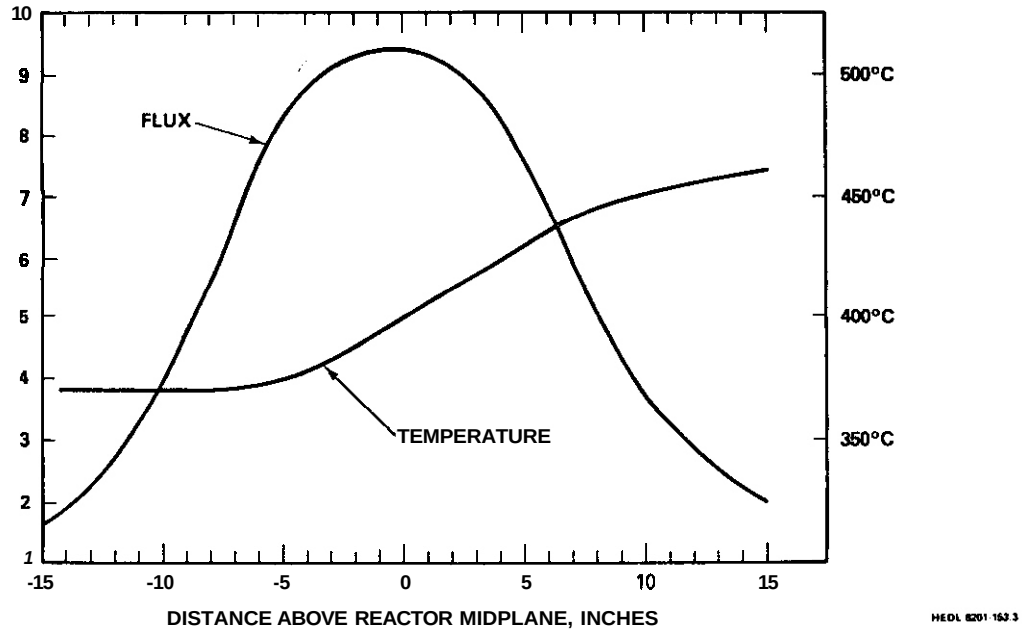

FIGURE 8. Relative Temperature and Flux (E >0.1 MeV) Profiles Experienced by the EBR-II Thimbles Shown in Figure 7.

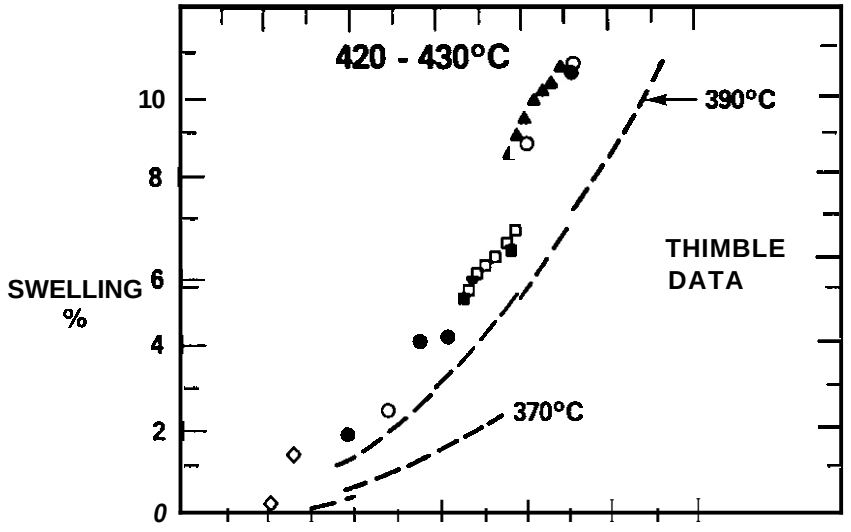

FIGURE 9. Swelling Data from 304L Thimbles in EBR-II in the Range 420-430°C.(9) (Each symbol represents a different thimble.) Trend lines for 370 and 390°C are also shown.

across the core. Only the trend lines of the correlation of Fish and coworkers were drawn for 370 and 390°C since the scatter increasesat lower temperature, particularly for 370°C. The scatter is thought by the authors to arise from the flux sensitivity of swelling at low temperatures.

It is important to note that the thimble data do not provide any indication whether the transient continues to shorten with increasing temperature. The data also say nothing definitive about the effect of temperature or flux on the steady-state swelling rate.

More recently, however, swelling data have become available from the outer capsule which forms half of the double containment of the EBR-II fuel rods. These data extend to higher temperatures than that reached by the thimbles. Note in Figure 10 that the capsule swelling trends in the range 400-435°C agree very well with thoseof the thimble. The actual capsule data points in this temperature range will be shown in a subsequent figure.

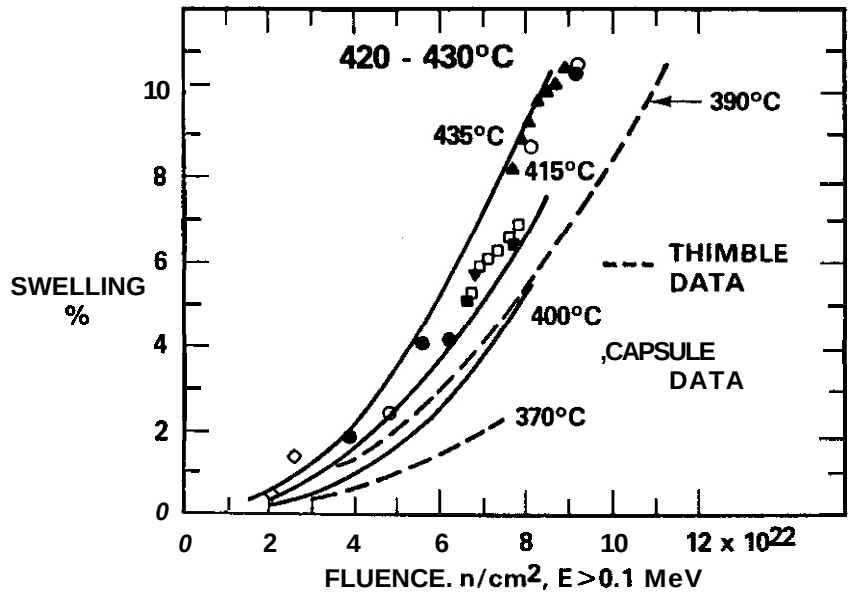

FIGURE 10. Comparison of Capsule and Thimble Data for Temperatures Below 435°C.

Flinn and Foster [10] have published an analysis of the capsule data in which the data points themselves were not shown. They estimated the steady-state swelling rate using the linear approach for each of ten small temperature intervals. As shown in the lower half of Figure 11 the steady-state swelling rate determined by this method is strongly dependent on temperature. Note also that the maximum swelling level at which the swelling rate was determined varies strongly with temperature.

Since the swelling at various temperatures has not yet reached a common level perhaps there exists a more illuminating way to present the data. Rather than break the data down into fine temperature intervals and analyze each set separately, note what happens when the seven of the ten original data sets are plotted together on Figure 12a. These seven sets cover the range 450-538°C.

Even in the absence of corrections for neutron spectra and other factors, it is obvious that the swelling of this steel exhibits a broad temperature regime or plateau in which the swelling is essentially independent of temperature. The appearance of a temperature-dependent swelling rate in Figure 11 arises out of

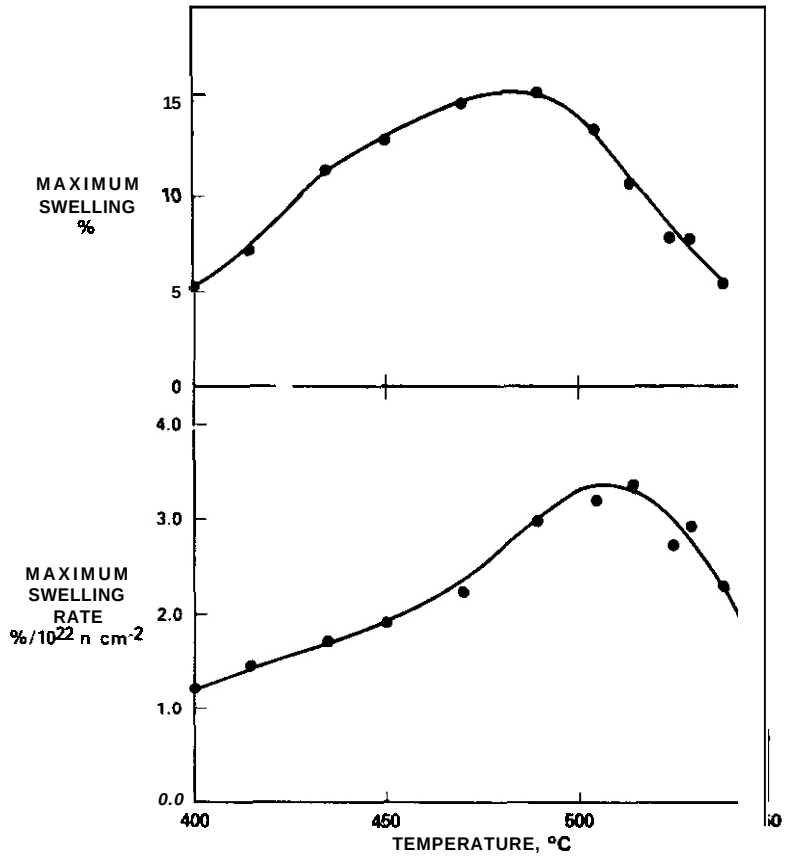

FIGURE 11. Swelling Rates as a Function of Temperature Reported by Foster and Flinn (10) for Annealed 304L Capsule Data. Also shown are the maximum swelling levels attained at each temperature.

the combined use of a linear approach and a swelling profile which is strongly peaked at intermediate temperatures. It appears that swelling in the range 450-538°C could be contained within a very narrow range of incubation parameters located about the trend line shown in Figure 12b. Note that this trend curve rather quickly approaches the same eventual swelling rate exhibited by a typical heat of AISI 316 irradiated in EBR-II. The difference in incubation parameter is due not only to the difference in nickel content but also the fact that the AISI 316 curve is for 20% cold-worked material. Cold-working is known to shift the duration of the transient period of 300 series stainless steels to higher fluence.(3)

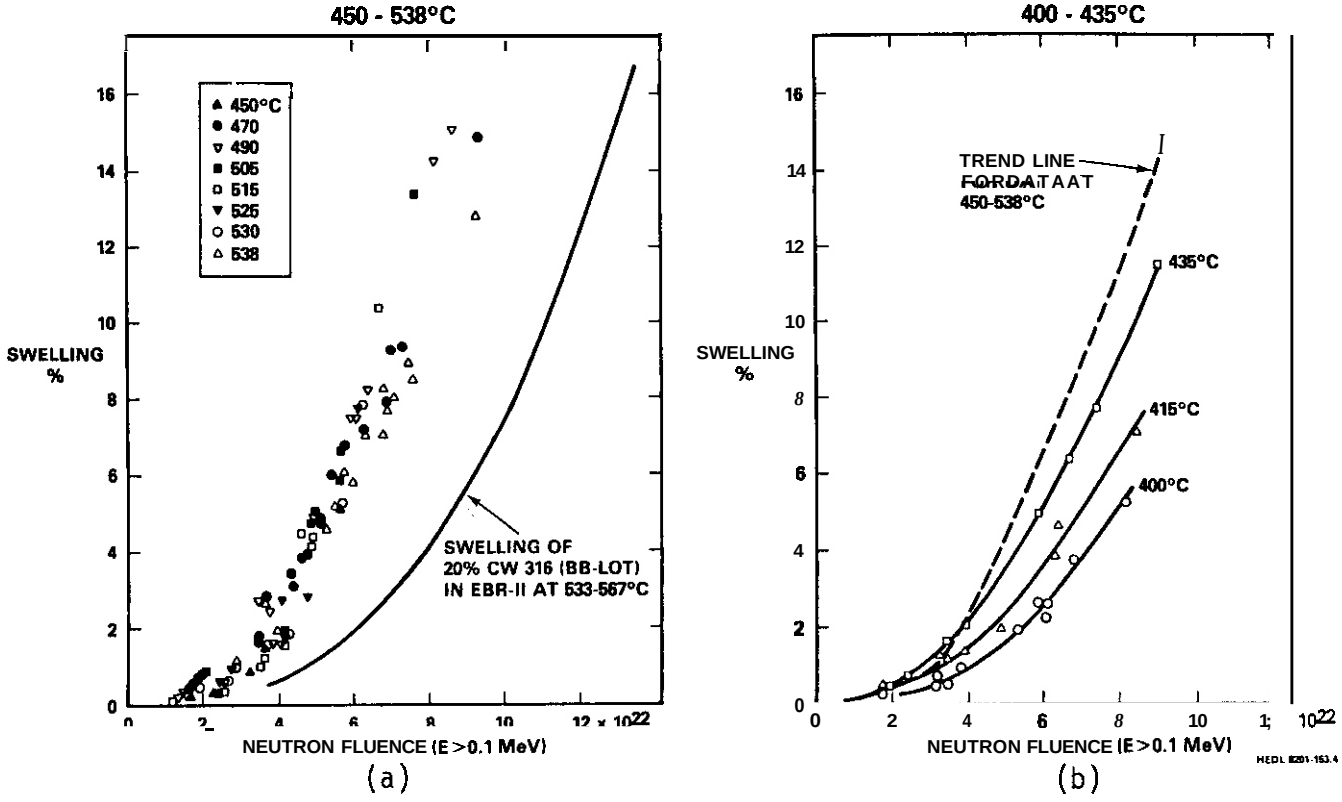

FIGURE 12. Swelling Behavior of Annealed 304L Fuel Capsules. Note relative independence of swelling on temperature in range 450-538°C. A typical cold-worked 316 curve is shown for comparison.

Note in Figure 12b that at lower temperature the duration *of* the transient regime is strongly sensitive to the simultaneous variations in neutron temperature, flux and displacement efficiency. If the swelling of this alloy is viewed at a given fluence level it would appear to exhibit a plateau (as seen in Figure 13), the upper limit of which lies somewhere above 540°C, the highest temperature reached by the capsules.

5.4 The Dependence of AISI 304 Swelling on Displacement Rate

Due to the coupling of the temperature profile and the neutron spectra and flux profiles in EBR-II it is impossible at this time to determine unequivocably

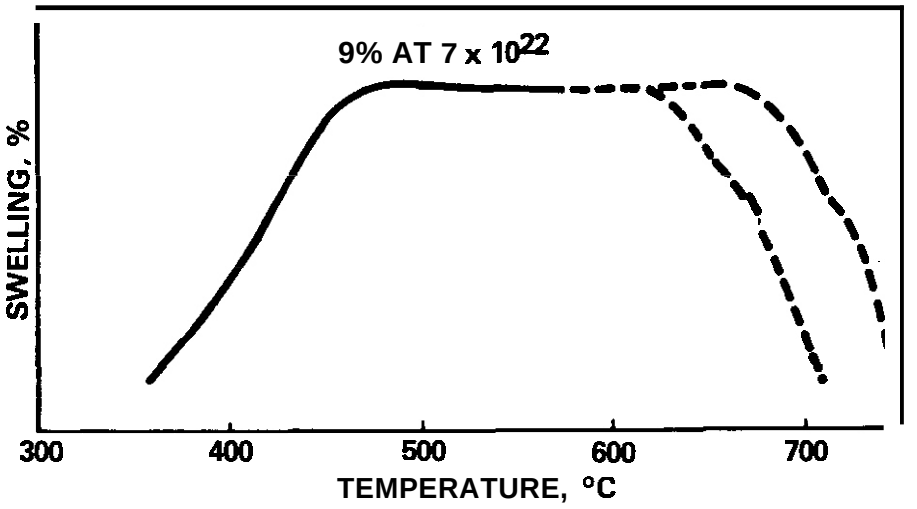

FIGURE 13. Schematic Illustration of the Swelling Behavior at 7 x 10^{22} n/cm^2 (E >0.1 MeV) of Annealed AISI 304L. The dotted lines indicate that no data is available at these temperatures. Straalsund et al. have shown swelling in AISI 304 at temperatures above 700°C.(12)

whether variations in the duration of the transient regime of swelling are due entirely or partially to variations in displacement rate. There is some additional low temperature data which suggest that displacement rate variations account for some of the scatter observed in swelling at a given temperature. Figure 14 shows the results of interim and final examinations of the diameter change of an annealed 304L creep tube. This tube was designed to function as a heat pipe and to be at essentially constant temprature (±8°C) throughout its full length.(11) At doses from 4 to 70 dpa the core center measurements showed a continual increase in diameter. When the core center portion reached 70 dpa measurements were made along the length of the tube. The factor of two difference in diameter change at approximately *20* dpa and 385°C is clearly a result of reaching the same exposure at two different displacement rates. It should be noted that the data taken below the core midplane are likely to be more accurate than those taken above the centerline, due to the cumulative upward axial expansion of the pipe due to swelling. This expansion moves the upper part of the rod into regions of lower neutron flux. (The pins are anchored only at the bottom of the assembly.) It is anticipated that the low fluence above-core data are therefore plotted at a fluence larger than actually attained and would otherwise fall above the curve describing the core center deformation.

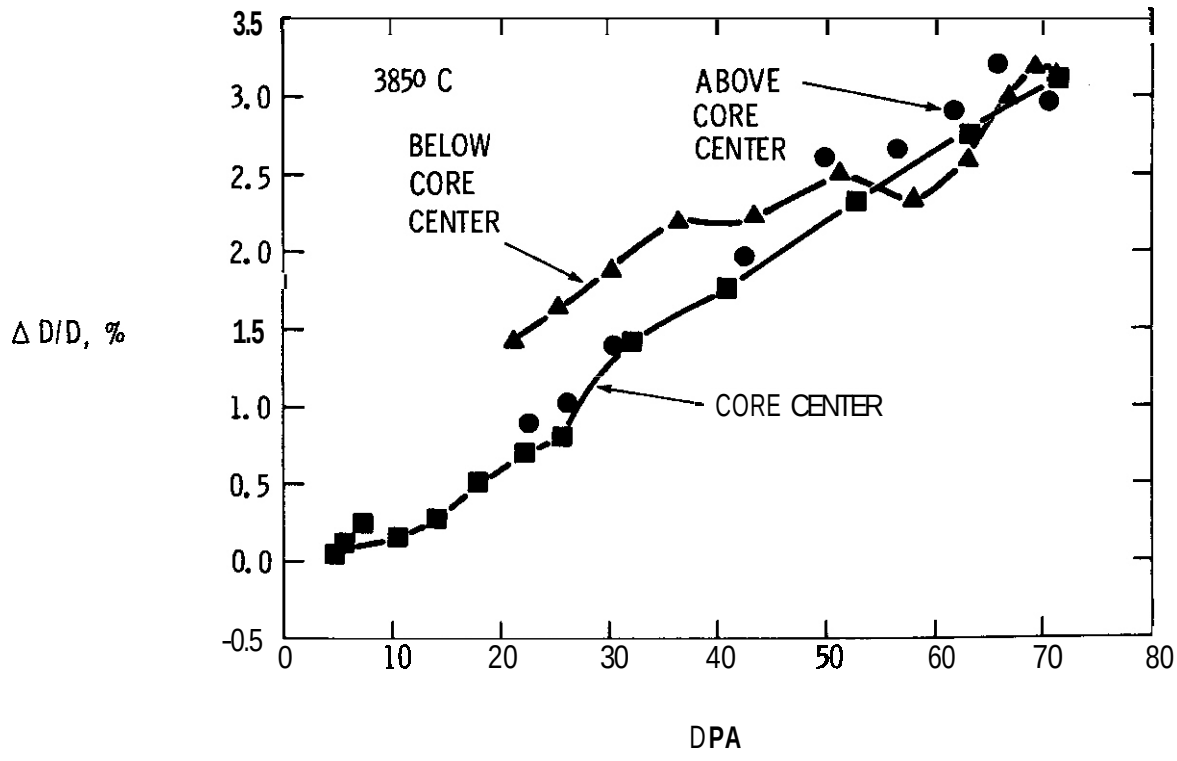

HEDL 7910-134.9

FIGURE 14. Displacement Rate Effect Observed in Deformation of Annealed 304L Creep Capsule Irradiated at 385°C as Reported by Porter and Hudman. (11)

Figure 15 shows that the swelling of 304L at 385°C decreases monotonically with displacement rate.[11] A similar trend is seen in 5% cold-worked **AISI** 316 at 400°C. Future reports will investigate the rate and spectrum dependence of swelling in more detail.

5.5 Discussion

It appears that the primary difference between the swelling of AISI 304 and 316 lies in the duration of their transient regime. This difference appears to arise primarily from their difference in nickel content. **It** also appears that the major effect of temperature on swelling lies in the transient regime, most particularly at relatively low temperatures. There is a considerable temperature range over which the swelling may be considered to be independent of temperature but slightly dependent on the displacement rate. The influence of the

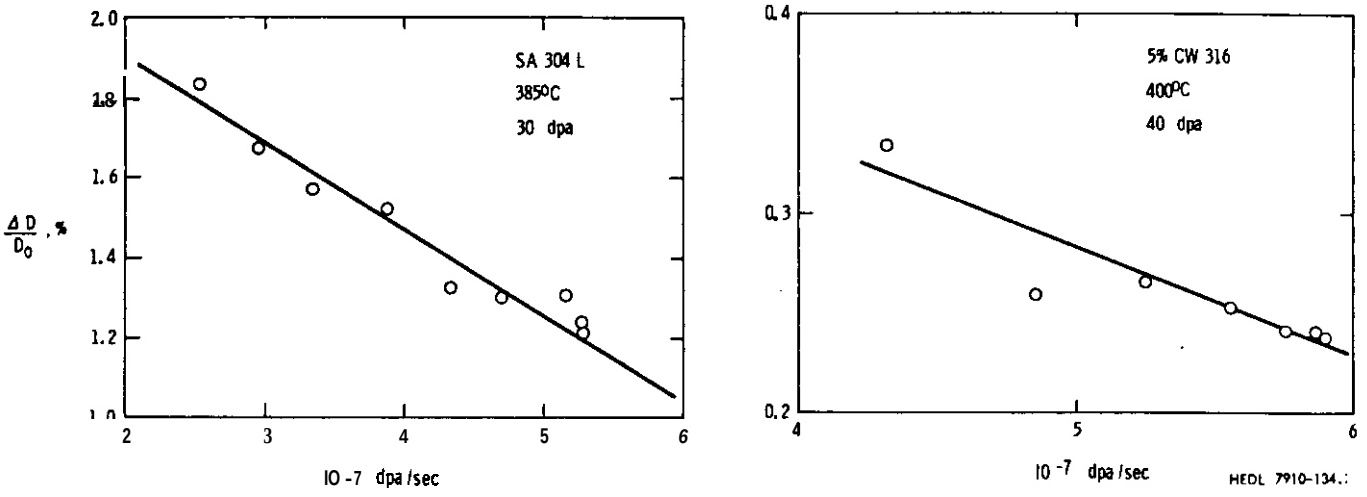

FIGURE 15. Displacement Rate-Dependent Swelling Observed by Porter and Hudman in EBR-II Irradiation of Two Austenitic Stainless Steels.(11)

displacement rate also lies primarily in the transient rather than steady-state regime. Since steady-state swelling is not as sensitive to temperature as expected, that implies that the swelling is not as sensitive as anticipated to the density of temperature-sensitive microstructural components such as voids and dislocation loops. This suggests that swelling will therefore not be as sensitive to helium content, another parameter which affects microstructural densities. This point will be addressed in more detail in later reports.

6.0 References

1. H. R. Brager and F. A. Garner, "Comparison of the Swelling and the Microstructural/Microchemical Evolution of AISI 316 Irradiated in EBR-II and HFIR," Proc. Second Topical Meeting on Fusion Reactor Materials, Seattle, WA, August 9-12, 1981, (in press).

2. H. R. Brager and F. A. Garner, "Influence of Neutron Spectra on the Radiation-Induced Evolution in AISI 316," accepted for publication in J. Nucl. Mater.

3. F. A. Garner, "The Microchemical Evolution of Irradiated Stainless Steels," Proc. Symposium on Irradiation-Phase Stability, October 5-9, 1980, Pittsburgh, PA, The Metallurgical Society of AIME, p. 165.

4. J. F. Bates, "Irradiation-Induced Swelling Variations Resulting From Compositional Modifications of Type 316 Stainless Steel," Properties of Reactor Structural Alloys After Neutron or Particle Irradiation, ASTM STP 570, American Society for Testing and Materials, 1975, pp. 369-387.

5. J. F. Bates, R. W. Powell and E. R. Gilbert, "Reduction of Irradiation-Induced Creep and Swelling in AISI 316 by Compositional Modifications," Effects of Radiation on Materials: Tenth Conference, ASTM STP 725, D. Kramer, H. R. Brager and J. S. Perrin (Eds.), American Society for Testing and Materials, 1981, pp. 713-734.

6. J. F. Bates and W. G. Johnston, Proc. ASTM International Conference on Radiation Effects in Breeder Reactor Structural Materials, Scottsdale, AZ, June 1977, pp. 625-644.

7. G. L. Hofman, Nucl. Tech., 47 (January 1980) 7-22.

8. 6. R. Seidel and R. E. Einziger, "In-Reactor Cladding Breach of EBR-II Driver-Fuel Elements," in Reference 6, p. 139.

9. R. L. Fish, J. L. Straalsund, C. W. Hunter and J. J. Holmes. "Swellina and Tensile Property Evaluations-of High Fluence EBR-II Thimbles," Effect: of Radiation on Substructure and Mechanical Properties of Metals and Alloys, ASTM STP 529, American Society for Testing and Materials, 1973, pp. 149-164.

10. J. P. Foster and J. E. Flinn, J. Nucl. Mater., 89 (1980) 99-112.

11. D. L. Porter and G. D. Hudman, "The Apparent Dose Rate Dependence of Swelling in Austenitic Stainless Steels," Transactions American Nuclear Society, Las Vegas, NV, 1980, p. 230.

12. J. L. Straalsund, H. R. Brager and J. J. Holmes, "Effects of Cold Work on Void Formation in Austenitic Stainless Steel," in Radiation-Induced Voids in Metals, J. W. Corbett and L. C. Ianniello (Eds.), U.S. A.E.C. Symposium Series 26, April 1972, p. 142.

7.0 Future Work

Analysis of data on neutron irradiated AISI 304 as well as on other 300 series steels will continue.

DISTRIBUTION

uc-20 (119)

uc-20c (77)

DOE-HQ/Office of Reactor
Research and Technology
NE-530
Washington, DC 20545

PB Hemmig, Safety & Physics

DOE-HQ/Office of Fusion Energy (2)
Washington, DC 20545

JF Clark, ER-70
JF Decker, ER-54, G-256

DOE-RL/Office of Asst Manager for
Projects & Facilities Management (2)
FMIT Project Office

GM Chenevert, Project Manager

DOE-RL/Office of Asst Manager
for Advanced Reactor Programs
Breeder Technology Division

KR Absher, Chief,
Technology Development Branch

Argonne National Laboratory (5)
9700 South Cass Avenue
Argonne, IL 60439

LR Greenwood EA Loomis
A. Taylor H. Wiedersich
RE Nygren

Battelle Memorial Institute (3)
Pacific Northwest Laboratory
P.O. Box 999
Richland, WA 99352

JL Brimhall
DA Oingee
TD Chikalla

Brookhaven National Laboratory
Associated Universities
Upton, Long Island, NY 11973

Chairman, Nuclear Energy Dept

Columbia University
Plasma Physics Laboratory
New York, NY 10027

RA Gross

General Atomic Company (2)
P.O. Box 81608
San Diego, CA 92138

GR Hopkins
JR Gilleland

INESCO
11011 Torreyana Rd
San Diego, CA 92121

RD Stevenson

Lawrence Livermore Laboratory (2)
P.O. Box 808
Livermore, CA 94550

MW Guinan
CM Logan

Los Alamos National Laboratory (2)
P.O. Box 1663
Los Alamos, NM 87544

OJ Dudziak
CR Emigh

Massachusetts Institute of Technology (5)
77 Massachusetts Avenue
Cambridge, MA 02139

L. Lidsky I-W Chen, 13-5118
NJ Grant, 8-305 DB Montgomery, NW21
JB Vander Sande, 13-5025

DISTRIBUTION (Cont'd)

Massachusetts Institute of Technology
Nuclear Reactor Laboratory
138 Albany St
Cambridge, MA 02139

OK Harling, NW12-204

McDonnell-Douglas Astronautics Co.
P.O. Box 516
St. Louis, MO 63166

D. Kummer

Mound Laboratory
P.O. Box 32
Miamisburg, OH 45342

Manager, Tech Appl & Dev

National Bureau of Standards
Gaithersburg, MD 20760

CD Bowman

Naval Research Laboratory (3)
Washington, DC 20375

I. Manning, Code 6672
JA Sprague, Code 6395
LE Steele, Code 6390

North Carolina State University
Department of Nuclear Engineering
Raleigh, NC 26707

JR Beeler, Jr.

Oak Ridge National Laboratory (12)
P.O. Box X
Oak Ridge, TN 37830

Director, Thermonuclear Div,
Bldg 9201-2
K. Farrell
ML Grossbeck
M. Roberts, Bldg 9204-1
PJ Maziasz
LK Mansur
NH Packan
FG Perey
J. Sheffield
JO Stiegler
C. Weisbin
FW Wiffen

Princeton University (2)
Plasma Physics Laboratory
Forrestal Campus
P.O. *Box* 451
Princeton, NJ 08544

K. Wakefield
H. Furth

Rockwell International
8900 DeSoto Ave
Canoga Park, CA 91304

D. Kramer

Sandia Laboratories (2)
P.O. Box 5800
Albuquerque, NM 87185

FL **Vook,** Org 5100

Sandia Laboratories
Livermore, CA 94550

WD Wilson

Science Applications, Inc.
1200 Prospect
LaJolla, CA 92037

Dr. H. Gurol

University of California (2)
Los Angeles, CA 90024

RW Conn
NM Ghoniem

University of Michigan
Nuclear Engineering
Ann Arbor, MI 48109

T. Kammash

University of Missouri
Mechanical & Aerospace Engineering
1006 Engineering Bldg
Columbia, MO 65211

M. Jolles

DISTRIBUTION (Cont'd)

University of Missouri
Dept of Nuclear Engineering
Rolla, MO 65401

A. Kumar

University of Virginia
Dept of Materials Science
Charlottesville, VA 22901

WA Jesser

University of Wisconsin
1500 W. Johnson Drive
Madison, WI 53706

WG Wolfer

Westinghouse
Advanced Reactors Division
P.O. Box 158
Madison, PA 15663

A. Boltax

Westinghouse
Research and Development Center (2)
1310 Beulah Road
Pittsburgh, PA 15235

S. Wood
JA Spitznagel

Commission for the European Communities
200. rue de la Loi
B-1049 Brussels, Belgium

J. Darvas

Energieonderzoek Centrum Nederland
Westerdionweg 3
NL-1755 ZG Petten, NH, The Netherlands

B. Van Der Schaaf

Swiss Federal Institute
for Reactor Research
CH-5303 Wuerenlingen, Switzerland

WV Green

EURATOM
Joint Research Center Ispra
Materials Science Division
1-21020 Ispra, Varese, Italy

P. Schiller

Hahn-Meitner Institute
fur Kernforschung
Glienickerstrasse 100
D-1000 Berlin,
Federal Republic of Germany

H. Wollenberger

Hokkaido University
Faculty of Engineering
Sapporo 060, Japan

T. Takeyama

Japan Atomic Energy Research Institute (2)
Physical Metallurgy Laboratory
Tokai Research Establishment
Tokai-mura, Naka-gun, Ibaraki-ken
Japan

S. Iwata, Physics
K. Shiraishi, Nuclear Fuel Research

Kernforschungsanlage Julich GmbH
Postfach 1913
D-517 Julich,
Federal Republic of Germany

H. Ullmaier

DISTRIBUTION (Cont'd)

Kernforschungsanlage Karlsruhe
Institut fur Reaktorbauelemente
Postfach 3640
D-7500 Karlsruhe 1,
Federal Republic of Germany

K. Ehrlich

Kyushu University
Research Institute for Applied Mechanics
6-10-1 Hakozaki, Higashi-ku
Fukuoka 812, Japan

K. Kitajima

National Research Council
Montreal Road
Ottawa, Canada

EV Kornelson

National Research Institute for Metals
Nuclear Materials Division
1-2-1 Sengen, Sakura-mura,
Niihari-gun, Ibaraki 305
Japan

N. Kishimoto

Osaka University
Dept of Nuclear Engineering
2-1, Yamada-oka, Suita,
Osaka 565, Japan

K. Sumita

Science University of Tokyo
Engineering Dept
Kagurazaka, Shinjuku-ku,
Tokyo 162, Japan

RR Hasiguti

Studiecentrum voor Kernenergie
Centre d'Etude de l'Energie Nucleaire
Boeretang 200
B-2400 Mol, Belgium

J. Nihoul

Tokyo Institute of Technology
12-1, 2-Chome, O-Okayama
Meguro-ku, Tokyo, Japan

K. Kawamura

United Kingdom Atomic Energy Authority
Atomic Energy Research Establishment
Metallurgy Division
Building 388
Oxfordshire, OX11 ORA, UK

DR Harries

University of Tokyo (3)
Bunkyo-ku,
Tokyo 113, Japan

Naohira Igata, Met & Mater Science
Shiri Ishino, Nuclear Eng
Taijiro Uchida

DISTRIBUTION (Cont'd)

HEDL (38)

HR	Brager	W/A-64	NF	Panayotou	W/A-65
WL	Bunch	W/B-47	EF	Parker	W/E-17
LL	Carter	W/B-47	RW	Powell	W/A-64
DG	Doran (5)	W/A-57	RJ	Puigh	W/A-58
EA	Evans	W/C-23	FH	Ruddy	W/C-39
FA	Garner	W/A-57	FA	Schmittroth	W/A-4
DS	Gelles	W/A-64	WF	Sheely	W/C-62
R.	Gold	W/C-39	RL	Simons	W/A-57
HL	Heinisch	W/A-57	AL	Trego	W/E-15
DL	Johnson	W/A-4	GL	Wire	W/A-58
GD	Johnson	W/A-65	HH	Yoshikawa	W/C-44
NE	Kenny	W/C-115	Central Files	(5)	W/C-110
FM	Mann	W/A-4	Publ Services	(2)	W/C-115
WN	McElroy	W/C-39	Doc Clearance		W/C-123
EK	Opperman	W/A-58			